Dissertation
submitted to the
Combined Faculties for the Natural Sciences and for Mathematics
of the Ruperto Carola University of Heidelberg, Germany
for the degree of
Doctor of Natural Sciences

presented by
Diplom-Physicist: Andreas Bayer
born in: Heidenheim a. d. Brenz

Oral examination: June 29, 2005

X-ray attenuation techniques to explore the dynamics of water in porous media

Referees: Prof. Dr. Kurt Roth
Prof. Dr. Bernd Jähne

Röntgenabschwächung zur Untersuchung der Dynamik von Wasser in porösen Medien

Der Fluss von Wasser in einem ungesättigten porösen Medium wird von der Richards' Gleichung beschrieben. Diese gilt für den Fall, dass die Luft in den Poren beliebig mobil ist und jederzeit aus dem Porenraum entweichen kann. Ausserdem benötigt man zur Lösung der Richards' Gleichung eine Parametrisierung für die Beziehung zwischen Wassergehalt und Matrixpotential, die Boden-Wasser Charakteristik. Verschiedene Modelle beschreiben diese Kurve, deren Parameter in der Regel durch inverse Modellierung dynamischer Ausflussexperimente bestimmt werden können.
Es wurde ein experimenteller Aufbau entwickelt, der es ermöglicht, Ausflussexperimente an porösen Medien durchzuführen, an denen gleichzeitig Röntgenabschwächungsprofile und tomographische Bilder gemessen werden können. Mit diesem Aufbau wurden Experimente durchgeführt, mit denen die Gültigkeit der Richards' Gleichung bei verschiedenen Randbedingungen überprüft werden konnte. Dazu wurden in der Probe gemessene vertikale Wasserverteilungen mit Vorhersagen von Simulationen verglichen. Anhand der gefundenen Abweichungen konnte gezeigt werden, dass die Kontinuität der Luftphase nicht immer gegeben ist, und Heterogenitäten die Objektivität der gefunden effektiven Parameter verhindern können.
Ausserdem werden Methoden gezeigt, wie mit Hilfe von Röntgentomographie die grobe innere Struktur von Proben analysiert werden kann.

X-ray attenuation techniques to explore the dynamics of water in porous media

The flow of water in an unsaturated porous medium is described by Richards' equation. It is based on the assumption that the air in the pores is arbitrarily mobile and able to disappear from the pore space at any time. To solve Richards' equation a parameterization of the relationship between the water content and the matric potential is necessary: the soil-water characteristic. There are several models that describe this curve. Their parameters are typically determined from dynamic outflow experiments.
A experimental setup was designed, that allows measurements of X-ray attenuation data and tomographic images during the outflow experiment. With this setup experiments were done to test the validity of Richards' equation for different boundary conditions. Therefore, the measured vertical distribution of water was compared with simulated distributions. The differences found show

that the continuity of the air phase is not given at all points, and heterogeneity may prevent the determined effective parameters from being objective. Additionally, methods are introduced to analyze the rough internal structure of samples using X-ray computed tomography.

Contents

List of Figures

Symbols

This list contains the most important symbols and notations used.

The mathematical structure of symbols is indicated by their typographical appearance:

a	scalar
$\mathbf{a}$	vector
A	tensor
sin	standard function

Subscripts usually refer to a component of a vector (x, y, z, or 1, 2, 3) or to the phase (air, $water$, $matrix$).

Parentheses (...) are used for arguments of functions and operators.

The arguments of functions are suppressed if they are clear from the context, e.g., $\frac{\partial}{\partial x} f$ instead of $\frac{\partial}{\partial x} f(x)$. They are written, however, if the dependence on an argument is emphasized, e.g., $A(\theta(z))$ for a vertical attenuation profile that depends on the water content. The total derivative $\frac{d}{dt}$ means in detail $\frac{\partial}{\partial t} + \mathbf{v} \cdot \nabla$ with respect to time.

The pressure is sometimes given in units of [cm] or [cmWC] which means the pressure of a hanging water column with the same height.

Lowercase Latin Symbols

$\mathbf{g}$	acceleration of gravity [$\mathrm{L\,T^{-2}}$]
$\mathbf{j}_w$	volume flux of water [$\mathrm{L\,T^{-1}}$]
h	matric head [L]
l_{ij}	projection matrix in the iterative reconstruction algorithm

Uppercase Latin Symbols

I_{00}	measured intensity on the detector without any absorbers [counts]

I_0 measured intensity on the detector with present bow tie filter [counts]

K hydraulic conductivity tensor [$M^{-1}L^3T$]

K_s hydraulic conductivity at water saturation [L^3T^{-1}]

Lowercase Greek Symbols

ψ_w density of potential energy of water [E L^{-3}]

ψ_m matrix potential [E L^{-3}]

Θ water saturation [-]

ϕ porosity of porous media [–]

θ volumetric water content [–]

θ_s volumetric water content at saturation [–]

θ_r residual volumetric water content [–]

μ X-ray attenuation coefficient, the subscripts will indicate the material [L^{-1}]

Mathematical Notation

$\frac{d}{dt}$ total derivative with respect to time [T^{-1}]

$\frac{\partial}{\partial t}$ partial derivative with respect to time [T^{-1}]

∇ partial derivative with respect to space [L^{-1}]

1 Introduction

Flow and transport through porous media can be separated into two regimes, *saturated* and *unsaturated*. In the saturated zone the flow of water is well described by Darcy's law (Darcy, 1856). The most common example for saturated flow is groundwater flow in an aquifer. The porous medium there can be heterogeneous to different extents, but the flow of water in all these structures is well described by Darcy's law, if there is an adequate knowledge about the structure and the saturated hydraulic conductivity.
The unsaturated zone is the region between the soil surface and an underlying water table. This zone has to be passed by water on its way from the soil surface to the groundwater. A lot of biological processes happen in this region, e.g. decomposition of dissolved matter. In contrast to the saturated zone, the pore space is only partially filled with water. The water is caught in pores because of capillary forces and discontinuities of the fluid phase.
The degree of saturation is changing with time and space due to rainfall, evaporation and root water uptake. The hydraulic conductivity, constant in the saturated zone, depends on the water saturation in the way that it decreases with decreasing saturation. The description of water flow through the unsaturated zone is a challenging undertaking. Detailed knowledge about the hydraulic behavior is also needed when considering transport of dissolved matter, e.g. travel times of dissolved contaminants are important for predictions about the risk arising from them on their way through soil.

Motivation

In the unsaturated zone the dynamics of water is described by Richards' equation (Richards, 1931). To solve this equation a parameterization of the relationship between water saturation and matric potential is necessary, the water retention curve. There are a lot of approaches that describe this curve (Brooks and Corey, 1966; van Genuchten, 1980; Russo, 1988; Kosugi, 1996; Arya and Paris, 1981; Kastanek and Nielsen, 2001). Common to all of them is that there are free parameters which are determined by fitting the model to measured

points of the water retention curve or by inverse modeling of outflow experiments.
The water retention curve depends on the pore space of the medium, the pore size distribution (Kosugi, 1996; Arya and Paris, 1981) and the topology Vogel (2000).
This dependency also causes hysteresis, different saturations can be found for a fixed potential depending on the history of the system (Haines, 1930; Kool and Parker, 1987; Jaynes, 1992; Parlange, 1976; Mualem, 1984; Topp, 1971; Gillham *et al.*, 1976). The saturation is higher if it is measured during drainage than during imbibition.

To predict the dynamics of water at the field scale (length scale of 10 m) the subsoil is divided into observable substructures each assumed to be homogeneous. Then, for each substructure hydraulic parameters are determined. Typically, undisturbed soil samples are prepared (length scale of 0.1 m) and adequate experiments are performed in the laboratory. By solving Richards' equation with the estimated parameters the hydraulic behavior at the field scale is simulated.
The assumed homogeneity of the single substructures is often disturbed by smaller structures. This could have a large impact on large scale observations. Flury *et al.* (1994) observed dye patterns at different test sites and addressed the observed shape to small structures like macro-pores and cracks.

During outflow experiments the sample is accessible at its boundaries. The pressure at the boundaries is changed and the resulting amount of outflow is analyzed. These methods provide quantities that average out the internal behavior of the sample. Direct information about the internal behavior can be obtained by cutting the sample into slices and analyze them with respect to the samples structure or patterns of previously applied dye. This is a huge experimental effort and predictions based on the detailed information cannot be tested, since the sample is destroyed.
Non-destructive methods, like X-ray attenuation and tomography, became attractive Mees *et al.* (2003). Structure models, obtained form bulk density measurements by X-ray tomography, were used to predict the outflow measured in a multi-step outflow experiment (Vogel *et al.*, 2002) and the breakthrough curves of tracers (Kasteel *et al.*, 2000). Císlerová and Votrubová (2002) visualized the pore space of soil samples using computed tomography to study flow dynamics.
X-ray tomography can be used to analyze samples at different scales. With

lower spatial resolution it is possible to detect the bulk density of large samples (some 10 cm) and the pore space can be explored by micro-tomography on smaller samples (some 1 cm) (Wildenschild *et al.*, 2002; Culligan *et al.*, 2004). Hopmans *et al.* (1992, 1994) studied the dynamics of water during a one-step outflow experiment using vertical water content profiles and tomographic images.

Most of the experiments were done in clinical scanners. Clinical reconstruction methods correct beam hardening assuming water to be the main material of the sample. Soil samples have different attenuation properties than the expected water leading to artefacts that must be corrected. In clinical scanners time consuming experiments are not possible since the scanners are used to aquire human data. While the support to control the boundary conditions of the samples is not available the sample must be in hydrostatic equilibrium.

The setup presented in this work offers the support to perform multi-step outflow experiments and record X-ray data without moving the sample to an external scanner system. This allows detailed studies of the internal flow dynamics, even under transient conditions.

Outline

The present work is structured in four parts. In chapter 2 the theoretical background of water flow in porous media will be illuminated (sec. 2.1). The sections 2.2 and 2.3 deal with X-ray production and attenuation in media followed by the description of image reconstruction from projection data (sec. 2.4). This includes the method of filtered back-projection and the implementation of an iterative reconstruction algorithm.
The experimental setup is presented in chapter 3. Afterwards in chapter 4 experimental studies are discussed. A method to determine hydraulic parameters from X-ray attenuation data is demonstrated (sec. 4.1). In sec. 4.2 the imbibition of water into a dry sample is monitored as vertical X-ray attenuation profiles. Comparison to simulations of the capillary rise show differences that can be explained with a loss of the continuity of the air phase during the experiment. An advanced experiment is presented in sec. 4.3 where a traditional multi-step outflow experiment is supported by X-ray measurements. Here, a weak layered heterogeneity of the sample was obtained produced unintentionally during sample preparation. A layered material model based on

X-ray attenuation profiles was able to describe the measured outflow curve as well as the internal water distribution of the sample.
Further experiments follow in sec. 4.4 that demonstrate several applications of X-ray attenuation and tomography to calibrate light-tranmission methods, exploring the internal structure of natural soil and supporting experiments with structured artificial samples.
Finally in section 5 the work be summarized.

2 Theoretical background

The possibility to describe the water flow through a porous medium is important in many situations. Groundwater simulations and risk assessment for dumping areas for example need precise descriptions of the hydraulic behavior in the subsurface. As in other disciplines of physics one is looking for effective parameters that can be measured on samples in laboratory. Typical length scale of these samples is 0.1 m and the results are used at larger scales to make predictions for the hydraulic evolution at the site of interest. This needs experimental and theoretical methods to achieve parameters and handle them in a useful way. In the following chapter an introduction to the theoretical background of water flow through porous media will be given. Theoretical details can be found is several textbooks, e.g. Bear (1988); Kutílek and Nielsen (1994); Freeze and Cherry (1979); Roth (2005).
X-ray tomography and attenuation techniques are used to explore the distribution of water within samples qualitatively and quantitatively. Therefore the used formalisms for image reconstruction and handling X-ray transmission and attenuation data will be demonstrated.

2.1 Water flow through porous media

A porous medium is characterized by a matrix occupied by a pore space. This configuration can be found in a lot of materials, like soil, rocks, in a sponge and foams made of metal or plastic. The flow dynamics in such a medium can be described on the pore-scale by the Navier-Stokes equation.
For a Newtonian fluid the force acting on an arbitrary volume element ΔV with density ρ and mass Δm is the sum of forces (fig. 2.1) originating from

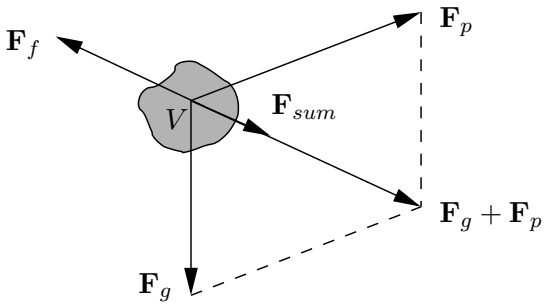

Figure 2.1: Forces that act on an arbitrary volume of water V. The force $\mathbf{F}_g$ originates from gravity, $\mathbf{F}_p$ from a pressure difference and $\mathbf{F}_g$ from inner friction. The direction of motion is indicated by $\mathbf{v}$.

gravity $\mathbf{F}_g$, a pressure difference $\mathbf{F}_p$ and the inner friction $\mathbf{F}_f$

$$\begin{aligned} \mathbf{F}_{sum} &= \mathbf{F}_g + \mathbf{F}_p + \mathbf{F}_f \\ \Delta m \frac{d\mathbf{v}}{dt} &= \Delta m g + \nabla p \Delta V + \eta \nabla^2 \mathbf{v} \Delta V \\ \rho \Delta V \frac{d\mathbf{v}}{dt} &= \rho \Delta V g + \nabla p \Delta V + \eta \nabla^2 \mathbf{v} \Delta V \\ \rho \frac{d\mathbf{v}}{dt} &= \rho g + \nabla p + \eta \nabla^2 \mathbf{v} \end{aligned} \tag{2.1}$$

where g is the acceleration of gravity and η the viscosity of the fluid. Substituting the total derivative $\frac{d\mathbf{v}}{dt} = \frac{\partial \mathbf{v}}{\partial t} + \mathbf{v} \cdot \nabla \mathbf{v}$ leads to the Navier-Stokes equation

$$\left(\frac{\partial}{\partial t} + (\mathbf{v} \cdot \nabla) \right) \mathbf{v} = \mathbf{g} - \frac{1}{\rho} \nabla p + \frac{\eta}{\rho} \nabla^2 \mathbf{v} \tag{2.2}$$

that describes the classical hydrodynamics. It is a non-linear partial differential equation whose solution is the velocity distribution $\mathbf{v}(s,t)$ as a function of space and time. Because of the non-linear term $(\mathbf{v} \cdot \nabla)\mathbf{v}$ this equation is difficult to solve in general. With special assumptions and boundary conditions there exist solutions. For a porous medium the geometry of the pore space has to be used as boundary condition and therefore it must be known for the whole sample.

2.1.1 Richards' equation

An empirical approach for the description of fluid flow in saturated porous media was introduced by Darcy (1856) where the volumetric flux $\mathbf{j}_w$ is proportional to the pressure gradient ∇p as the driving force

$$\mathbf{j}_w = -\mathsf{K}_s \nabla p \quad . \tag{2.3}$$

The constant of proportionality K_s is the saturated hydraulic conductivity. In contrast to the Navier-Stokes equation (2.2) the exact geometry of the pore space must not be known. Darcy's law is defined for the continuum scale and K_s is an effective parameter that describes the hydraulic behavior in the pore space.

For unsaturated soil Buckingham (1907) extended Darcy's law (2.3) by substituting the constant K_s with $\mathsf{K}(\theta)$ a hydraulic conductivity that depends on the water content θ

$$\mathbf{j}_w = -\mathsf{K}(\theta) \nabla p \quad . \tag{2.4}$$

To describe temporal changes of water flow the conservation of mass of water is taken into account

$$\frac{\partial}{\partial t}\theta + \nabla \mathbf{j}_w + r_w = 0 \tag{2.5}$$

meaning, that the temporal change of water within an arbitrary volume is caused by a flux of water into or out of the volume. The term r_w considers sinks and sources in the volume like root uptake or wells. Without any sinks and sources r_w will disappear and (2.4) and (2.5) lead to the differential equation

$$\frac{\partial}{\partial t}\theta - \nabla \left(\mathsf{K}(\theta) \nabla \psi_w \right) = 0 \quad , \tag{2.6}$$

in mixed form that describes the flow of water through a rigid porous medium. To obtain only one state variable the water potential can be written as $\psi_w = \psi_m - \rho_w g z$. Thus, $\mathsf{K}(\theta)$ must be described by $\mathsf{K}(\psi_m)$ that requires a formulation of $\theta(\psi_m)$ resulting in

$$C_w(\psi_m) \frac{\partial}{\partial t}\psi_m - \nabla \left(\mathsf{K}(\psi_m) \left(\nabla \psi_m - \rho_w g \right) \right) = 0 \quad , \tag{2.7}$$

where $C_w(\psi_m) := \frac{d\theta}{d\psi_m}$. This equation is called Richards' equation (Richards, 1931) in the potential form. In terms of matric head $h = \psi_m / \rho_w g$ it becomes

$$C_w^*(h) \frac{\partial}{\partial t} h - \nabla \left(\mathsf{K}(h) \left(\nabla h + 1 \right) \right) = 0 \quad , \tag{2.8}$$

with $C_w^*(h) := \frac{d\theta}{dh}$.

Richards' equation can be solved numerically to describe the flow through a porous medium. One major assumption that is made in this formalism, is that the whole problem is a single phase problem. To remove water from the pore space of a porous medium it has to be replaced by another phase, normally air. Thus, the volume the water is taken from must have a connection to the reservoir of air. If this is not true, the water cannot be removed. The same statement holds for infiltration. Filling a volume of the pore space with water, again, a direct connection to the reservoir of air is necessary. The occupying air has to disappear before water can take its place. Richards' equation assumes the air phase as arbitrarily mobile, continuous and connected to its reservoir. Then, the pressure in the air phase is constant at all points, equal to the pressure of the reservoir (Roth, 2005). This assumption has to be kept in mind when simulating hydraulic behavior of porous media by solving Richards' equation.

With increasing water content these assumptions are not satisfied any more. When the number of water filled pores increases, the connection of air to its reservoir will become worse. The air is not longer arbitrarily mobile and the pressure in the air phase is not constant and has to be taken into account.
A further increase of water content leads to a discontinuity of the air phase. Air entrapments emerge in volumes that are by-passed by water. This air is not mobile any more in the sense that it can follow pressure gradients. The only possibilities to remove it are bubbles produced when the pressure in the air phase reaches a point where bubbles can be formed and leave the trap. A second process is to dissolve the air in water and transport it to other places. This behavior cannot be described by Richards' equation which is a single phase description.

Solving Richards' equation (2.7) or (2.8) needs a description for $\theta(h)$ and $\mathsf{K}(h)$. Two prominent parameterizations are given by Brooks and Corey (1966) and van Genuchten (1980).

Brooks and Corey (1966) introduced a parameterization assuming a power-law distribution of the pore radii with a finite upper limit leading to

$$\Theta(h) = \begin{cases} (h/h_0)^{-\lambda} & \forall \;\; h > h_0 \\ 1 & \forall \;\; h \leq h_0 \end{cases} \tag{2.9}$$

where λ is a positive free parameter, h_0 the air-entry pressure where the largest pores drain first, and Θ the water saturation defined as

$$\Theta := \frac{\theta - \theta_r}{\theta_s - \theta_r} \quad , \tag{2.10}$$

where θ_s and θ_r are the saturated and residual water content, respectively. The upper case of (2.9) can be inverted as

$$h(\Theta) = h_0 \Theta^{-1/\lambda} \quad , \tag{2.11}$$

which was originally published by Brooks and Corey (1966).

Another famous and often used parameterization is the one defined by van Genuchten (1980)

$$\Theta(h) = (1 + (\alpha h)^n)^m \quad , \tag{2.12}$$

where Θ is again the water saturation as defined in (2.10). The shape and position of the curve is determined by the empirical parameters α, n and m. Often (2.12) is used in a simpler form where $m = -1 + 1/n$

$$\Theta(h) = (1 + (\alpha h)^n)^{-1+1/n} \tag{2.13}$$

to reduce the number of free parameters. The inversion of (2.13) leads to

$$h(\Theta) = \alpha^{-1} \left((\Theta^{-n/(n-1)} - 1) \right)^{1/n} \quad . \tag{2.14}$$

Comparison with (2.11) for $\alpha h \gg 1$ and

$$n - 1 = \lambda \quad \text{shows that} \quad \alpha^{-1} = h_0 \tag{2.15}$$

and can also be interpreted as the air entry value.

In principle, the free parameters of the two parameterizations have no physical meaning. They just define a class of functions that can describe the experimentally found shape of water-retention curves for typical materials. In fig. 2.2 some water retention curves for the two parameterizations are shown. It is obvious, that with the conditions (2.15) both parameterizations approximate each other for low saturation. The difference at high saturation is quite evident. While the Brooks-Corey parameterization shows a sharp air entry value (fig. 2.2), that also causes a discontinuity in the derivative at this point,

the van Genuchten description has a continuous transition at this point which often is easier to handle in numerical calculations.

The sharp air entry value of the Brooks-Corey description means that there is a maximum pore radius and an abrupt ending of the pore size distribution. If the abrupt ending is soften one will end up with a shape of the $\Theta(h)$ curve similar to that of van Genuchten. From a physical point of view the sharp ending is more realistic, because of the limited maximal pore radius corresponding to this point. While the behavior described by van Genuchten (1980) is often found in experiments it must be addressed to boundary effects e.g. pounding water at the surface. There are a lot of other parameterizations based on different assumptions for the pore space (Russo, 1988; Kosugi, 1996; Arya and Paris, 1981). These models start from a geometric model of the pore space, typically the pore size distribution. This quantity can hardly be measured directly. Hence, the related model parameters must be used as fitting parameters. Vogel (2000) demonstrated that the shape of the $\Theta(h)$ not only depends on the pore size distribution but also on the topology of the pore space.
However, there is neither a "correct" nor a "wrong" parameterization. The only physical constraints for $\Theta(h)$ are: it must be continuous and monotone. There are no jumps allowed and the water content can only decrease during drainage and increase at imbibition. Based on these limitations a very flexible approach was proposed by Kastanek and Nielsen (2001) who used cubic spline interpolations to describe the water retention curve.

The validity of the empirical parameterizations, presented above, is tested by comparison to experimental results. They all contain free fit parameters that have to be determined from measured data. Until now, it is not clear if $\Theta(h)$ is a real material property in the sense that it can be determined from physical quantities, e.g. the mass of an object that can be calculated from its mass density and its volume. The water retention curve also depends on the history of the matric head. For a fixed value h one will find different water contents for drainage and imbibition. This effect is called "*hysteresis*". On the pore scale this can be explained by the so called "*ink-bottle*" effect depict in fig. 2.3. The ceiling of water in a capillary connected to a water table at the bottom is determined by its radius (case a) and d) in fig. 2.3). For a capillary with different radii the ceiling also depends on the history of the system. For drainage the height in the capillary (case b) is limited by the smaller radius and for imbibition by the larger one (case (c)).
Hysteresis due to structure is caused by breaking the continuity of one phase

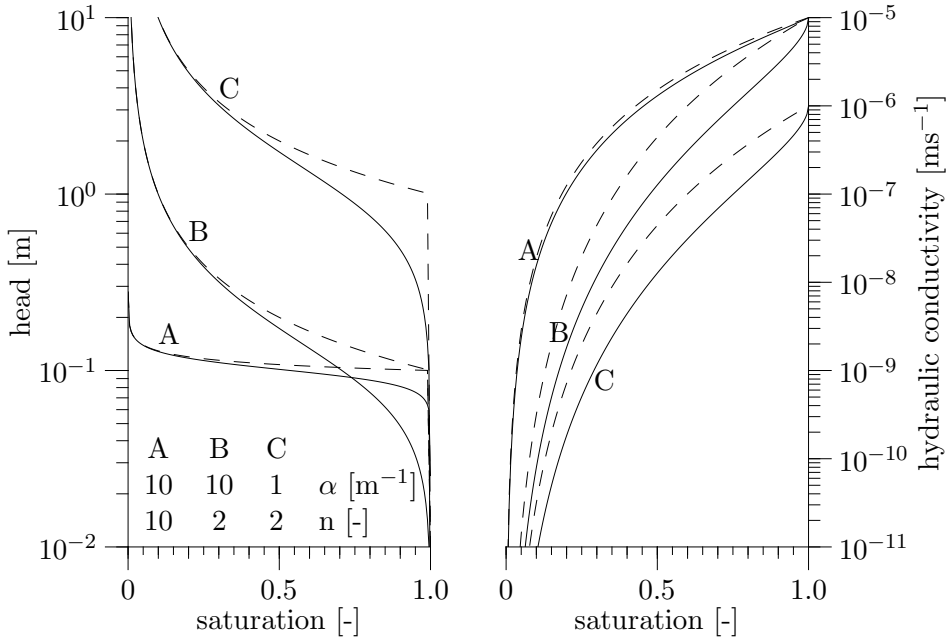

Figure 2.2: Left graph shows example parameterizations $h(\Theta)$ of Brooks and Corey (1966) (dashed) and van Genuchten (1980) (solid). The used parameters are shown in the image or calculated with respect to (2.15). On the right the unsaturated hydraulic conductivity $\mathsf{K}(\Theta)$ is shown calculated with (2.19) and the two different models of $h(\Theta)$. The saturated hydraulic conductivity is chosen to be $1 \cdot 10^{-5}$ m/s (A,B) and $1 \cdot 10^{-6}$ m/s (C). The used values of α and n are shown in the left graph.

by the other. This can be done during imbibition, as shown in section 4.2, by filling the small pores rapidly and by-pass the larger. During drainage the same effects can be observed by draining larger pores faster and break the continuity of the small ones.
Dynamic effects also influence the water retention curve. The driving force for water movement is, beside gravity, the capillary pressure P^c typically assumed to be equal to the difference between the pressure in the wetting phase P^w and in the non-wetting phase P^n. Hassanizadeh *et al.* (2002) showed that this equality is only fulfilled in equilibrium or steady state. From a thermo-

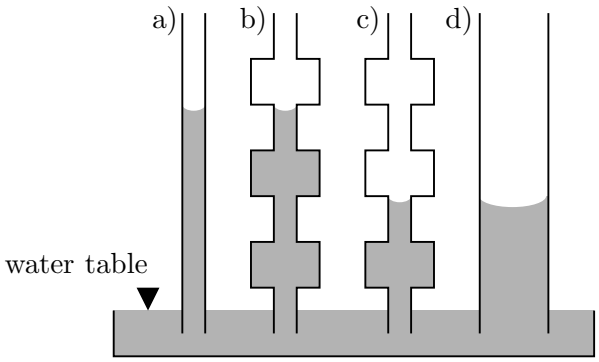

Figure 2.3: Ink-bottle effect demonstrated with two single radius capillaries a) and d) and two mixed radius capillaries b) (for drainage) and c) (for imbibition) connected to a water table at the bottom (adapted from Graf (2004)).

dynamical basis (Hassanizadeh and Gray, 1993) demonstrated that

$$-\epsilon \frac{D^s S}{Dt}[(P^n - P^w) - (P^c)] \geq 0 \quad , \tag{2.16}$$

where ϵ is the porosity and $\frac{D^s S}{Dt}$ the material time derivative of the wetting phase saturation S observed when moving with the solid phase. For a rigid medium this derivative reduces to $\frac{\partial S}{\partial t}$. For equilibrium or steady-state the time derivative disappears and the capillary pressure becomes $P^c = P^n - P^w$. They approximated (2.16) by introducing a positive material coefficient τ with

$$-\epsilon \frac{D^s S}{Dt} = -(\tau^{-1})[(P^n - P^w) - (P^c)] \quad . \tag{2.17}$$

The parameter τ is interpreted as a measure of the speed with which a change of saturation takes place. If the equilibrium of the system is disturbed by changing the external pressures P^w and/or P^n the system needs time to react on this change by adapting the saturation. Not until this change is finished the capillary pressure becomes constant and equal to $P^n - P^w$. The pressure that is responsible for the water content is P^c but externally accessible are P^n and P^w. The parameterizations for $\Theta(h)$ account for the measurable difference $P^n - P^w$. Therefore, the water content in the sample that depends on P^c is different form the predicted if dynamic effects play a major role. Until now it is not clear which conditions lead to dominating dynamic effects. Systems with

a low hydraulic permeability or heterogeneity are expected to have amplified dynamic capillary pressure effects (Hassanizadeh *et al.*, 2002).

The other important material property is the unsaturated hydraulic conductivity $\mathsf{K}(\Theta)$. Also different descriptions exist to calculate it based on different assumptions of the size distribution of the pores and their connectivity. Burdine (1953) introduces a model based on the assumption that the pore space is built from parallel bundles of capillaries each with constant radius, leading to

$$\mathsf{K}(\Theta) = \mathsf{K}_s \Theta^a \frac{\int_0^\Theta h(\vartheta)^{-2} d\vartheta}{\int_0^1 h(\vartheta)^{-2} d\vartheta} \quad , \tag{2.18}$$

where $\mathsf{K}(\Theta)$ is calculated from the parameterization of $h(\Theta)$ and the term Θ^a includes the effect of tortuosity.

Another description was given by Mualem (1976) where the bundles are assumed to be randomly connected as

$$\mathsf{K}(\Theta) = \mathsf{K}_s \Theta^a \left(\frac{\int_0^\Theta h(\vartheta)^{-1} d\vartheta}{\int_0^1 h(\vartheta)^{-1} d\vartheta} \right)^2 \quad . \tag{2.19}$$

Both models start with the description of $h(\Theta)$. The model of Mualem is used in most computer implementations. With the two parameterizations $h(\Theta)$ given in (2.11) and (2.14) there are two models for $\mathsf{K}(\Theta)$ by inserting in (2.19). The Mualem/Brooks-Corey description by combining (2.19) and (2.11)

$$\mathsf{K}(\Theta) = \mathsf{K}_s \Theta^{a+2+2/\lambda} \tag{2.20}$$

and the Mualem/van Genuchten model

$$\mathsf{K}(\Theta) = \mathsf{K}_s \Theta^a \left(1 - \left(1 - \Theta^{n/(n-1)} \right)^{1-1/n} \right)^2 \tag{2.21}$$

by inserting (2.14) in (2.19). Example curves of these two parameterizations are shown in the right graph of fig. 2.2.

2.1.2 Methods to determine the pressure-saturation relation

As shown before the pressure-saturation relation $h(\Theta)$ is an important material property. There exist a lot of methods to measure or calculate it. A direct

method to obtain $\Theta(h)$ is to apply a fixed pressure to a soil sample. After equilibration the saturation of the sample is measured by weighing the sample. If this is done for different values of h, $\Theta(h)$ can be estimated by fitting one of the parameterizations and determine the relevant parameters.
Another method is to establish a well defined saturation to a soil sample and measure the capillary pressure after equilibrium is reached. With this method $h(\Theta)$ will be monitored e.g (Brooks, 1980). All these methods need more or less time to equilibrate the water phase to the external pressure which can be very time consuming.
Also theoretical approaches were made by predicting $h(\Theta)$ from the particle size distribution as shown by Arya and Paris (1981) or Chan and Govindaraju (2004).

An alternative to the static experimental methods are dynamic experiments like one- (Kool *et al.*, 1985; Parker *et al.*, 1985; van Dam *et al.*, 1992) or multi-step outflow experiments and calculate $h(\Theta)$ by inverse modeling (van Dam *et al.*, 1994).
In a multi-step outflow experiment different pressures are applied to the porous medium and the cumulative water outflow is measured as a function of time. Then, the experiment is modeled using the hydraulic properties as free fitting parameters. This method was used during this work and will be introduced in more detail in section 3.2 on page 48.

2.1.3 Monitoring pore structure and water content

The hydraulic behavior within a sample of porous media away from water saturation can be described satisfyingly as long as the air phase is continuous, arbitrarily mobile and connected to the atmosphere by Richards' equation. But the transition from this regime to another where the connection to the atmosphere is cut off or volumes of air are entrapped is not well defined. Also these regimes can coexist within one single sample, for example a dry sample that is connected to a water table at the bottom. Then, after some time the lower part will be fully saturated and the sample less saturated towards the top. All kinds of saturation are present in one sample. This will lead to a poor description of the hydraulic behavior if one of the "non Richards" regimes dominates and is not taken into account during analysis. In typical experiments it is not possible to obtain information about the inside of a sample without destroying it. During the last years in soil physics methods became attractive that can scan samples without destruction.

Visual imaging: Normally porous media are not transparent for optical methods and so they are useless. Except the porous medium is designed artificially with regard to use optical methods, e.g. crushed glass and adequate fluids, used by Stöhr (2003) to study flow and transport using visible light methods. Also when thin slices of material are used optical methods will work e.g. fingered flow in a Hele-Shaw cell filled with sand (Darnault *et al.*, 2001; Tidwell and Glass, 1994; Pons *et al.*, 1999).

Neutron scattering: When the samples become larger and intransparent optical methods fail and others are attractive. Neutron scattering methods are very sensitive to water. The cross-section for scattering neutrons in water is very large due to the cross-section of hydrogen (82.02 barn) compared to the one of silicon (2.167 barn) or oxygen (4.232 barn) (Neutron, 92). Solymar *et al.* (2003) used this method to produce tomographic images and detected changes of water saturation in a sandstone sample. The major disadvantage is that neutron sources with adequate fluxes need a nuclear reactor and are not available for experiments in a normal laboratory. In fig. 2.4 two examples for tomography with neutrons are presented. Obviously the distribution of water is easy to observe, but the density of the material is only reflected by its different water content. In a dry sample heterogeneities are hard to detect with this method because of the low scattering cross-section of sand.

Nuclear Magnetic Resonance: Another non-destructive method, sensitive to water, is nuclear magnetic resonance (NMR) where the magnetic properties of the ^{1}H-proton are used to visualize water. The magnetic moment of the proton has two possible orientations in an external magnetic field, parallel and anti-parallel. These two orientations are separated by an energy gap between the two states. If photons with an energy as large as the gap penetrate the medium the magnetic orientation of the protons can flip and the photon will be absorbed. This process is called magnetic resonance. The loss of photons can be monitored and is a measure for the amount of protons in the irradiated volume. By applying special geometries in the external magnetic field the condition for resonance is only given at special locations and a spatial resolution of water content is possible. Deurer *et al.* (2002) used this technique to monitor the proton density and velocity in thin slices of a small sample of porous medium built up from glass beads with a sample diameter of 14 mm. The spatial resolution is limited because of local magnetic fields induced by the matrix material. This inhomogeneity of the magnetic susceptibility leads to ad-

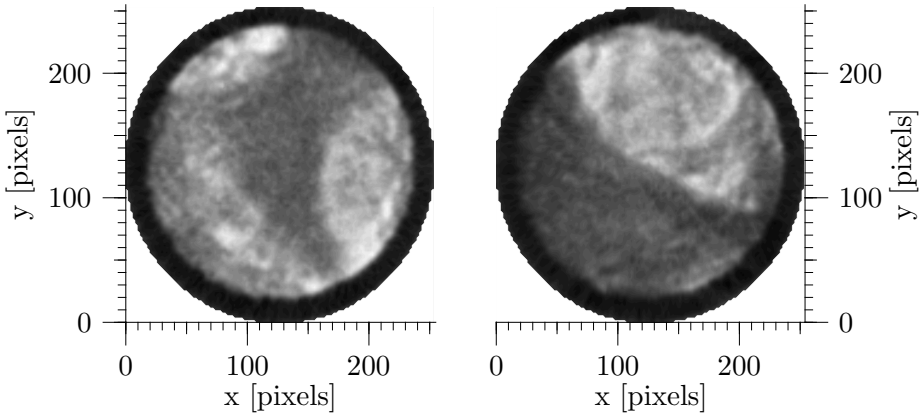

Figure 2.4: Example images for neutron tomography on porous media. Data taken at ILL (*Institute Laue-Langevin, Grenoble*) on a high-flux neutron beam-line. The sample was a vertical aluminum tube with 11 cm inner diameter filled with sand. Shown are two slices recorded in different depths with a fixed water potential at lower boundary. The water content is represented in grey levels from dark (low) to white (high water content).

ditional transverse relaxation and therefore to signal attenuation (Callaghan, 1990). Císlerová *et al.* (1997) used magnetic resonance imaging to visualize water flow in a natural soil sample of 4.5 cm in diameter. There are several other publications describing the usage of NMR in soil science published elsewhere (Hemminga and Buurman, 1997; Randall and Ivanova, 1997; Veeman, 1997; Van As and van Dusschoten, 1997; Dijk *et al.*, 1999; Deinert *et al.*, 2004). The experimental effort is also extensive large because large magnetic fields up to 4-10 Tesla produced by superconducting magnets are necessary to polarize the magnetic moments of the protons.

Measurements of larger structures in soils, like cracks, can be done by, e.g. electrical resistivity measurements as shown by Samouëlian *et al.* (2003, 2004). Here the spatial resolution is in the range of centimeters.

The method chosen in this work was X-ray attenuation and tomography, also a non-invasive method like neutron scattering or NMR, but with less technical effort and easier to handle. X-ray attenuation is in principle element specific and the pore space can be detected as well as the water occupying these pores.

The sensitivity to different materials is best, when sources are used where the wavelength of the incoming photons can be tuned and the element specific absorption edges are scanned. To guarantee enough photons with a specific wave-length huge X-ray sources with high brilliance like synchrotrons (DiCarlo *et al.*, 1997) are necessary. Another source of monochromatic photons are radioactive materials like the ^{241}Am source used by Pires *et al.* (2004a,b) that emits photons at $E_\gamma = 59.54\,\mathrm{keV}$. In contrast to synchrotrons the emitted photon energy is not tuneable and useless to scan absorption edges. Typical X-ray sources in the laboratory are polychromatic, meaning they emit the brems-spectrum of electrons slowed down in a metal target, and additionally photons with special energies characteristic for the material of the anode. This spectrum is a mixture of photons with different wavelengths, and the sensitivity to single elements is lost, since the detector is not sensitive for single wavelengths. But nevertheless attenuation of X-ray is sensitive to the local electron density. This fact is used to separate materials by their respective densities of electrons. In medical applications this is used nearly since the discovery of X-rays in 1895 by W. C. Röntgen. In the next section the principles of interaction between X-ray and matter will be described in more detail.

2.2 X-ray production

Beside radioactive decay, X-ray radiation is produced when charges are accelerated. This can be shown when Maxwell's equations are studied. To produce X-rays in the laboratory, electrons are accelerated in electrical fields up to 200 kV towards an anode. When such an electron reaches the anode it crashes into its material and slows down. Most of the kinetic energy is transformed into heat. But a small part is emitted as a mixture of photons with different wave-lengths. These photons form the so called bremsspectrum of the source. They have energies up to $E_\gamma = eU$ where e is the electron charge and U the acceleration voltage. Additionally some of the incoming electrons interact with electrons of the anode material. If an incoming electron hits an electron bound in an atom this electron can be removed, and the atom is left in an excited state. It relaxes by filling up the hole with an electron located in an energetic higher state. During this relaxation the excess energy of the electron is emitted as a photon or transfused to a second electron (Auger electrons) as kinetic energy. The photons hold the energy given by the energetic difference of the two electronic states involved. Thus, these photons are characteristic for the used material of the anode and their sum is called the characteristic spectrum

of the anode that superposes the bremsspectrum.
Advanced sources of X-ray radiation are synchrotrons or particle accelerators where charges (electrons, protons) accelerated to velocities near the speed of light are forced to change their direction of motion by applying external magnetic fields. This change is the reaction to an external force and therefore an acceleration of the charged particle, leading again to the emission of photons. This sources produce high fluxes of X-ray photons in various energy ranges depending on the kinetic energy of the particles. Using a monochromator even single energy photons can be selected with adequate quantities to perform monoenergetic attenuation experiments (Garnier *et al.*, 1998; DiCarlo *et al.*, 1997).

2.3 X-ray attenuation in solid media

The interaction mechanism between X-ray and matter can be separated in three effects: photoelectric effect, Compton scattering and pair production. The probability one of these interactions occurs depends on the energy of the incoming photon and the kind of matter itself, described by the atomic number Z.
The photoelectric effect is an interaction between a photon and an electron bound in an atom. Is the energy of the incident photon E_γ large enough to replace an electron from an inner shell with bounding energy E_B to continuum it can be absorbed. A free electron with the kinetic energy $E_{kin} = E_\gamma - E_B$ will be produced. After absorption, the atom is in an excited state due the missing electron. It relaxes by filling up the incidental hole with an electron located on a higher shell. During this process a characteristic photon is emitted or a secondary (Auger) electron produced. The photoelectric cross section is approximately

$$\sigma_{photo} \propto \frac{Z^3}{E_\gamma^3} \quad \text{for large Z}$$
$$\sigma_{photo} \propto \frac{Z^4}{E_\gamma^3} \quad \text{for small Z.}$$

The photoelectric effect dominates for photons with energies $E_\gamma < 200\,\mathrm{keV}$.

In the Compton scattering process a photon is scattered by an electron with the loss of energy depending on the angle θ between the directions of the

photon before and after scattering. The energy of the scattered photon $E_{\gamma'}$ can be calculated from the conservation of energy and momentum

$$E_{\gamma'} = \frac{E_\gamma}{1 + \frac{E_\gamma}{m_0 c^2}(1 - \cos\phi)}$$

for scattering a photon on a free electron not moving before and a rest mass of m_0. The differential cross section for bounded electrons is given by the Klein-Nishina formula (Klein and Nishina, 1929)

$$\frac{d\sigma}{d\Omega} = \frac{r_0^2}{2}\left(1 + E_\gamma(1 - \cos^2\phi)\right)^2 \left(1 + \cos^2\phi + \frac{E_\gamma^2(1 - \cos\phi)^2}{1 + E_\gamma(1 - \cos\phi)}\right) \tag{2.22}$$

where r_0 is the classical electron radius. Compared to the photoelectric effect the photon does not disappear, but its direction of flight will change and it will not be detected any more.
The third process of X-ray scattering is pair production. This effect can only occur if the energy is larger than $E_\gamma = 2m_0c^2 = 2 \cdot 511\,\text{keV}$, the energy needed to produce an electron-positron pair (m_0 rest mass of an electron). The effect is irrelevant in the energy range considered in this work.

2.3.1 Non-linear X-ray attenuation

If a X-ray beam of intensity I_0 with a certain wavelength passes a medium of thickness x the measured intensity after passage is described by the attenuation law of Beer

$$I(x) = I_0 e^{-\mu x} \tag{2.23}$$

where μ is the attenuation coefficient of the material passed. This describes the linear attenuation of X-ray, the linearity can be seen in the differential form of (2.23)

$$dI = -\mu\, I\, dx$$

where the change of the intensity per length of path dx is proportional to I, and μ is the constant of proportionality. Non-linearity of attenuation comes up when the incoming X-ray intensity is a mixture of photons with different energies and the fact of μ depending on the photon energy is taken into account. Equation (2.23) now becomes

$$I(x) = \int_0^{E_{max}} I_0(E) e^{-\mu(E)x} dE \tag{2.24}$$

where E is the photon energy, $I_0(E)$ the energy distribution if incoming photons and $\mu(E)$ the energy dependent attenuation coefficient.
The X-ray source used here is also a polychromatic source and the effect of non-linear attenuation has to be taken into account. Therefore the emitted energy spectrum of the tube was determined by measuring the attenuation for two materials of different thicknesses. The non-linearity of the shape of the received attenuation curves was used together with the known energy depended attenuation coefficient of the respective material to determine the photon energy distribution of the X-ray source. The spectrum was used for later beam-hardening corrections during image reconstruction.

There are methods to measure the spectrum directly (Matscheko and Carlsson, 1989) and also to calculate it when the geometry and material of the anode is known (Ruth and Joseph, 1997; Tucker *et al.*, 1991). To estimate the photon energy spectrum of the used X-ray source the method described by Ruth and Joseph (1997) that is based in a semiempirical model by Tucker *et al.* (1991) was used.
They modeled the bremsspectrum starting from measured attenuation data for copper and aluminum. The measured transmission $f(X) = I(X)/I(0)$ is described similar to (2.24)

$$f(X) = a_0 + \int_0^{E_{kV_p}} \epsilon(E)S(E)e^{-m(E)X}\,dE \qquad , \tag{2.25}$$

where $m(E)$ is the mass attenuation coefficient $(\frac{\mu}{\rho})(E)$ depending on the photon energy E. The sensitivity of the detector is considered in $\epsilon(E)$, the detector response function, and $S(E)$ is the emitted spectrum of the tube. The objective function now will be $S_d(E) = \epsilon(E)S(E)$ since the detector response function is not known. The constant a_0 accounts for background in the measurement and will be a free fitting parameter. To estimate $S_d(E)$ the transmission for copper and aluminum was measured for different thicknesses of the respective material. This data was fitted using (2.25) to obtain $S_d(E)$ (see fig. 2.5).

Two models for $S_d(E)$ are described by Ruth and Joseph (1997): one is based on a semiempirical bremsstrahlung model reviewed by Tucker *et al.* (1991). A second model is based on an approach without physical assumptions where $S_d(E)$ is described as a weighted sum of delta functions and the weighting coefficients are used as free fitting parameters. Here the semiempirical model was used and will be described in more detail in the following.

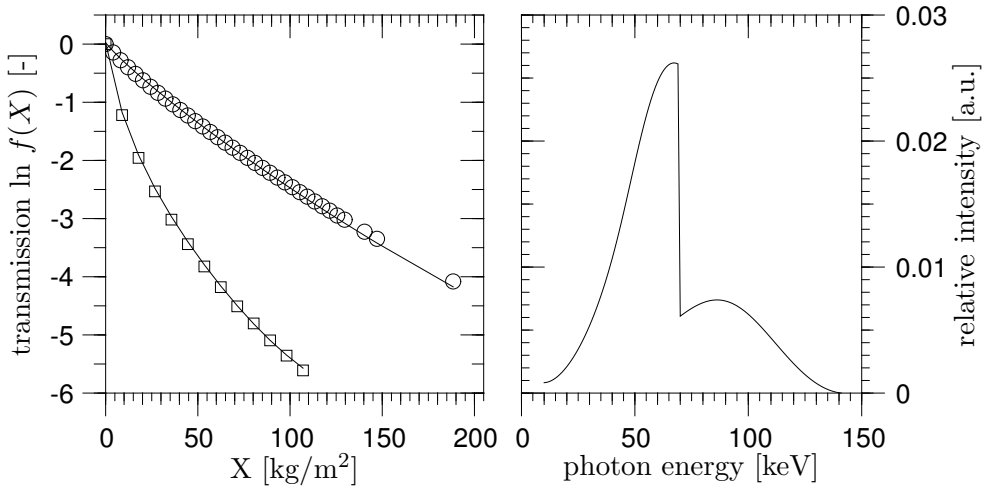

Figure 2.5: On the left side the measured attenuation for copper (squares) and aluminum (circles) is shown together with their respective fitted attenuation. The parameters found in the fit were used to generate the photon energy spectrum emitted by the used X-ray source. In the right graph values of the spectrum are normalized so that the sum of photons is equal one.

The photon energy spectrum emitted by a tungsten target is given by

$$S_d(E) \propto \int_E^{T_0} \frac{B(E, T+m)}{T} F(E,T) \left(\frac{1}{\rho}\frac{dT}{dx}\right)^{-1} dT$$

with

$$\begin{aligned} B(E,T) &= a_1 + a_2\frac{E}{T} + a_3\left(\frac{E}{T}\right)^2, \\ F(E,T) &= \exp\left(-\frac{(\frac{\mu}{\rho})_W(E)(T_0^2 - T^2)}{C\sin\theta}\right), \\ \frac{1}{\rho}\frac{dT}{dx} &= A_{msp} + B_{msp}e^{-TC_{msp}} \quad . \end{aligned} \tag{2.26}$$

T_0	:	initial kinetic energy of the initial photon
m	:	rest mass energy of the electron (511 keV)
$F(E,T)$	:	target attenuation factor
$(\frac{\mu}{\rho})_W(E)$	:	mass attenuation coefficient of tungsten
C	:	Thomson-Whiddington constant
θ	:	target angle
$\frac{1}{\rho}\frac{dT}{dx}$	:	mass stopping power for electrons
A_{msp}	=	$202.41\,\mathrm{keV\,m^2kg^{-1}}$
B_{msp}	=	$1036.1\,\mathrm{keV\,m^2kg^{-1}}$
C_{msp}	=	$0.04695\,\mathrm{keV\,m^2kg^{-1}}$

Parameters a_1, a_2 and a_3 were used as fitting parameters and A_{msp}, B_{msp} and C_{msp}, the mass stopping parameters for tungsten were taken from Tucker *et al.* (1991). The Thomson-Whiddington constant was set to $1.0 \cdot 10^4$ $\mathrm{keV^2m^2kg^{-1}}$ similar to Ruth and Joseph (1997). The fit was performed by a Levenberg-Marquardt routine (Press *et al.*, 1992) simultaneous for the two measured datasets.
The left side of fig. 2.5 shows the recorded transmission data for copper and aluminum together with the best fit curves ($\chi^2 = 0.062$). In the right graph of fig. 2.5 the resulting photon energy spectrum is shown for the parameters $a_1 = 51.6$, $a_2 = -376$ and $a_3 = 649$.

The photon energy spectrum found with this method was used for further corrections of non-linear attenuation in measured transmission data. This effect is also known as beam hardening due to the change in the energy spectrum of the photons when passing through material. The photons with lower energy disappear from the spectrum first. Therefore, with longer attenuation lengthsthe photon spectrum becomes "harder" i.e. the amount of low energy photons decreases faster than that of the high energy photons due to the non-linear attenuation coefficient.

2.4 X-ray computed tomography

As a non-invasive technique to obtain structural properties and the distribution of the water content in soil samples X-ray computed tomography has become a useful tool. It was developed for medical imaging by Hounsfield (1973), and about ten years later the first applications in soil science arose. Petrovic *et al.* (1982) tested the precision of a clinical tomography system to determine the soil

bulk density and Hainsworth and Aylmore (1983) used X-ray tomography to estimate the spatial distribution of water in soil samples. A detailed overview about the usage and applications of X-ray tomography in soil science can be found in Mees *et al.* (2003). The advantage of X-ray tomography is that the internal behavior of a sample can be studied with high spatial resolution without destroying the sample. Wildenschild *et al.* (2002) compared three scanner systems. An industrial system, a medical and a synchrotron system were used with increasing spatial resolution. With the highest spatial resolution (6.7 µm) they visualized single sand grains and separated the water and air phase occupying the pore space.
Vogel *et al.* (2002) used bulk density information obtained by tomography to produce a heterogeneous material model and predicted the result of a multi-step outflow experiment with reasonable agreement. Similar studies focused on transport are presented by Kasteel *et al.* (2000). Vertical water content profiles and tomographic images of a soil sample were recorded during a one-step outflow experiment by Hopmans *et al.* (1992, 1994). They monitored the drainage process and found that the inverse parameter estimation that solves Richard's equation becomes non-unique and instable as long as the air phase is non-continuous in the sample.

2.4.1 Data pre-processing

To compute the distribution of the attenuation coefficient including its energy dependency as shown in (2.24) a correct description of the I_0 signal is necessary. With the used setup it is in general not possible to measure this I_0 with the same tube and detector settings as for the projection measurements. The projection measurements are typically taken with a tube current of 10-50 mA and an exposure time of 24 ms. Measurements using these settings without a sample will lead to saturation of the detector signal and become useless. Typically the tube current is lowered to 1 mA and the exposure time is shorter. A correct scaling of the I_0 measurement is needed. Without using the bow tie filter (sec. 3.1.5) a simple linear scaling of I_0 to a longer exposure time and higher current is possible. When the bow tie filter is used, the energy dependence of its attenuation coefficient and the different thicknesses the beam passes, this linear scaling could not be done any more. Behind the thicker parts of the filter the beam will have a larger fraction of high energy photons than behind the thin parts.
In the following an estimate of the correct I_0-signal will be shown. The energy distribution $S_d(E)$ of the photons of the emitted X-ray beam is calculated using

the description of the bremsspectrum described in Ruth and Joseph (1997) (sec. 2.3.1). The index d notes that the sensitivity function of the detector is also included. The spectrum $S_d(E)$ is normalized in the way $\int_0^{E_{max}} S_d(E)dE = 1$. The different efficiencies of the individual detector elements and the energy distribution of the photons in each pixel is described by

$$S_{d00}(E, \alpha) = I_{00}(\alpha) S_d(E) \tag{2.27}$$

with $I_{00}(\alpha)$ as the measured intensities in each pixel of the detector in the absence of any absorber in the beam. The angle α denotes the positions of detector pixels in the fan beam. $S_{d00}(E, \alpha)$ is the number of photons with an energy between E and $E + \Delta E$ detected in direction α with respect to the current settings of exposure time and tube current. Using the bow tie filter (sec. 3.1.5) the change in the energy spectrum of the photons in this material needs to be calculated. With the known thickness of the material $x(\alpha)$ the beam passes in each direction the number of photons behind the bow tie filter can be calculated using

$$S_{d0}(E, \alpha) = S_{d00}(E, \alpha) e^{-\mu_{PVC}(E) x(\alpha)} \quad . \tag{2.28}$$

The values of the attenuation coefficient of PVC μ_{PVC}, the material of the filter, are estimated by fitting a high order polynomial to published data (National Institute of Standards and Technology, 2004). With the exact position and geometry of the filter $x(\alpha)$ can be described analytically.
For further processing $I_0(E, \alpha)$ or $I_0(\alpha)$ can be calculated with

$$I_0(E, \alpha) = u S_{d0}(E, \alpha) \tag{2.29}$$

$$I_0(\alpha) = \int_0^{E_{max}} I_0(E, \alpha) dE \tag{2.30}$$

taking into account different exposure times and tube settings while recording projection data by introducing the factor u that is proportional to the exposure time and the tube current.

Because of the unknown exact position of the tube focus point it is difficult to determine the position of the filter with high accuracy. This loss of accuracy influences the calculation of S_{d0}. For a more precise calculation of S_{d0} the thickness $x(\alpha)$ is determined from measured data. This needs the measure of $I_{00}(\alpha)$, and an intensity measurement $I_0(\alpha)$, when the bow tie filter is in the

path between source and detector. The measured intensity $I_0(\alpha)$ must satisfy (2.30), and the objective function $x(\alpha)$ is calculated by solving

$$I_0(\alpha) = u \int_0^{E_{max}} S_{d00}(E,\alpha) e^{-\mu_{PVC}(E)x(\alpha)} dk \tag{2.31}$$

obtained by combining (2.30), (2.29) and (2.28). A globally convergent Newton method implemented as shown in Press *et al.* (1992) was used to determine $x(\alpha)$, without the knowledge of the exact position of the filter.

2.4.2 Image reconstruction

There are several methods to reconstruct the spatial distribution of attenuation coefficients within a sample from recorded projection data. The most exact method is to solve a linear equation system to calculate the attenuation coefficient of each pixel of the reconstructed image. This method is rarely used because of its large effort in computing power and the bad convergence due to noise in the recorded data. The most popular method is the so called filtered back-projection (FBP). It projects each measured value back to the whole line of pixels the ray passed. A filtering process accounts for the higher density of measurements in the center of the sample than at border. This is an approximation of the direct mathematical description of computed tomography. Because of its low requirement of computing power it is attractive for online monitoring of single slices or volumes. A third method of reconstruction are iterative methods. These methods commonly start with a first guess of the reconstructed image and use it to calculate the projection data resulting from this distribution with respect to the physical processes of X-ray transmission. The calculated projection data is compared with the measured data. With the information of the deviation an update of the first guess image is calculated. This is a time consuming way but also attractive, because the implementation of physical processes also allows the introduction of corrections, for example beam hardening, to remove artefacts and increase the quality of the reconstructed image.
In the present work FBP and an implementation of an iterative algorithm are used and therefore a more detailed description will follow in the next sections.

2.4.3 The Fourier Slice Theorem

In this section the principle and also the possibility of image reconstruction will be demonstrated. The goal is to find a connection between a function $f(x,y)$

that defines the object to be reconstructed, and the measured projection data $P_\beta(t)$ where β is here the direction in which the projection was taken and t the distance of one single ray to the origin (fig. 2.6).
One projection can be written as the line integrals

$$P_\beta(t) = \int_{\xi(\beta,t)} f(x,y)ds \tag{2.32}$$

through the region where $f(x,y)$ is defined along a path $\xi(\beta,t)$. $P_\beta(t)$ is also known as the Radon transformation of $f(x,y)$. The two-dimensional Fourier transform of $f(x,y)$ can be written as

$$F(u,v) = \int_{-\infty}^{\infty}\int_{-\infty}^{\infty} f(x,y)e^{-i2\pi(ux+vy)}dxdy \tag{2.33}$$

and the Fourier transform of one projection and angle β as

$$S_\beta(w) = \int_{-\infty}^{\infty} P_\beta(t)e^{-i2\pi wt}dt\ . \tag{2.34}$$

The Fourier Slice Theorem now states that the Fourier transform of a parallel projection of the function $f(x,y)$ taken at angle β results in a slice of the two-dimensional transform $F(u,v)$ including the angle β with the u-axis (fig. 2.6). If there is an infinite number of projections the whole u,v space can be filled with information and the function $F(u,v)$ is obtained from measured projection data.
Using a finite number of projections, the data can also be used to reconstruct the original distribution $f(x,y)$. The projections have to be transformed into frequency space and because of their finite number there must be some interpolation to fill the whole space homogeneously with information and at least a two-dimensional back-transform leads to the objective function $f(x,y)$.
Problems along this way are because of the finite number of projections the density of values decreases with increasing distance to the origin in frequency space. The high frequency components of the image are calculated with a larger error than the low frequency ones, and the reconstructed image is degraded (Kak and Slaney, 1999). The filtered back-projection described in the next section takes account for this problem.

2.4.4 Filtered back-projection

The setup here uses a filtered back-projection (FBP) algorithm to calculate the "first guess" of the reconstructed image. This image is used for further processing or as input for the iterative reconstruction algorithm described in the next

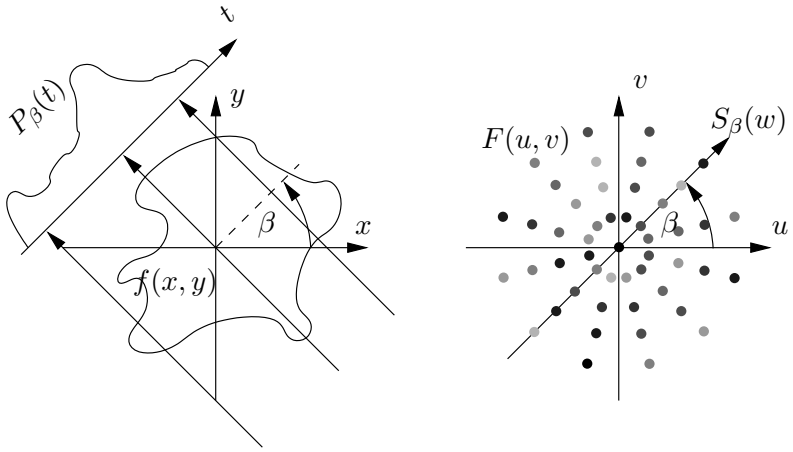

Figure 2.6: Sketch of the Fourier Slice theorem. One projection taken at rotation angle β results in on line of data in the u-v-space of the two-dimensional Fourier transform of $f(x, y)$.

section (section 2.4.5). The filtered back-projection procedure is described in several publications e.g. Kak and Slaney (1999); Toft (1996); Fuchs (1998).
To demonstrate the idea of FBP the simple case of parallel projections is assumed. Then the distribution $f(x, y)$ is given as the inverse Fourier transform of $F(u, v)$ as shown in (2.33), in detail

$$f(x,y) = \int_{-\infty}^{\infty}\int_{-\infty}^{\infty} F(u,v)e^{i2\pi(ux+vy)}dudv \tag{2.35}$$

and after representing the frequency space in polar coordinates (2.35) becomes

$$f(x,y) = \int_{0}^{2\pi}\int_{0}^{\infty} F(w,\beta)e^{i2\pi w(x\cos\beta+y\sin\beta)}wdwd\beta \tag{2.36}$$

where

$$u = w\cos\beta, \quad v = w\sin\beta \quad \text{and} \quad dudv = wdwd\beta \quad .$$

Splitting this integration into two parts whereas each represents one half rotation of β,

$$f(x,y) = \int_0^{\pi}\int_0^{\infty} F(w,\beta)e^{i2\pi w(x\cos\beta + y\sin\beta)}wdwd\beta + \int_0^{\pi}\int_0^{\infty} F(w,\beta+\pi)e^{i2\pi w(x\cos(\beta+\pi)+y\sin(\beta+\pi))}wdwd\beta \qquad (2.37)$$

and with the symmetry property $F(w,\beta+\pi) = F(-w,\beta)$ (2.36) is written as

$$f(x,y) = \int_0^{\pi}\int_{-\infty}^{\infty} F(w,\beta)|w|e^{i2\pi wt}dwd\beta \qquad (2.38)$$

where the substitution $t = x\cos\beta + y\sin\beta$ was done. The Fourier transform $F(w,\beta)$ at a certain angle can be substituted by $S_\beta(w)$ with respect to the Fourier slice theorem leading to

$$f(x,y) = \int_0^{\pi}\int_{-\infty}^{\infty} S_\beta(w)|w|e^{i2\pi wt}dwd\beta \quad . \qquad (2.39)$$

Another substitution results in

$$f(x,y) = \int_0^{\pi} Q_\beta(t)d\beta \qquad (2.40)$$

where

$$Q_\beta(t) = \int_{-\infty}^{\infty} S_\beta(w)|w|e^{i2\pi wt}dw \quad . \qquad (2.41)$$

The last equation represents a filtering operation, where the frequency response of the filter is given by $|w|$. The "filtered projections" $Q_\beta(t)$ for different angles β are then added to form the objective distribution $f(x,y)$.
At this point the filtered back-projection in (2.40) is described in three steps:

First: Calculate $S_\beta(w)$ form the measured projections utilizing (2.34).

Second: Multiply $S_\beta(w)$ in frequency space with $|w|$ and from (2.41) the filtered projection $Q_\beta(t)$ is determined

Third: The filtered projections at different angles β are back-projected to the distribution $f(x,y)$ as shown in (2.40).

There are a lot of different filter kernels that approximate the theoretical $|w|$, that try to reduce noise by suppressing high frequencies (Shepp and Logan, 1974; Jain, 1989). If data is recorded in geometries different from the parallel described above, the reconstruction can be done in the same way, but data has to be resorted into the parallel geometry first.
The geometry of the setup here forces to use the algorithm described by Kak and Slaney (1999) for an "equally spaced collinear detector" where the step of resorting to parallel geometry is skipped and included in the reconstruction process. This algorithm can also be divided into three single steps:

First: The projection data recorded in fan beam geometry $R_\beta(s)$ denotes the integrated attenuation calculated from the measured intensities on the detector at position s for the rotation angle β. From this data modified projections

$$R'_\beta(s) = R_\beta(s)\frac{D}{\sqrt{D^2+s^2}} \tag{2.42}$$

are calculated where D is the distance from the source of the fan beam to the origin which is located at the center of rotation.

Second: The modified projections $R'_\beta(s)$ are filtered as convolution resulting in the filtered projections

$$Q_\beta(s') = R'_\beta(s) * g(s) \tag{2.43}$$

using the filter kernel $g(s)$. To save computing time this convolution is often done as multiplication in frequency space.

Third: In the last step the filtered projections are back-projected by

$$f(r,\phi) = \int_0^{2\pi} \frac{1}{U^2} Q_\beta(s') \tag{2.44}$$

where $f(r,\phi)$ is the representation of objective function $f(x,y)$ in polar coordinates. The weighting factor $1/U^2$ is calculated from

$$U(r,\phi,\beta) = \frac{D + r\sin(\beta-\phi)}{D}$$

concerning the position of the point (r,ϕ) the reconstruction is calculated for.

A detailed derivation for this procedure can be found in Kak and Slaney (1999). The three steps were implemented for the FBP reconstruction used as a "first-guess" of the image. Then follows a reconstruction with an iterative reconstruction algorithm, that includes physical properties of the data acquisition, described in the next section. The iterative algorithm was used to include effects due to non-linear attenuation, which is not considered yet.

2.4.5 Iterative reconstruction algorithm

To include physical processes of the image acquisition process to account for beam-hardening during image reconstruction an algorithm described by DeMan *et al.* (2001) was implemented. The algorithm maximizes the log-likelihood

$$L = \sum_{i=1}^{I} (y_i \ln(\hat{y}_i) - \hat{y}_i) \quad , \tag{2.45}$$

where y_i is one of the I measured transmitted intensities and $\hat{y}_i$ is the expected transmission values, y_i is assumed to be a Poisson realization of $\hat{y}_i$.
This method of reconstruction starts with a distribution of attenuation coefficients μ_j –the "first guess"– and calculates the intensities on the detector by simulating the image acquisition process. The calculated $\hat{y}_i$ are compared to the measured values and the difference between both is back-projected to correct μ_j with the goal to maximize (2.45). This is done in an iterative procedure until the best values μ_j are found and (2.45) is nearly constant.
With a given distribution of the attenuation coefficient $\mu(x, y) = \{\mu_j\}_J$ described as a vector with $j = 1 \ldots J$ entries, the vector of projection data $\{\hat{y}_i\}_I$ is calculated from

$$\hat{y}_i = b_i e^{-\sum_j l_{ij}\mu_j} \quad , \tag{2.46}$$

where l_{ij} is a matrix that contains the cross section between the the i-th ray and the j-th pixel (sec. 2.4.6). For a given geometry the entries of the matrix are constant and can be calculated once at the beginning to reduce computing time. If the matrix is stored on the hard disk it has not to be recalculated for further reconstructions with the same underlying geometry.
To maximize (2.45) an update step for this iterative procedure is given by

$$\Delta\mu_j = \mu_j^{n+1} - \mu_j^n = -\frac{\frac{\partial L}{\partial \mu_j}(\mu)}{\sum_{h=1}^{J} \frac{\partial^2 L}{\partial \mu_j \partial \mu_h}(\mu)} \tag{2.47}$$

where n is the iteration number.
To include the effect of beam hardening instead of (2.46) the attenuation process is described in a more general way by

$$\hat{y}_i = \sum_{k=1}^{K} b_{ik} e^{-\sum_j l_{ij}\mu_{jk}} \quad , \tag{2.48}$$

that now accounts for the energy dependency of the attenuation coefficient. The energy spectrum b_{ik} of incoming photons is decomposed into K intervals and the attenuation μ_{jk} depends on the photon energy. Therefore, a model for the energy dependency of the attenuation coefficient must be introduced. In the used energy range ($E_{photon} < 150\,\mathrm{keV}$) the attenuation process is dominated by the photoelectric effect $\Phi(E)$ and Compton scattering $\Theta(E)$. The attenuation coefficient is now

$$\mu(E) = \phi\Phi(E) + \theta\Theta(E) \quad , \tag{2.49}$$

a superposition of both with ϕ and θ as weighting factors for each process. The photoelectric effect in the used energy range is approximated by

$$\Phi(E) = \frac{1/E^3}{1/E_0^3} \quad , \tag{2.50}$$

where E_0 is a reference energy. This approximation can be used for all materials that have no absorption edges in the used spectral range. The Compton scattering $\Theta(E)$ is described by the Klein-Nishina equation

$$\Theta(E) = \frac{f_{KN}(E)}{f_{KN}(E_0)} \qquad \text{with} \tag{2.51}$$

$$f_{KN}(E) = \frac{1+\alpha}{\alpha^2}\left(\frac{2(1+\alpha)}{1+2\alpha} - \frac{\ln(1+2\alpha)}{\alpha}\right) + \frac{\ln(1+2\alpha)}{2\alpha} - \frac{1+3\alpha}{(1+2\alpha)^2} \tag{2.52}$$

where $\alpha = E/511\,\mathrm{keV}$ and E_0 as reference energy.
With (2.49), (2.50) and (2.51) there is an approximation for the energy dependent attenuation coefficient. The coefficients ϕ and θ in (2.49) can be estimated from least square fitting the attenuation model to published $\mu(E)$ data (e.g., National Institute of Standards and Technology). From the equations (2.49)-(2.51) it is obvious that ϕ and θ represent the photoelectric and the Compton scattering part of the attenuation at E_0.

In a more practical way for digital processing, the discretization of (2.49) is written as

$$\mu_{jk} = \phi_j \Phi_k + \theta_j \Theta_k \quad , \tag{2.53}$$

where Φ_k and Θ_k represent the energy dependence of μ_{jk} with the approximations (2.50) and (2.51), ϕ_j and θ_j carry the material dependence with the dimension [L^{-1}]. The acquisition model (2.48) then becomes

$$\hat{y}_i = \sum_{k=1}^{K} b_{ik} e^{-\sum_j l_{ij}(\phi_j \Phi_k + \theta_j \Theta_k)} \tag{2.54}$$

and the number of unknowns is $2\,J$ (ϕ_j and θ_j) in contrast to $K\,J$ unknowns μ_{jk} in (2.48). This leads to a better convergence for the acquisition model (2.54) because of the reduced number of degrees of freedom.
To reduce the number of degrees of freedom again DeMan *et al.* (2001) assumed that the pair of values (ϕ, θ) for most materials lie near the piecewise linear ϕ-θ function defined by a set of base materials. This implies that the energy dependence of the attenuation has to be a linear combination of the energy dependences of two adjacent base materials. They now assumed, that for a set of base materials the again piecewise linear $\mu(E_0)$-ϕ curve and the $\mu(E_0)$-θ curve determine the values of ϕ and θ for any material.
Now, in (2.54) ϕ_j and θ_j can be substituted by the functions $\phi(\mu_j)$ and $\theta(\mu_j)$ and (2.54) becomes

$$\hat{y}_i = \sum_{k=1}^{K} b_{ik} e^{-\sum_j l_{ij}(\phi(\mu_j) \Phi_k + \theta(\mu_j) \Theta_k)} \tag{2.55}$$

and the number of degrees of freedom reduces to J. The functions $\phi(\mu_j)$ and $\theta(\mu_j)$ describe the monochromatic attenuation coefficient at photon energy E_0 in pixel j. The calculation of the j-projections in the exponent is very time consuming and therefore (2.55) is rewritten in a more efficient way by taking Φ_k and θ_k outside the summation

$$\hat{y}_i = \sum_{k=1}^{K} b_{ik} e^{-\left(\Phi_k \sum_j l_{ij} \phi(\mu_j) + \Theta_k \sum_j l_{ij} \theta(\mu_j)\right)} \tag{2.56}$$

resulting in the implemented acquisition model with two j-projections instead of K in (2.55).
The algorithm developed by DeMan *et al.* (2001) results by substituting (2.56)

in (2.45) and applying (2.47) which results in the following iteration instruction:

$$\mu_j^{n+1} = \mu_j^n + \Delta\mu_j^n \tag{2.57}$$

with

$$\Delta\mu_j^n = \frac{\phi'_j \sum_{i=1}^{I} l_{ij} e_i Y_i^{\Phi} + \theta'_j \sum_{i=1}^{I} l_{ij} e_i Y_i^{\Theta}}{\phi'_j \sum_{i=1}^{I} l_{ij} M_i + \theta'_j \sum_{i=1}^{I} l_{ij} N_i} \quad . \tag{2.58}$$

The explicit formulations for the used substitutions are shown on page 100 in eqns. (A.1) to (A.13) or in DeMan *et al.* (2001).
With the algorithm described above the reconstructed distribution $\mu(x, y)$ represents the monochromatic linear attenuation coefficient at $E = E_0$. Obviously each iteration requires four projections (projection of ϕ, θ, ϕ' and θ') and four back-projections (back-projection of $e_i Y_i^{\Phi}$, $e_i Y_i^{\Theta}$, M_i and N_i).
The initial values of μ_j^0 are calculated by a filtered back-projection as described in section 2.4.4.
The time needed for one reconstruction with $I = 1280 \times 600$ and $J = 512 \times 512$ and 15 iteration steps is about 30 min on a 3 GHz machine. The most time consuming processes are the four projections and back-projections. This calculations were parallelized and utilize the full computing power of the dual processor machine used to reduce computing time.

To demonstrate the effect of beam-hardening two reconstructed images are shown in fig. 2.7. The object in the images is a PVC phantom with 16 cm in diameter. Some structures were included in the previously homogeneous PVC disc. The right image was reconstructed with the filtered back-projection algorithm and the left with the iterative algorithm described above. The image that results from the filtered back-projection shows an increasing attenuation for increasing sample radius. When the X-ray beam enters the sample the photons with low energy are attenuated stronger than photons with high energy. The relative fraction of photons with high energy is increasing with increasing penetration depth of the beam. This is reflected in the image that shows high attenuation at the border. The right image in fig. 2.7 depicts the result of the iterative reconstruction algorithm that used the left image as "first-guess". Here the attenuation at the border is the same as in the center of the disc. The algorithm accounts for non-linear attenuation and therefore the effects due to this behavior vanish.

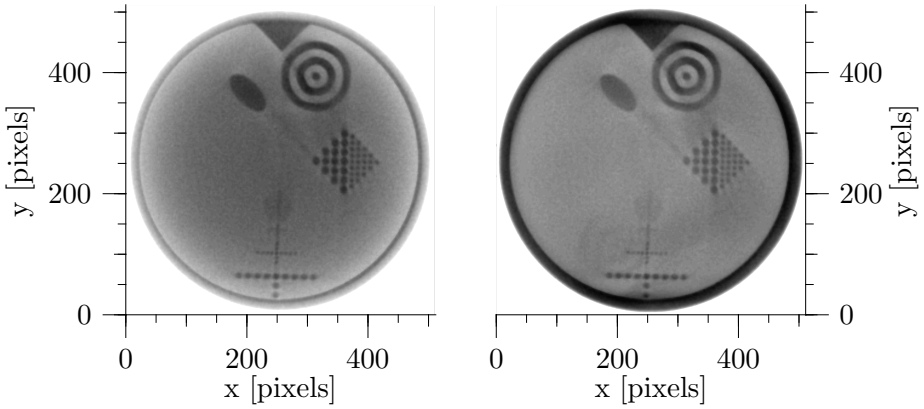

Figure 2.7: Reconstructed images of a PVC phantom with a diameter of 16 cm. The left image is reconstructed with the FBP algorithm. It is used as "first-guess" for the iterative reconstruction resulting in the right image. Both images are filtered with Gaussian filter ($\sigma = 1$, 3σ taken into account). x- and y-axis represent the pixel numbers of the reconstruction grid, with a pixel-size of $0.4\,\mathrm{mm}^2$. The grey levels indicate the attenuation coefficient (low attenuation: dark, high attenuation: bright).

2.4.6 Utilize the symmetry of the reconstruction problem

The projection matrix L with the elements $\{l_{ij}\}$ introduced in the last section can be very large. It contains the cross lengths of each possible path of the X-ray beam from the source to the respective sensor element on the detector and the pixels in the reconstruction grid. This cross lengths were found by implementing a ray-driven ray-tracing algorithm using a bilinear interpolation scheme (Joseph, 1982).
For a reconstruction grid with size $\mathrm{J} = \mathrm{U} \times \mathrm{U}$ and N measured projections with M sensor elements l_{ij} has in principle $\mathrm{I} \times \mathrm{J}$ entries, where $\mathrm{I} = \mathrm{M} \times \mathrm{N}$. In a standard reconstruction the reconstructed image is of size $\mathrm{U} = 512$ and measured data is $\mathrm{N} = 600$ and $\mathrm{M} = 1280$ for the detector used. The principle size of L in a double precision representation is at maximum $(\mathrm{I} \times \mathrm{J}) \cdot 8\,\mathrm{Byte} = 1.6 \cdot 10^{12}$ Byte. Most of the entries will be zero because a single beam can pass two pixels per row or column at maximum unless the interpolation scheme includes more pixels. With respect to the zero entries a sparse matrix scheme was implemented that stores the values in a compressed row storage format, where for each row

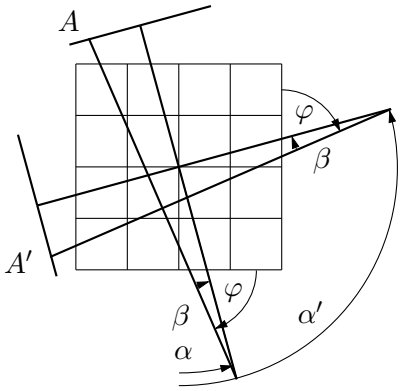

Figure 2.8: Sketch of the geometry of the reconstruction grid and one X-ray beam A at rotation angle α and fan angle β and the beam A' for the same fan angle and rotation angle $\alpha' = \alpha + \pi/2$. The angle of incidence of the beam φ is also the same for A and A'.

in L the number of non-zero entries, their positions in the respective row and their values are stored. This leads to a large size reduction of L, in the shown example to $6.3 \cdot 10^9$ Byte, still a huge amount of data that has to fit into the main memory of a computer. A next step in reducing size is to utilize the symmetry of the reconstruction matrix. As shown in fig. 2.8 the path of beam A' is similar to that of beam A. The difference between the two beams arises from the rotation of the sample by $\pi/2$. The weights for A' are already calculated for beam A and only their positions have changed. A similar symmetry exists for rotation angles that are π and $3/4\pi$ larger than α. A further reduction of the size of L by a factor of 4 follows. The size of L is now about $1.6 \cdot 10^9$ Bytes and fits into the memory of an ordinary computer. Another size reduction is possible, if necessary, using single precision numbers instead of double precision taking into account the symmetry of the fan beam.

L can be calculated for $\alpha = 0 \ldots \pi/2$ and further calculations for rotation angles $\alpha > \pi/2$ can use the same entries of L with respect to the symmetry. A forward projection means the transform of values x_j distributed like $\mu(x, y)$ into values $\tilde{x}_i$ that are ordered like in a sinogram. The generalization (x_j and $\tilde{x}_i$) is done because of the different quantities that are projected (ϕ, θ, ϕ' ,θ',

$e_i Y_i^{\Phi}$, $e_i Y_i^{\Theta}$, M_i and N_i). The forward projection is given by

$$\tilde{x}_i = \sum_{j=0}^{j=J-1} l_{ij} x_j \quad . \tag{2.59}$$

Using the reduced form of L, described before, the multiplication of (2.59) must be divided into four parts

$$\begin{aligned} \tilde{x}_i &= \sum l_{ij} x_j \\ \tilde{x}_{i+\frac{1}{4}I} &= \sum l_{ij} x_{(n-1-j \bmod n)n+j/n} \\ \tilde{x}_{i+\frac{1}{2}I} &= \sum l_{ij} x_{(n-1-j/n)n+n-1-j \bmod n} \\ \tilde{x}_{i+\frac{3}{4}I} &= \sum l_{ij} x_{(j \bmod n)n+n-1-j/n} \end{aligned} \tag{2.60}$$

where the index i runs over $i = 0, \ldots, \frac{1}{4}I - 1$ and n is the edge size of the squared reconstruction grid which contains the values x_j. The summation $\sum$ in all four parts always runs over all $j = 0, \ldots, J-1$. The division j/n is an integer division always rounded to the lower integer value of j/n. Obviously, the projection is split into four parts where the first part is the trivial case. The three others solve the problem of finding the correct entries in x_j, the rotating grid, that are involved in the respective projection (fig. 2.8).

The back-projection is given as the multiplication

$$x_j = \sum_{i=0}^{i=I-1} l_{ij} \tilde{x}_i \quad . \tag{2.61}$$

To do this in an effective way, too, (2.61) is also divided into four parts. The same matrix L as in (2.60) will be used to save computer memory. Therefore an adequate index handling is given as

$$\begin{aligned} x_j &= \sum l_{ij} \tilde{x}_i \\ x_{(n-1-j \bmod n)n+j/n} &= \sum l_{ij} \tilde{x}_{i+\frac{1}{4}} \\ x_{(n-1-j/n)n+n-1-j \bmod n} &= \sum l_{ij} \tilde{x}_{i+\frac{1}{2}I} \\ x_{(j \bmod n)n+n-1-j/n} &= \sum l_{ij} \tilde{x}_{i+\frac{3}{4}I} \end{aligned} \tag{2.62}$$

where the summation $\sum$ now runs over all $i = 0, \ldots, \frac{1}{4}I - 1$. n and j/n are used as described above.
The splitting of (2.59) and (2.61) offers the possibility for an effective parallel implementation to speed up the time consuming calculations. Note, the shown implementation is only fast if shared memory is used and all processes can access the entries l_{ij}. If not the huge amount of data still stored in l_{ij} has to be transfered to the accessible memory of the single processes and computing time increases again.

2.5 Vertical water content profiles

To monitor the vertical distribution of water within a sample the line sensor and the focus of the X-ray tube were placed in the same vertical position, at the bottom of the column. Then both were moved synchronously from bottom to top of the sample. During the movement the intensity on the detector is measured at several positions. The positions and the velocity of the movement has to be adjusted to useful values. The result of such a measurement is a vertical intensity profile $I(z, i)$, where z is the vertical position of the detector and i denotes the number of the pixel on the detector. The intensities for each pixel have to be corrected for the dark current of the respective detector pixel. The dark current must be determined in an independent measurement. With the known I_0 signal, also measured independently, the attenuation A can be calculated as the product of the effective attenuation coefficient μ_{eff} and the length of path of the photons through the material d by

$$A(z) = \mu_{eff} d = \ln\left(\frac{I_0}{I(z,i)}\right) \quad . \tag{2.63}$$

Here the attenuation A is the sum of length-fraction weighted attenuations of the different components and therefore depends on the water content and the detector position, hence

$$\begin{aligned} A(z) = A(\theta(z)) =& (1-\phi)\mu_{matrix} d + \theta(z)\mu_{water} d \\ &+ \mu_{wall} d_{wall} + (\phi - \theta(z))\mu_{air} d \quad , \end{aligned} \tag{2.64}$$

where μ_{matrix}, μ_{water}, μ_{wall} and μ_{air} are the attenuation coefficients of matrix, the column wall, water and air, respectively, d and d_{wall} are the diameters of the column and the thickness of the column wall, respectively, ϕ is the porosity and $\theta(z)$ the vertical distribution of the volumetric water content. The last

term in (2.64) can be neglected taking into account that the attenuation coefficient of air is two orders of magnitude lower than that of the other materials present (Hubbel, 1982). With the different measurements for the dry and the fully water saturated sample the volumetric water content profile $\theta(z)$ can be calculated from

$$\theta(z) = \frac{A(\theta(z)) - A_d}{A_s - A_d}\,\theta_s \tag{2.65}$$

where A_d is the value calculated using (2.63) of the dry sample, A_s of the saturated sample and θ_s is the saturated volumetric water content assumed equal to porosity.
In summary it can be ascertained that the vertical water content of a column can be determined if the attenuation profile for the dry and saturated column is available without the knowledge of absolute values for the attenuation coefficients for the used materials.

$$\begin{aligned} A_x - A_y &= \ln\frac{I_0}{I_x} - \ln\frac{I_0}{I_y} \\ &= \ln\frac{I_y}{I_x} \end{aligned}$$

shows that in this calculation even the I_0 signal is not needed.

2.6 Numerical simulations

During this work two solvers for Richards' equation were used. One was used for inverse modeling the outflow data measured with multi-step outflow and the other for forward simulations to predict the distribution of water within the sample and the cumulative outflow.

eshpim The package was written by Zurmühl (1994, 1998). It was used to estimate the van Genuchten parameters from measured outflow data. The input needed by the solver is the pressure at the lower boundary, the amount of outflow as function of time and if present the matric potential at some height of the sample measured by a tensiometer. The hydraulic parameters are determined from these data by solving the inverse problem of Richard's equation using a one-dimensional, fully-implicit, finite difference mixed formulation (Celia *et al.*, 1990) with a Levenberg-Marquardt algorithm to optimize the parameters. The code also allows the usage of a bi-modal van Genuchten parameterization (Zurmühl and Durner, 1998). A homogeneous material model is used to discretize the sample.

The porous plate used at the bottom of the sample is also included into the inverse modeling procedure.

$\mu\varphi$ Forward simulations for homogeneous and heterogeneous structures were done with the computer model $\mu\varphi$ (Ippisch, 2004) which solves Richards' equation using a cell-centered finite-volume scheme with full-upwinding in space and an implicit Euler scheme in time. Linearization of the non-linear equations is done by an inexact Newton-Method with line search. The linear equations are solved with an algebraic multigrid solver. For the time solver the time step is adopted automatically. The used structure model can be homogeneous as well as heterogeneous. Supported structures can be given in 1D, 2D, 3D and as distributions of hydraulic parameters with cylindrical symmetry.

3 Experimental setup

In this chapter, as indicated by its title, the single components of the experimental setup will be described in detail. The two main parts are the X-ray system and the multi-step outflow setup.

3.1 X-ray system

The format of the experimental setup of the X-ray system contains three major parts: the X-ray source, the detector and the mechanics to move and rotate the sample. Additionally, a method of finding the relative positions of detector, sample and tube is presented. The bow tie used filter to homogenize the intensities at the detector will also be introduced.

3.1.1 X-ray tube

The X-ray source used is a medical X-ray tube (model: *Phillips OPTIMUS RAD X-ray Generator* with *SRO 0951/ROT 350 tube housing*). The tube has a rotating tungsten target doped with rhenium. The accelerating voltage can be varied between 40 keV and 150 keV at several discrete values. Also the tube current can be adjusted to fixed values within a range from 100 µA to 50 mA. The focus point on the anode can be switched, in principle, between 0.3 mm and 1.0 mm. During this work only the larger focus point was used. With the small spot the anode heats up much faster and measurements become uncomfortable, long times between two measurements arise, where the tube has to cool down. In front of the output window of the tube a slit is installed to collimate the beam. The highest intensity is emitted in a horizontal plane with an opening angle of $\pm 11^\circ$ around the perpendicular output direction.
Maximum time for one shot of the tube is 16 s, after that time the tube shuts down. This time limits the measurements, and measurements that need more time have to be split into intervals of 16 s. The other temporal limit of the tube is the warming of the anode. Approximately, six times in series high power measurements (e.g. 16 s beam time, 140 keV acceleration voltage, 20 mA tube current) are allowed, then the tube needs to cool down for some minutes

up to half an hour depending its history. With low output power the tube can be operated nearly continuously. For all measurements a tradeoff has to be made between the temporal resolution and the intensities measured on the detector. For high contrast images the signal on the detector should be as large as possible and often temporal behavior neglected.

3.1.2 Detector

To detect transmitted X-ray photons a CCD (Charge Coupled Device) line sensor was used during this work. A CCD is a light sensitive semiconductor capacitor. In principle, there are three layers starting with p-doped substrate followed by a transparent insulator and a conductor, called gate, on top. A positive voltage is applied to the gate with the effect that charge carriers are pushed away in the substrate near the insulator. There, a charge free area develops. For incoming photons the upper two layers, gate and insulator, are transparent and the photons are absorbed in the substrate (photoelectric effect). Electron-hole pairs are produced and separated by the applied voltage where the electrons are collected in the charge free area near the insulator and the defect charge carriers in the substrate. Each pixel retained as a capacitor where the amount of produced electron-hole pairs is proportional to the number of incoming photons. After some exposure the charge of the capacitor is read out and the next exposure may occur.
The electron-hole pair production also happens as a result of thermal influence. This leads to a background charge on the capacitor called dark current. One possibility to minimize this effect is to cool the CCD pixels. For correct intensity data the dark current has to be measured and subtracted from intensity data. To produce visible photons, the CCD is sensitive for, a scintillator is placed in front of the CCD chip. It absorbs the X-ray photons and produces secondary photons with lower energies. The low energy photons are now in the energetic range that to be detected by the CCD.

The detector used during this work was a plane CCD line sensor (*Hamamatsu C7390*) build up from 1280 squared CCD pixels with 0.4 mm edge length.
The charge of each pixels is amplified separately and the information after digitizing with a 12 bit A/D-converter transfered to a frame grabber board in a separate computer. Originally the detector is used for quality control at assembly lines noticeable in a parameter called line speed LS that controls the exposure time t_{ex}. It can be switched in the range of $t_{ex} = 0.6\,\text{ms}, \ldots, 24.0\,\text{ms}$

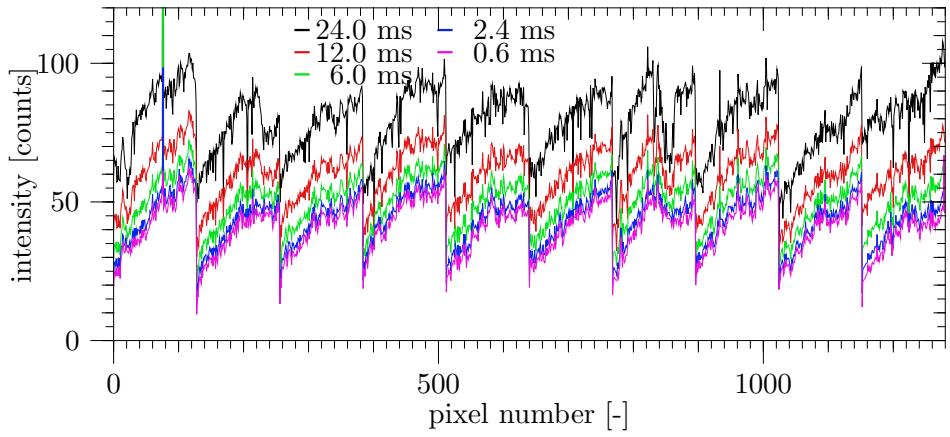

Figure 3.1: Counts on the detector measured without tube activity for different exposure times shown in different colors.

where t_{ex} is calculated from the line speed by

$$t_{ex} = 24\,\text{ms} \cdot LS^{-1} \tag{3.1}$$

and LS reaches values form 1.0 to 40.0 in steps of 0.1.
No pre-processing was done by the detector unit, e.g. dark current correction. The dark current signal was recorded separately and taken into account during data processing. In fig. 3.1 an example for dark current spectra is displayed for different exposure times. The spectra show underlying sub-structures of 128 pixels width due to the production process, where the 1280 pixels are put together from ten 128 pixel elements. Also one "hot" pixel can be observed at position 73 with a dark current intensity more than five times larger than the rest. The value of this pixel is set to the linear average of the two surrounding pixels during data processing.
From fig. 3.1 it is apparently that the dark current signal consists of the sum of an constant value and one that is proportional to exposure time. This was tested for dark current data $I_{dark}(i, t_{ex})$ calculated as the average value of 200 single measurements for each exposure time t_{ex}. A linear regression for each single pixel was performed to find the two free parameters $a(i)$ and $b(i)$ of the linear description

$$I_{dark}(i, t_{ex}) = a(i) + b(i)t_{ex} \qquad .$$

The constant part of the linear function where $t_{ex} = 0$ was found to be nearly identical to the measured dark current spectrum at $t_{ex} = 0.6\,\text{ms}$. The factor of

proportionality $\bar{b}$, the average value for all $b(i)$, was $\bar{b} = (1.67 \pm 0.38)$ counts/ms. The averaged stability index $R^2 = 0.998$ is very close to 1 with an uncertainty of $\approx 7 \cdot 10^{-5}$. As expected the dark current in each pixel is proportional to t_{ex} in the used range of t_{ex}. In principle it is now possible to calculate the dark current intensity for all exposure times, but the faster way, chosen here, was to record dark currents for each exposure time used in the respective experiment.

3.1.3 Mechanics

The mechanical system consists of six axis, that can be moved separately or together. Detector and tube are allowed to move vertically. Additionally, the detector can move in the horizontal direction to change its distance to the tube. The other three axis control the sample-tube distance, the rotation of the sample and its lateral position.
Since there is no reference point or fixed distance in this system, a routine was developed where the system can measure all the important positions itself.
Therefore a metal pin is placed on the sample disc and the projected shadow of the X-ray beam is recorded for one complete rotation of the disc. Then the pin is placed on a second position with a known distance d to the first position (fig. 3.2). The projected position during a second rotation is also monitored. The measured traces of the pins $y_{1,2}(\alpha)$, with rotation angle α and the center of the detector $y_{1,2}(\alpha) = 0$, are described by

$$y_1(\alpha) = \frac{a(b + r_1 \sin(\alpha + \varphi))}{c + r_1 \cos(\alpha + \varphi)} \tag{3.2}$$

for the first pin position and

$$y_2(\alpha) = \frac{a(b + r_2 \sin(\alpha + \varphi \pm \arccos(\frac{r_1^2 + r_2^2 - d^2}{2 r_1 r_2})))}{c + r_2 \cos(\alpha + \varphi \pm \arccos(\frac{r_1^2 + r_2^2 - d^2}{2 r_1 r_2}))} \tag{3.3}$$

for the second. The distances for a, b, c, r_1 and r_2 are depict in fig. 3.2. The phase shift φ occurs from the random positions of the pins. The "$\pm$" sign in (3.3) accounts for the non-unique position of the second pin. There are two positions allowed for the second pin that have the same distance r_2 and d (see right side in fig. 3.2).
After recording the two traces, they are fitted simultaneously by (3.2) and one of the two parameterizations in (3.3). With this procedure it is possible to determine the distance from the focal point inside the tube to the detector pixel

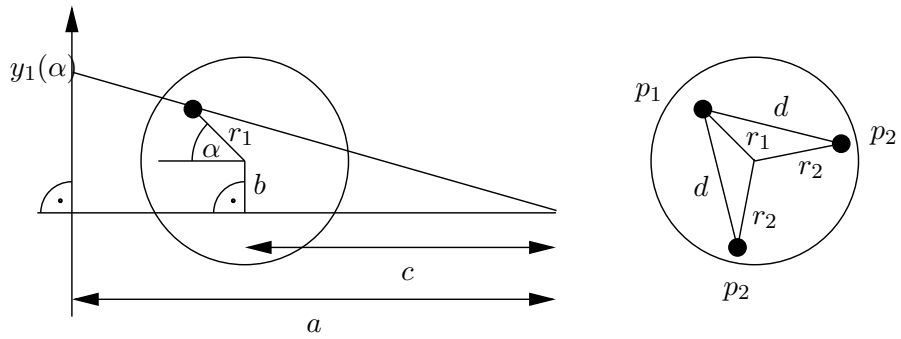

Figure 3.2: Description of the parameters used in (3.2). The position $y_1(\alpha)$ on the detector describes the projected shadow of a pin placed on the rotating disc in distance r_1 from its center. The distance a is the spacing between the tube and the detector, b the perpendicular distance from the center of the disc to the connecting line between tube and center of the detector, c is the spacing from tube to the intersection point of b and this connection line. The tube is on the right side and one ray is shown, that starts at the X-ray source and ends at $y(\alpha)$ on the detector.
The right part shows two possible second positions for the pin p_2 with the same distance d to the first pin position p_1. The distances of p_1 and p_2 to the center of rotation are shown as r_1 and r_2.

array a and to the center of rotation c from the easy and precise measurable value d. Also the off-axis position b for the center of the disc will be found and can be adjusted.
The vertical positions of tube and detector must be found during the experiment by scanning over prominent absorbers at well known positions.

3.1.4 Control software

The movement of the mechanical parts of the setup, the image acquisition, and the tube and detector settings are controlled by a single computer program. There is one parameter file which contains the values that are processed by this program. It supports different modes of image acquisition. The easiest is simple reading of the measured intensity on the detector with and without tube activity used to generate reference data and dark current information. Also reading the detector values during synchronously moving of the detector and

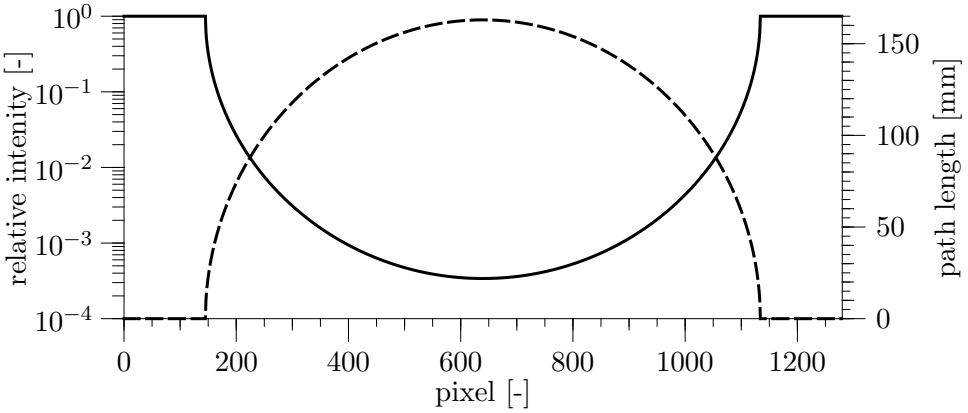

Figure 3.3: The solid line shows the relative intensity on the detector for a homogeneous circular absorber with the attenuation coefficient of $\mu = 0.049\,\mathrm{mm}^{-1}$ on a logarithmic scale. As dashed line the length of path the X-ray beam explores in the sample is indicated for a sample with a radius of 81.5 mm (related to right $y-$axis).

tube is possible. In a third mode the intensities are monitored while rotating the sample holder. Another mode is used to generate tomographic data, which is used to reconstruct slice information.
Two additional modes were implemented to control the motors separately and adjust the detector settings. No fully automatic scan series are designed because the temperature of the system cannot be monitored by the control software until now and has to be checked by eye.

3.1.5 Bow tie filter

The used fan beam geometry, together with cylindrical samples, comes up with the problem of an early saturation of detector pixels at the boundary. The emitted X-ray intensity is, in the ideal case, homogeneous within the fan beam. Without a sample a constant spectrum should be observed on the detector. This homogeneity is disturbed by the sample, where the X-ray photons have to pass the sample on paths whose length depends on the fan angle.
Assuming a homogeneous sample with a circular cross section, placed with its center on the connecting line of the tube focus and the center of the horizontal detector. The recorded intensities will vary from the largest values at the outer pixels to the lowest, located at the center of the detector. In fig. 3.3 a calcu-

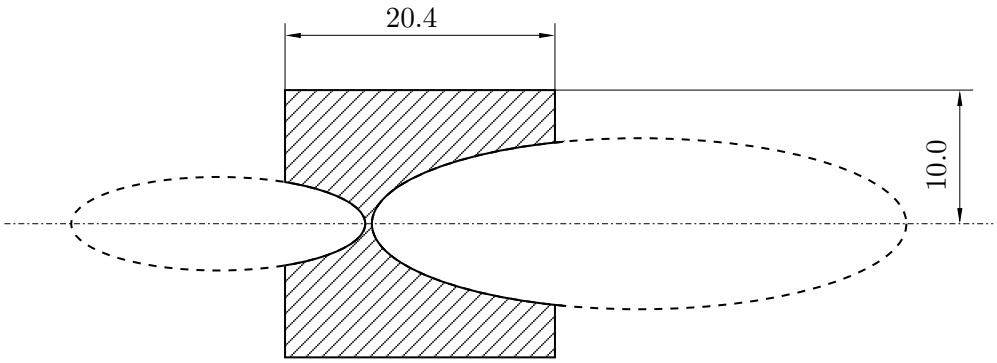

Figure 3.4: Sketch of used bow tie filter from a rectangular PVC plate 20.4×20.0 cm edge length.

lated spectrum together with the length of path is shown. The detector used has a dynamic range of 12 bit, i.e. values from 0 to 4095 are detectable. In the shown geometry the intensity range covers three orders of magnitude and the detector pixels aside reach saturation, while pixels in the center stay far away from saturation. To disband internal changes in the sample a longer exposure time of the center pixels is needed without saturating pixels far away from the center.
As in clinical applications, this problem was solved by creating a filter that has the inverse shape of the sample placed between the X-ray focus and sample. The length of path for the X-ray beam through this filter is short in the center and large for rays with larger fan angles. It was made of polyvinyl chloride (PVC) that is easy to process and has an attenuation coefficient $\mu_{PVC}(80\,\mathrm{keV}) = 3.231 \cdot 10^{-2}\ \mathrm{mm}^{-1}$ (National Institute of Standards and Technology, 2004), that is in the range of the effective attenuation coefficient for the studied materials.
The filter itself was made of a rectangular plate where two elliptic cut-outs were milled out (fig. 3.4). The lengths of the two axis that describe an ellipse were found by fitting the length of path trough the filter to the inverse path length through the sample.

The complete dynamic range of the detector can now be used to detect changes within the sample instead of the thickness variation of the sample at different fan angles. In principle the filter works only perfect for one specific geometry of tube-detector and tube-sample distance. For other distances not to

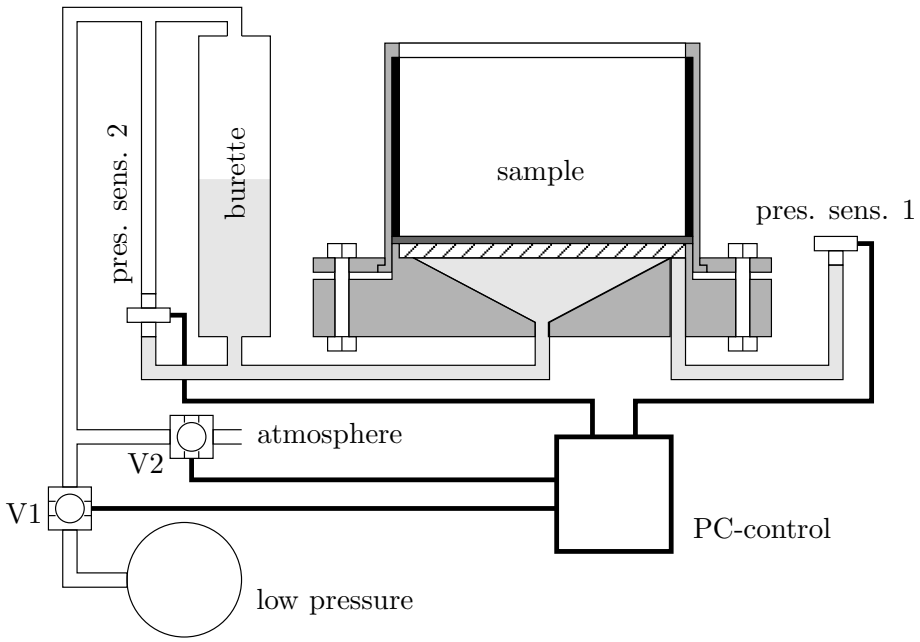

Figure 3.5: Sketch of the multi-step outflow setup. Shown is the sample holder and its connections to control the pressure at the lower boundary. The water outflow is caught in the burette and with the pressure sensor 2 its amount is measured. The pressure at the lower boundary is detected with pressure sensor 1. With a computer the pressure at the lower boundary is measured and adjusted by readjusting the pressure via the magnet valve V1 connected to a reservoir of low pressure and V2 connected to atmospheric pressure.

far away from these positions it still can prevent skirting pixels of the detector from saturation.

3.2 Multi-step outflow system

To study flow dynamics in porous media it was necessary to control the boundary condition of the samples during X-ray attenuation measurements. Therefore the setup to control pressure and monitor outflow was installed beside the X-ray setup.
The multi-step outflow system used is a traditional setup (fig. 3.5), where the

pressure in the water phase is controlled at the lower boundary of the sample. Typical samples are 10 cm high cylindrical columns with 16.3 cm in diameter. The sample holder is a PVC tube that can be filled with artificial samples or undisturbed soil columns. At the bottom of the column a porous plate of sintered glass is placed together with an air-proof, but permeable to water, membrane on top. The membrane seals the lower boundary for gas flow and allows only the water flow out of and into the sample.

In fig. 3.5 a sketch of the multi-step outflow setup is shown. The pressure in the water phase, at the lower boundary, is measured with a pressure sensor (pres. sens. 1) mounted in hydraulic contact with the lower end of the porous plate. Pressure is monitored with a computer and adjusted by two magnet valves, one connected to a low pressure reservoir (V1) and the other to the atmosphere (V2). The water outflow is collected in a burette, and its amount is quantitatively determined from the diameter of the burette and the height of the water column measured with a second pressure sensor (pres. sens. 2). The two pressure sensors were calibrated before each experiment and work with an accuracy < 50 Pa. The pressure control allows low pressures at the lower boundary down to 80 kPa (≈ -200 cm height of a water column). The system is working stand-alone and MSO experiments taking very long time are possible.

The sample holder shown in fig. 3.5 is a redesign of the holder traditionally used in our group. This was necessary to combine the MSO experiments with X-ray measurements. In contrast to the new holder the old one has different PVC thicknesses at the bottom, which disturbs the X-ray measurements in this region. The modified holder has constant thicknesses in the parts that are passed by X-rays.

4 Results and discussion

The experimental setup described in the chapter before was used to perform several experiments with the aim to illuminate and utilize the internal behavior of porous samples concerning water flow. The measured water content profiles will be compared to predictions based on Richards' equation together with the water retention curve described by van Genuchten (1980). This is used to study the validity of Richards' equation for different boundary conditions. From measured X-ray data the internal structure of a sand sample is obtained. It was found to be weakly layered. Simulations based on a layered material model can predict the measured outflow data as well as the internal distribution of water. The present setup also allows recording tomographic images that can be used to study the structure of natural and artificial samples to test them for heterogeneity or identify rough structures.

4.1 Measurement of the soil water retention curve with X-ray attenuation

In soil science one of the most important "material parameters" is the soil water retention curve $\theta(h)$, the relation between the water content and the matric potential. There are different ways to measure that curve. One is the pointwise measurement of the water content within a sample, e.g. gravimetrically, for different potentials. This is very time consuming because the system needs a long time to reach hydrostatic equilibrium depending on the water content and the material. Especially for clay and loamy material this time can be a few days. An other method is the inverse parameter fitting of the outflow during a multi-step outflow experiment to estimate the parameters for the used model of the water retention curve. In the case of a van Genuchten like curve the parameters α and n have to be estimated. In this chapter, a method is demonstrated to access this curve directly for coarse materials (Bayer *et al.*, 2004). Therefore, a X-ray attenuation measurement of the vertical distribution of water and a multi-step outflow experiment was performed on a sand column.

4.1.1 Sample preparation

For this experiment sand was filled in a PVC tube of 10 cm height and with a radius of 8.15 cm. The grain size of the sand ranges from 0.63 mm to 1.25 mm. To prevent air entrapments the water level in the column was adjusted during the filling process such that it was always near the surface of the sand. With this method nearly no air will be entrapped, and the sample is completely water saturated at the beginning of the experiment. The top end of the sample was covered with a PVC plate to reduce the soil-atmosphere moisture exchange to minimize evaporation. This cover did not seal the sample such that the pressure control at the lower boundary was not affected by it.
The porosity of the sample was determined as $\phi = 0.396 \pm 0.002$ from its volume and the mass and density of the used sand. In a separate experiment, the saturated hydraulic conductivity was measured by the falling-head method (Klute, 1986), and results to $\mathsf{K}_s = 14\,\mathrm{m/h}$.

4.1.2 Measurement protocol

Starting with the completely water saturated sand column a vertical X-ray attenuation profile of the sample was recorded as reference. The horizontal line sensor and the X-ray tube were moved from the bottom to the top of the sample synchronously. To desaturate the sample it was mounted in a external multi-step outflow setup and a fixed potential of $h_{LB} = 3\,\mathrm{cm}$ was applied at the lower boundary for 20 hours. Earlier multi-step outflow experiments showed that after this time hydrostatic equilibrium has been established. Then sample was brought back to the X-ray setup and scanned again.
To estimate the hydraulic parameters of the material a traditional multi-step outflow experiment (van Dam *et al.*, 1994) was performed with the same sample. Finally the column was dried in an oven for five days at 50°C, to record the second reference scan. The relatively low temperature was chosen to prevent damage to the surrounding PVC parts of the column. During drying the weight of the column was monitored until it remained constant.
The X-ray measurements are used to calculate the vertical water content distribution $\theta(z)$ as described in chapter 2.5. With this profile the hydraulic parameters of the van Genuchten parameterization can be estimated as shown in the next section.
Before drying the sample a multi-step outflow experiment was run with the same sample to estimate the hydraulic parameters for further comparison. The column was saturated again by rising the water table slowly. For the multi-step

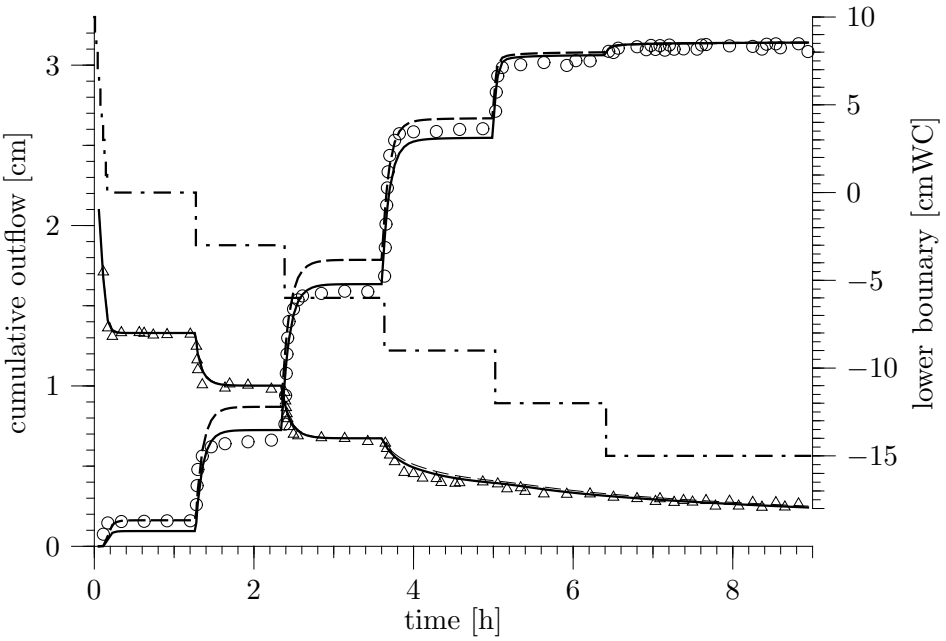

Figure 4.1: Measured multi-step outflow data (cumulative outflow: circles, matrix potential measured with a tensiometer 8 cm above lower boundary related to right y-axis: triangles) during desaturation (pressure at lower boundary related to right y-axis: dash-dot line) and the prediction using the van Genuchten parameters estimated by X-ray attenuation measurement (dashed line). Additionally the best-fit of the model (solid line) is shown. The fitted and predicted curves for tensiometer data are on top of each other.

outflow experiment the setup described in 3.2 was used, with the distinction that the X-ray setup was not present. The initial lower boundary condition of the experiment was $h_{LB} = -\frac{\psi_m}{\rho_w g} = -10\,\text{cm}$ where ψ_m is the matric potential, ρ_w the mass density of water and g the acceleration of gravity. Then, the pressure at the lower boundary was decreased (fig. 4.2) in ten steps of $\Delta h_{LB} = 1\,\text{cm}$ to $h_{LB} = 0\,\text{cm}$ each step with one minute duration. Afterwards, there follow five steps of about one hour duration and $\Delta h_{LB} = -3\,\text{cm}$. The measured outflow curve is shown in fig. 4.1. The van Genuchten parameters were estimated by inverse modeling the outflow data using *eshpim* (sec. 2.6). The best-fit outflow curve and the found parameters are given in fig. 4.1 and tab. 4.1.

Table 4.1: Parameters determined by fitting the van Genuchten parameterization to the pressure-saturation relation measured by X-ray attenuation and from solving the inverse problem for the multi-step outflow data. Uncertainties are calculated using the χ^2-statistics as described by Press *et al.* (1992).

parameter	X-ray att.	MSO-Fit
n [-]	10.7 ± 0.1	11.6 ± 0.2
α [10^{-2}cm^{-1}]	9.95 ± 0.01	9.46 ± 0.04
θ_r [-]	0.08 ± 0.01	0.09 ± 0.01

4.1.3 Estimation of the van Genuchten parameters from vertical water content profiles

If the vertical water content distribution $\theta(z)$ of a porous medium can be measured and the sample is in hydrostatic equilibrium and the material follows the parameterization of van Genuchten it is possible to estimate the parameters n and α. In hydrostatic equilibrium, where the matric head h is constant, the vertical z-axis represents a h-axis, too. Thus, the $\theta(z)$ measurement will become a description of $\theta(h)$. These values can be fitted by the van Genuchten parameterization, hence

$$\theta(h) = \theta_r + (\theta_s - \theta_r)(1 + (\alpha h)^n)^{-1+1/n} \tag{4.1}$$

while n, α and θ_r are free fitting parameters.
This works if the h-range is accessible in a sufficient interval. If not , $\theta(z)$ has to be measured at different pressures at the lower boundary to shift the water content profile through the sample and merge the profiles at the correct points. In fig. 4.2 the vertical water content profile recorded in hydrostatic equilibrium together with the fitted van Genuchten parameterization is shown. The shown profile was taken at $h_{LB} = 3\,\text{cm}$ at the lower boundary. Thus, an interval of $h = 3, \ldots, 13\,\text{cm}$ was accessible. In the lower part of the curve the X-ray signal was disturbed by the sample holder. The PVC wall was about five times thicker than in the upper part of the sample because the redesigned holder presented in sec. 3.2 was not available at this time. Therefore, the signal to noise ratio was reduced in this range.
The upper part of the sample between $h = 11.5, \ldots, 13.0\,\text{cm}$ was affected by changes in the bulk density at the top of the sample. These data were excluded

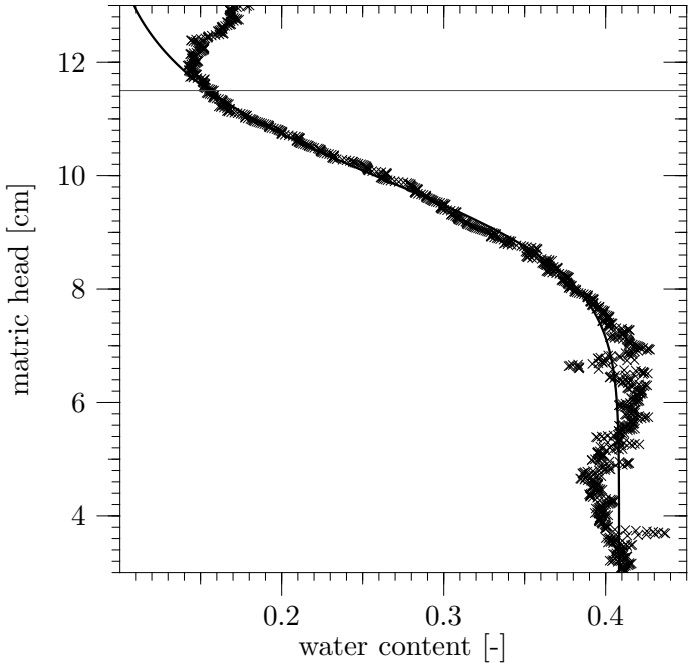

Figure 4.2: Measured vertical water content profile (symbols) within the sample at $h_{LB} = -3\,\text{cm}$ extracted from X-ray attenuation profiles. The y-axis show the sample height from bottom to top in hydrostatic equilibrium and is therefore also a matric head axis. The solid line is the fitted van Genuchten parameterization. Data above the line at $h = 11.5\,\text{cm}$ were affected by changes at the sample surface and excluded from further evaluation.

from further analysis. Optimal parameters n, α and θ_r were determined using the *non-linear least square fit* routine implemented in *Microcal Origin 6.0* (Microcal, 1997) and are shown in tab. 4.1.

4.1.4 Results of van Genuchten parameter estimation from X-ray attenuation profiles

Fitting the vertical water content profile results in a set of van Genuchten parameters. The measured curve is well represented by this parameterization. The value obtained for the parameter n is in good agreement with the value measured by multi-step outflow. The difference of the parameter α can be ex-

plained by an uncertainty in the pressure at the lower boundary. The parameter α^{-1} is associated with the air-entry pressure, the pressure for which air can enter the sample first and the largest pores drain. For the X-ray measured profiles is was $\alpha_X^{-1} = 10.05\,\text{cm}$ and from multi-step outflow data $\alpha_{MSO}^{-1} = 10.57$ was determined. This means, that an uncertainty in pressure at the lower boundary of 0.5 cm can explain this difference. The potential at the lower boundary has to be controlled very accurately. The pressure at the lower boundary can be controlled with a accuracy $\pm 0.2\,\text{cm}$ with the setup used. Thus, for a correct parameter estimation for α_X the pressure at the lower boundary has to be controlled in a more accurate way. At the time when this experiment was done there was no possibility to control the pressure during the X-ray measurements. The sample was prepared and drained with a fixed lower boundary condition, then sealed at the bottom and transfered to the X-ray setup.
For coarse homogeneous materials the method of estimating van Genuchten parameters from X-ray attenuation profiles can be a fast alternative tool to the traditional, time consuming methods.

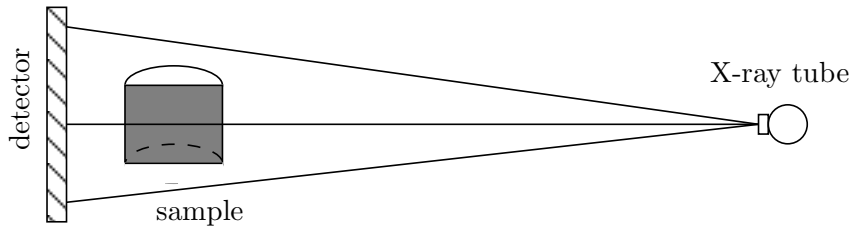

Figure 4.3: Experimental setup to record vertical attenuation profiles with high temporal resolution. The detector is mounted vertically and with each reading process from the detector one attenuation profile through vertical slice of the sample (grey shaded area) is taken.

4.2 Water imbibition monitored with high temporal resolution

Monitoring the vertical water distribution as shown in the section before opens the possibility to have a deeper look in temporal dependencies of the water retention curve.

4.2.1 Material, method and setup

The measurement of one vertical water content profile as shown in section 4.1 was done in $\approx 32\,\mathrm{s}$. To look at changes in water content during imbibition a much higher sampling rate is needed. Instead of scanning the sample from bottom to top by moving detector and X-ray tube synchronously the detector was rotated by 90° and the tube was placed at a fixed position at half height of the sample (fig. 4.3) . With this geometry X-ray attenuation profiles of one slice through the sample can be taken at frequencies up to 10 Hz. This increase in temporal resolution is associated with a loss of spatial resolution. In the used geometry slices through the sample project the whole sample height onto 270 pixels of the detector. At half height of the sample the spatial resolution is equal to the pixel size of the detector and decreases towards the top and bottom of the sample, due to the fan beam geometry.
The used sample was a column of sintered borosilicate glass of 10 cm height and 7.5 cm radius. The reason of using this material was the rigid pore space in contrast to sand, where the grains can move because of capillary forces during the experiment. Porosity was given to $\phi = 0.40$ according to the manufacturer. A PVC tube was also not necessary since the material was rigid, but to prevent

unwanted flow of water and air it was coated with silicone. The bottom of the sample was mounted on a plexiglass base and the upper end was open to the atmosphere. With this setup the flow is forced in the vertical direction.
Initially, the sample was oven-dried. Recording X-ray transmission data started immediately after the water phase was connected to the bottom of the column. Because of the limited beam-time of the tube, data were collected in bunches at increasing time intervals. Within the bunches measurements are separated by 1 s. Data recorded at times between this 1 s interval was used to average to increase the signal to noise ratio. The reference measurement of the dry and fully saturated sample are taken at the beginning, before water enters the sample, and at the end, respectively. For the second reference profile the sample was saturated in an exsiccator to reach full saturation.
The vertical water content was determined from the recorded attenuation profiles by correcting measured data $I(z)$ for its dark current and calculating the attenuation $A(z) = \ln(I_0/I(z))$. Together with the two reference measurements the volumetric water content at position z is calculated by (2.65).

4.2.2 Results and discussion

Vertical water content profiles at different times during imbibition are shown in fig. 4.4. During the first thirty minutes the water content changed rapidly and reaches hydrostatic equilibrium after some 16 hours. Fig. 4.5 reveals that dynamics of the capillary rise cannot be described by Richards' equation. It would predict full saturation at bottom from the point where the water table is connected to the sample. The measurements show that the sample was not saturated immediately at the bottom. Saturation increases fast at the beginning and rather slowly to the end. This dynamics of capillary rise into the dry sample may be described by two processes. An initial fast imbibition leading to a water content of $\theta = 0.29$ after fifteen minutes (right contour plot in fig. 4.4), followed by a second process that increases the water content at the bottom slowly to the stationary value of $\theta = 0.35$. This may result from the loss of continuity in the air phase during imbibition. In the beginning water enters the column rapidly and fills the pores with small diameters faster than the larger ones because of stronger capillary forces. Water can flow around some pores quickly and cut off the gas phase. This leads to air entrapments from which the air can remove by slowly bubbling through the overlying water barrier as pressure in the air phase increases. However, some fraction of the air cannot leave the sample in this way and stays in it as residual air for a long time. The volume fraction of residual air here, was about 0.05 the differ-

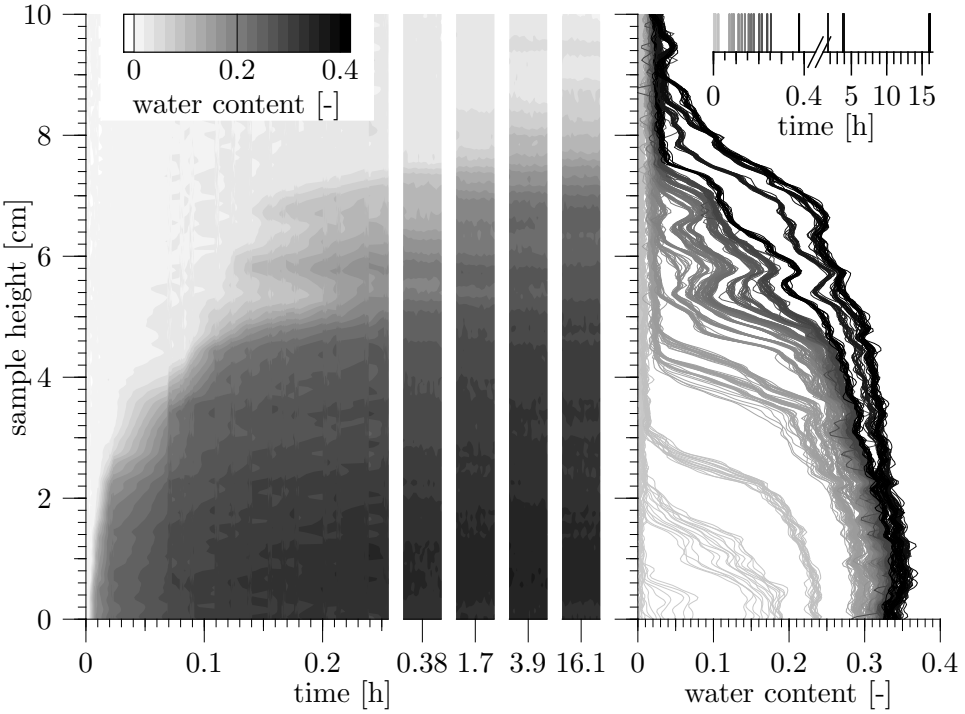

Figure 4.4: The contour plot shows vertical water content profiles at different points in time of the imbibition. Water content itself is represented as different grey values. The four single bars show the contours at much later times taken in bunches of 16 s length. The graph on the right side shows the same data with different axis. Here the x-axis is the water content and time is coded in grey values.

ence between the measured and saturated water content at the bottom. This corresponds to a residual air saturation of 12% of the pore space. This phase will disappear only by exceedingly slow diffusion of air through the water phase.

This illuminates the complexity of the multi-phase behavior in porous media. Richards' equation cannot describe the imbibition into a dry sample even though the air phase is continuous at the beginning. This is shown by a forward simulation with $\mu\varphi$ (sec. 2.6) of this behavior, depict in fig. 4.5 where the vertical water content profiles at different times of the imbibition are drawn. The hydraulic parameters were determined in a separate multi-step outflow

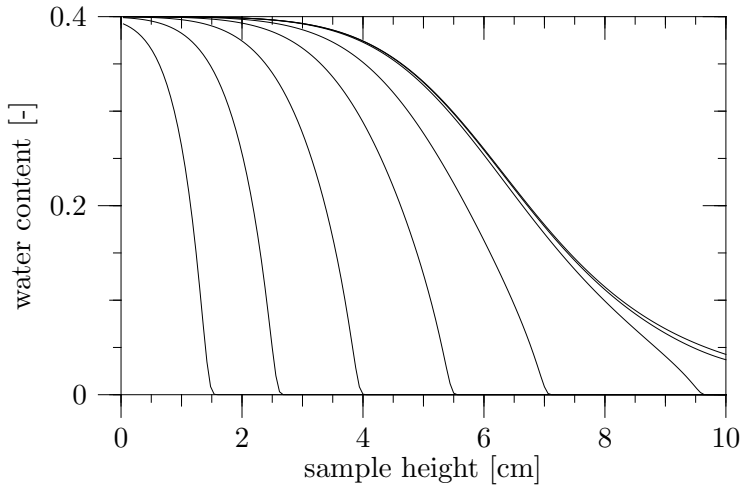

Figure 4.5: Simulated vertical water content profiles during imbibition in a dry sample at times $t = 0.008, 0.016, 0.033, 0.066, 0.13, 0.5, 1.0, 16.0$ h (from left to right)

experiment. The problem of entrapped air depends on properties of the pore space, the pore size distribution and the connectivity. To produce air entrapments water must flow fast through small pores to destroy the continuity in the air phase. Also cross-connections are needed to catch the air before it leaves the sample. Faybishenko (1995) shows experimentally that entrapped air has a large impact on the hydraulic conductivity. The samples he used were large undisturbed soil columns taken at some field site. He also divided the entrapped air in two parts, the "mobile air that discharges from the quasi-saturated soils" and "immobile air that disappears through dissolution". The quasi-saturated hydraulic conductivity is decreasing dramatically with the increase of the amount of entrapped air.
Considering the volume, occupied by the entrapped air, namely the large pores that have a major contribute to the total flux the hydraulic conductivity must drop if more pores become inaccessible for water.

4.3 Multi-step outflow and X-ray attenuation

In a multi-step outflow experiment effective hydraulic parameters were estimated by inverse modeling of the measured cumulative outflow data. The inverse model assumes the sample as homogeneous, but additional X-ray attenuation measurements during the outflow experiment showed a weak heterogeneity. The validity of the effective parameters has to be discussed with respect to the present heterogeneity.

4.3.1 Sample preparation

The used material was fine sand with a grain-size distribution in the range from 0.25 mm to 0.63 mm. The sample was prepared as described in sec. 4.1.1 by filling the material into a rising water table to minimize air entrapment and reach maximal water saturation. From the mass of the sand, its density and the volume of the sample the porosity was calculated to $\phi = 0.393 \pm 0.008$. Because of the filling process the saturated water content was assumed equal porosity, $\theta_s = \phi$. After saturating the sample a classical multi-step outflow experiment was performed. The sample was placed between the source and detector of the X-ray setup to record vertical X-ray attenuation profiles during the outflow experiment. The format of the experimental setup is shown in fig. 3.5 where the sample is mounted in a multi-step outflow support between source and detector of the X-ray system.

4.3.2 Measurement protocol

The initial boundary condition of the multi-step outflow measurement was complete saturation, i.e. the matric head at lower boundary was $h_{LB} = -\frac{\psi_m}{\rho_w g} = -10\,\text{cm}$ where ψ_m is the matric potential, ρ_w the mass density of water and g acceleration of gravity. Then, pressure at the lower boundary was decreased in three steps $h = -10 \rightarrow -5 \rightarrow -2 \rightarrow 0\,\text{cm}$ with duration of some minutes. Afterwards the pressure was changed in five steps of $\Delta h = 4\,\text{cm}$ to $h = 20\,\text{cm}$ (fig. 4.6). Time while pressure was constant between the steps ranges from 3 h to 40 h. The water outflow was caught in a burette and its amount calculated from the height of the water table in the burette and its geometry.
In fig. 4.6 the measured cumulative outflow and the boundary condition is shown. The time axis is split into two pieces: the first part shows the result for pressure $p \geq 0\,\text{cm}$ where nearly no outflow was observed, since the air-entry

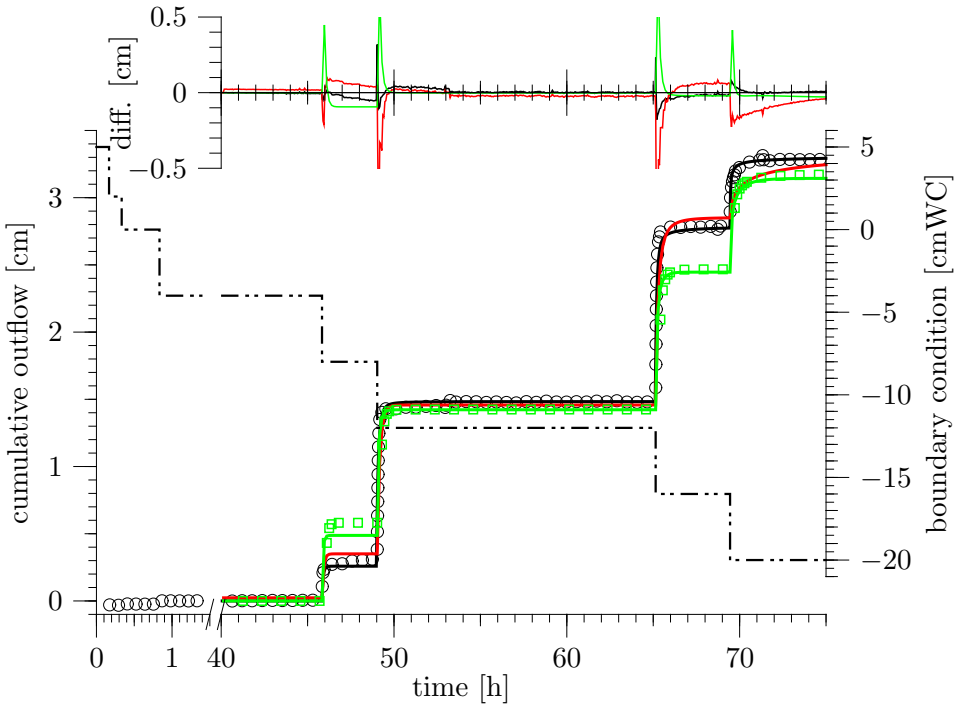

Figure 4.6: The circles show the measured cumulative outflow during the multi-step outflow experiment. The result of inverse modeling is shown as black line and the forward simulated outflow for the heterogeneous structure model is represented by the red line. The green squares show the simulated outflow based on the layered material model turned upside down and the result of inverse modeling these data is represented by the green line. Pressure at the lower boundary is plotted as dash-dot-dot line and related to the right y-axis. In the upper part the differences between point data and modeled and simulated line is shown in the corresponding colors.

pressure was not yet reached. This part was excluded from further evaluation. Outflow data was set to zero at $t = 40\,\mathrm{h}$ which was the starting point of inverse modeling.
After the pressure steps were established, X-ray attenuation profiles were recorded form the bottom to top of the sample with a spatial resolution of 0.4 mm, the pixel size of the detector. The time needed for one profile was $\approx 30\,\mathrm{s}$, but the system was at this time near hydrostatic equilibrium and the profiles are

not affected by internal changes of the sample.

4.3.3 Data processing

Vertical water content profiles were calculated from measured X-ray intensity data similar to sec. 2.5. The measured intensities $I(z,i)$ at position z and pixel i on the detector were corrected for their dark current. $I(z,i)$ was measured across the center of the cylindrical sample including 30 pixels on the detector line which corresponds to a width of 1.2 cm on the detector. In this range the path length of the beam through the material is nearly constant and the signal to noise ratio was improved by averaging.
The difference to the method described in sec. 2.5 was that no reference measurement for the dry sample exists, because the sample was build by filling sand in water and the column never was dry during experiment. However, the reference for the saturated sample was available. The difference between the attenuation $A_s(z)$ for the saturated sample and $A(z)$ for the unsaturated state is given by

$$\begin{aligned} A_s(z) - A(z) &= \ln \frac{I_0}{I_s(z)} - \ln \frac{I_0}{I(z)} \\ &= \ln \frac{I(z)}{I_s(z)} \\ &= (\theta_s - \theta(z))\mu_{water} d \end{aligned} \tag{4.2}$$

using the respective decomposition for attenuation into the fractions of attenuation of the present materials as shown in (2.64) and neglecting again the attenuation of air. The measured x-ray intensity profile for the saturated sample is denoted as $I_s(z)$ and the length of path as d. From (4.2) it is obvious that the measurement of I_0, the measured intensity without sample, is canceled and not needed. With the known attenuation coefficient for water $\mu_{water}(70\,\mathrm{keV}) = 0.0188\,\mathrm{mm}^{-1}$ the vertical water content profile results from

$$\theta(z) = \theta_s - \beta \frac{A(\theta_s(z)) - A(\theta(z))}{\mu_{water} d} \tag{4.3}$$

where θ_s is the saturated water content assumed equal to porosity. The unknown correction factor β accounts for effects due to non-linear attenuation. β was determined from measured cumulative water outflow during the experiment. For different pressure steps p_i the mean water content $\hat{\theta}(p_i)$ of the sample

can be obtained by

$$\hat{\theta}(p_i) = \theta_s - \frac{q(p_i)}{V} \quad , \tag{4.4}$$

where $q(p_i)$ is the measured volume of emanated water at pressure step p_i and V the volume of the sample. The amount of outflow between two pressure steps p_i and p_j can be calculated from (4.4) by

$$\Delta\hat{\theta}(p_i, p_j) = \theta_s - \frac{q(p_i) - q(p_j)}{V} \quad . \tag{4.5}$$

Obviously, this calculation is only valid for states of hydrostatic equilibrium at a given pressure step. Then, the relation

$$\hat{\theta}(p_i) = \int_0^{z_max} \theta(z, p_i) dz \tag{4.6}$$

should also be satisfied for $\hat{\theta}(p_{i+1}) - \hat{\theta}(p_i)$. With the measured X-ray attenuation profiles $\theta(z, p_i)$ can be calculated by (4.3) and β was chosen such that (4.6) was satisfied. This could be done for different pressure steps resulting in $\beta = 2.17 \pm 0.13$.

Differences between two steps were used because of the uncertainty in top of the water content profiles originated from changes in the top layer where the surface of the sample was lowered when pressure was applied at the bottom. For latter steps the matrix is stabilized and the difference between two following profiles is only affected by the outflow of water. The relative large value arises from the different fractions of sand, water and PVC to the measured attenuation. The contribution of attenuation of sand to the total attenuation is about four times larger than that of water with respect to porosity. This leads to apparent changes in water content that have their origin in non-linear attenuation of sand.

4.3.4 Results

From the measured outflow data hydraulic parameters were estimated using *eshpim* (sec. 2.6). The approach assumes the sample to be a homogeneous effective medium. The resulting, optimized parameters are shown in tab. 4.2, the related best-fit curve in fig. 4.6. The modeled outflow curve fits very well to the experimental result and uncertainties of the fitted parameters are small indicating that the values represent the hydraulic properties of the material in

Table 4.2: Column A contains best-fit values determined by inverse modeling of the measured outflow curve. Column B shows the results of fitting the simulated outflow data for the sample turned upside down. The parameters with empty boxes in col. B were set to the corresponding value in col. A and held constant. The sum of the squared differences between the original and fitted curve are shown in row SSQ. Uncertainties are calculated using the χ^2 statistics as described by Press *et al.* (1992).

parameter	A	B
K_s[cm/h]	84.9 ± 9.5	
n[−]	24.1 ± 1.2	6.31 ± 0.14
$\alpha[10^{-2}\,\mathrm{cm}^{-1}]$	5.73 ± 0.01	5.68 ± 0.03
θ_r	0.060 ± 0.001	0.0
θ_s	0.393 ± 0.008	
τ	0.5	
SSQ	0.68	1.66

an acceptable way.
With these values the vertical distribution of water within the sample was calculated for $h_{LB} = 8, 12, 16$ and 20 cm based on the van Genuchten parameterization with respect to pressure at the lower boundary and the sample height to compare it to the directly measured X-ray attenuation profiles. Measured and calculated profiles are shown in fig. 4.7
Obviously, the effective parameters estimated from outflow data cannot reflect the internal behavior of the sample. Especially the profile at $h_{LB} = 16$ cm shows large differences between prediction and measurement.
The top part of the sample is affected by small changes in the density of the material that lead to large changes in the measured attenuation because of the large attenuation coefficient for sand compared to that of water. If the volume in the top 2 cm of the sample becomes more compact because of lowering the sand surface for 1 mm the attenuation predicts a water content that is of 0.2 higher than reality.
The attenuation data clearly show that the structure is not homogeneous in the vertical direction, as if it was, the shape of different profiles should be similar which is actually not the case.

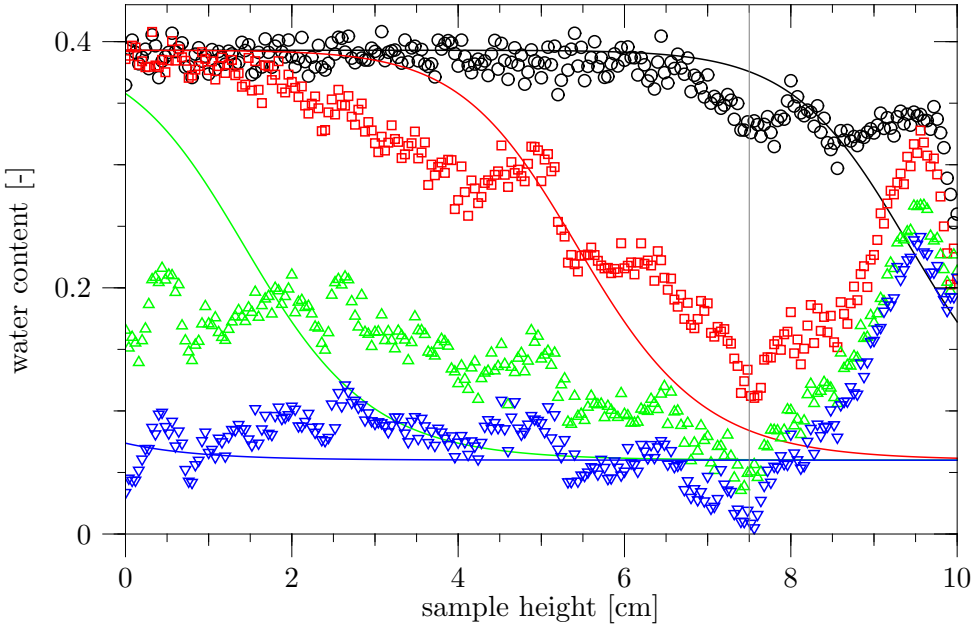

Figure 4.7: Measured (symbols) and simulated (solid lines) vertical water content profiles assuming a homogeneous sample. The matric head for the shown profiles at the lower boundary was $h_{LB} = 8\,\text{cm}$ (black), 12 cm (red), 16 cm (green) and 20 cm (blue). The hydraulic parameters were estimated by inverse modeling the multi-step outflow experiment. Values left of the vertical line at $z = 7.5\,\text{cm}$ are affected by changes in the sample surface that leads to unreal water content values.

To include heterogeneity a layered material model was generated based on X-ray attenuation data. Since attenuation profiles were measured in hydrostatic equilibrium it is possible to extract points on a water retention curve at different vertical positions of the sample. The matric head h [cmWC] for any point on the vertical z-axis is given by $h(z) = h(0) + z$, where $h(0)$ is the matric head at at lower boundary of the sample and z is the height above the lower boundary. Corresponding to the eight steps of the multi-step outflow experiment eight points on the water retention curve $\theta_z(h)$ were obtained. The discrete material model is based on points at $z = 0\,\text{cm}, \ldots, 7\,\text{cm}$ in steps of $\Delta z = 1\,\text{cm}$ and three additional ones at $z = 2.4\,\text{cm}, 4.3\,\text{cm}, 5.5\,\text{cm}$ to account for the structure in the measured profiles.

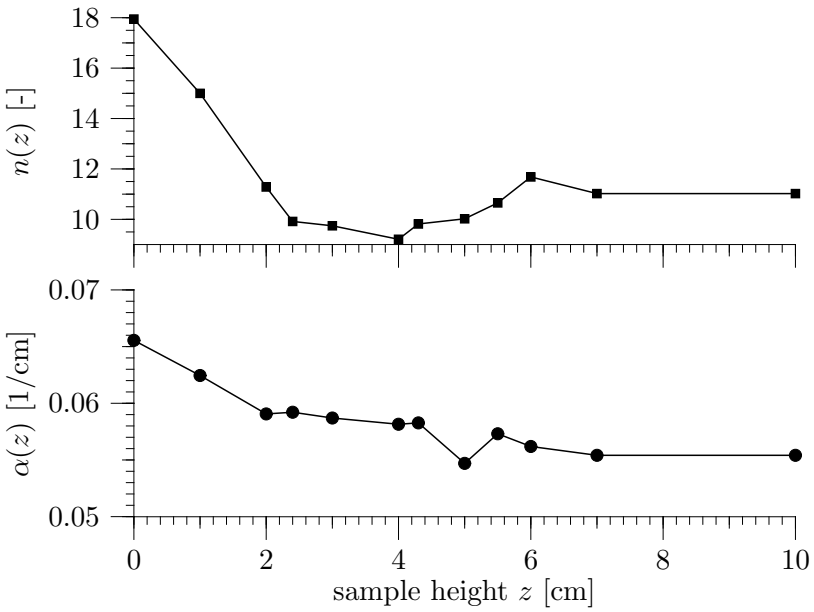

Figure 4.8: Vertical distribution of van Genuchten parameters $n(z)$ and $\alpha(z)$ assuming a layered material model.

A van Genuchten parameterization was fitted to the extracted points $\theta_z(h)$ to obtain a set of parameters $\alpha(z)$, $n(z)$ and $\theta_r(z)$ (fig. 4.8). Based on these parameters a layered material model was created. Values between the supporting points at different heights, were found by linear interpolation. The saturated hydraulic conductivity was set proportional to the square of $\alpha(z)/\alpha^*$ (in analogy to Miller media (Miller and Miller, 1956)) where α^* is the value found in the multi-step outflow data. The harmonic average of the hydraulic conductivities of each layer weighted by its relative thickness leads to an effective saturated hydraulic conductivity for the layered material model of 85.7 cm/h. This is very close to the value of the unstructured model (tab. 4.2). The values for saturated water content and turtosity where set to 0.393 and 0.5, respectively. With this structure a forward simulation leads to a much better match between measured and simulated water content profiles, as shown in fig. 4.9.
The main features of the profiles are reproduced very well and the measured outflow data is also modeled very well, except for the last pressure step (fig. 4.6). Here, the model underestimates the measured outflow as hydrostatic equilibrium is reached much slower than in the experiment. This is a consequence of the perfect layering of the modeled structure with the most coarse material at

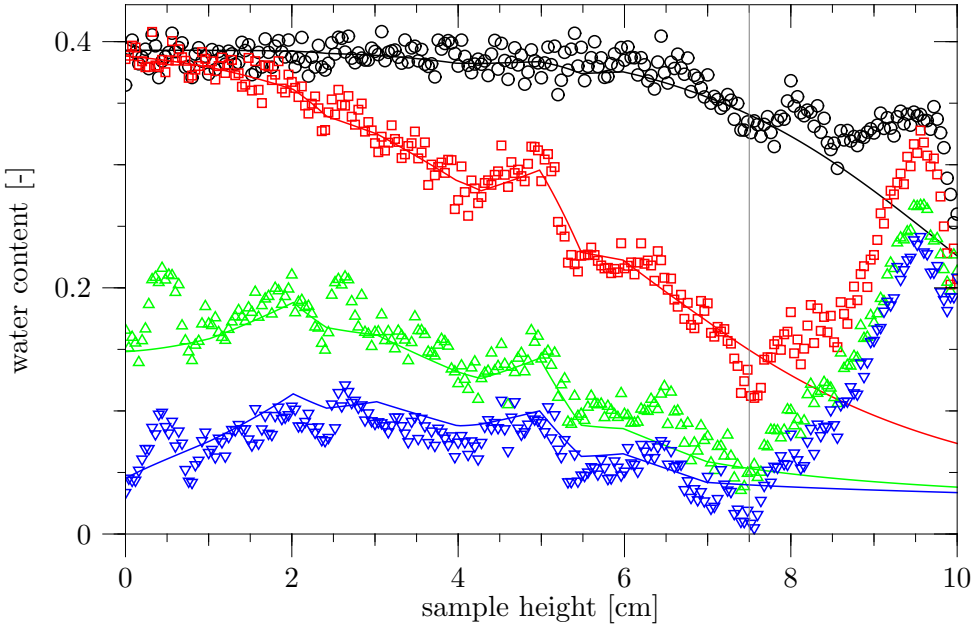

Figure 4.9: Measured (symbols) and simulated (solid lines) vertical water content profiles assuming a layered material model. The matric head for the shown profiles at the lower boundary was $h_{LB} = 8\,\text{cm}$ (black), 12 cm (red), 16 cm (green) and 20 cm (blue). Values left of the vertical line at $z = 7.5\,\text{cm}$ are affected by changes in the sample surface that leads to unreal water content values.

the bottom, reflected by the large parameter $\alpha(z)$ (fig. 4.8). With decreasing water content the conductivity of the lower layer is reduced first which hinders the water outflow from above. In reality, this layering is expected to be less perfect which would explain the discrepancy between model and experiment in the dry range.
Presumably, the layered structure of the sample was produced during sample preparation. When filling the sand into the rising water table the table was at $z \approx 1\,\text{cm}$ at the beginning. Then it was near or below the sand surface. This leads to increasing capillary forces during the filling process and thus to an increasing compactness of the sand. This is also depict in the parameter $\alpha(z)$ which decreases with sample height. The weak heterogeneity in this experiment was unintentionally created when preparing the sample. However, in natural soil, similar heterogeneities are omnipresent. Hence, the question arises: what

is the impact when a weakly layered heterogeneous sample is assumed to be homogeneous for the purpose of parameter estimation?

In this experiment the estimation of effective parameters assuming a homogeneous material model is not at all affected by the present heterogeneity since the inversion of Richards' equation yield an almost perfect description of the measured outflow data (fig. 4.6). This questions the significance and objectiveness of the estimated parameters which should not depend on details of the measurement procedure and on the specific flow regime.
If the parameters estimated by inverse modeling are objective, one would expect that the parameters found for one flow direction are able to describe the flow in the opposite direction, too.
For this horizontally layered material one would expect that its hydraulic behavior depends on the orientation of the sample. This is especially true for materials having a highly non-linear water retention curve with rapid changing water content along the vertical axis of the sample at hydrostatic equilibrium. In such a case the hydraulic behavior of different layers depend on their vertical position within the sample. Therefore the effective hydraulic parameters obtained from multi-step outflow experiments are expected to depend on the orientation of the sample. The $\theta(h)$ curve shown in fig. 4.10 indicates that this sample satisfies the assumption of rapid changes of $\theta(h)$ within the sample.

To test this experimentally the sample has to be turned upside down and the experiment has to be redone. With the setup used, this procedure is not possible, but can easily be done by simulating the multi-step outflow experiment assuming the reversed orientation of the sample. Fig. 4.6 shows the simulated outflow curve for the turned upside down sample, that is considerable different compared with the original data. In contrast to the original simulation, the coarse material in now on top of the sample leading to earlier drainage and the fine material at the bottom retain more water leading to less outflow at the end of the simulation.

The simulated outflow data for the turned sample was also fitted by inverse modeling assuming again a homogeneous material model. Fig. 4.6 shows the result and column B of tab. 4.2 contains the corresponding effective hydraulic parameters. The free parameters for inverse modeling were n, α and θ_r, the others were set to the values found before and held fixed. The resulting water retention curve and hydraulic conductivity for the sets of effective parameters are shown in fig. 4.10 and reflect the differences of the hydraulic descriptions.

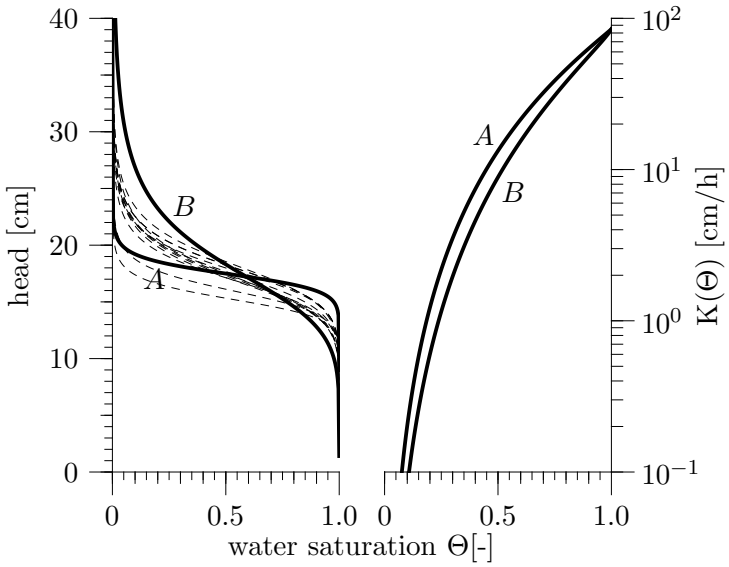

Figure 4.10: Water retention curve (left) and hydraulic conductivity (right) for the two sample orientations. Parameters of the respective curve A and B (solid lines) can be found in tab. 4.2. The dashed curves are calculated from the values $\alpha(z)$ and $n(z)$ shown in fig. 4.8.

4.3.5 Interpretation

The results show that there is no unique description of hydraulic properties since the parameters depend on the sample orientation. The satisfactory fit of inverse modeling is also no guarantee for the accuracy of the estimated values. The found effective hydraulic parameters using inverse modeling represent the outflow curve very well. A homogeneous material model was used to solve the inverse problem. But these parameters can not predict the internal behavior of the sample, observable in differences between the measured and simulated vertical water content distributions. These differences have their origin in a weak heterogeneity of the material produced during sample preparation. With the help of the X-ray attenuation the internal structure of the sample is indirectly observable through the water content profiles. This knowledge can be used to set up a heterogeneous layered material model, that represents the vertical water content profiles as well as the outflow curve.

Experiments like the one presented here are typically used to estimate hydraulic parameters used in simulations at the filed scale. The simulations are

based on structure models of the subsoil that is divided into several soil horizons that are found by geophysical methods like seismics, geomagnetics, electric resistivity or ground-penetrating radar. When these structures are localized they are assumed to be homogeneous and small samples of the size of some 0.1 m are extracted to determine hydraulic parameters with laboratory methods. The sample itself are assumed to be a representative elementary volume (REV), which means that the estimated parameters are valid for the large scale simulations.
The shown results can be discussed focusing on the REV behavior and on hysteresis. This will be done separately.

The assumption that the sample taken from some soil horizon is a REV is not fulfilled if the sample shows a layered structure itself. For a REV the size of the sample can be changed in a limited range resulting in the same estimated parameters. Also turning the sample is allowed. Both does not work here. Turning the sample leads to different parameters (tab. 4.2). With an increase or decrease of the sample in the vertical direction new layers are generated in the column or layers are removed. As shown in the simulation with the turned sample the difference in the outflow data can be addressed to the large α at low z-values (fig. 4.8). Thus, removing these layers will result in different outflow data, too. Also adding layers can change the outflow data and the estimated hydraulic parameters will change. Only increasing the radius of the sample will not change the estimated parameters while the discrete layers are homogeneous itself.
The next REV of the modeled structure will be found within the discrete layers, which have no underlying structure.
In natural soil this perfect layering may not be found. Then the question arises, is there a REV on any scale?
In comparison to the material model used in the simulation natural soils show structures on every scale. This must lead to the conclusion that there is no REV available. But the better question would be, is a REV necessary?
The found parameters can describe the outflow of water. If there are some other samples taken from the same soil horizon an estimation for the range of hydraulic parameters can be found and taken into account during simulations at the field scale.

If the flow direction is not changing it could be enough to determine the range of parameters for every soil horizon. In the topsoil the flow direction is changing often because of rainfall, root uptake and evaporation, where the last

two force the flow towards the soil surface. From the layered structure model a different set of effective hydraulic parameters was determined (tab. 4.2). The hysteresis of $\theta(h)$ and $\mathsf{K}(h)$, the difference for wetting and drying, is well known (Haines, 1930; Kool and Parker, 1987; Jaynes, 1992) and for $\theta(h)$ described by advanced models of e.g. Parlange (1976),Mualem (1984), where all scanning curves on $\theta(h)$ are predicted from on branch of the curve. The hysteresis in $\mathsf{K}(\Theta)$ are suggested to be small enough to ignore it (Topp, 1971; Gillham *et al.*, 1976). Modeling drainage and imbibition in the unsaturated zone needs to solve Richards' equation including a model that accounts for hysteresis. The present solvers assume that the drying and wetting curve are of the same shape, e.g. Si and Kachanoski (2000) using a parameters α_d for drainage and α_w for the wetting part.
The Mualem/van Genuchten parameterization of $\mathsf{K}(\Theta)$ (2.21) depends on the parameter n but not an α. If the hysteresis of $\mathsf{K}(\Theta)$ is neglected n is constant for wetting and drying. This implies that the hysteresis of $\theta(h)$ is determined by α which is not included in $\mathsf{K}(\Theta)$. Therefore the shape of the $\theta(h)$ curves for wetting and drying is similar.
The "hysteresis" arising from the layered structure does not fit into that scheme. The effective parameters for the two flow directions show similar parameters for α and remarkable differences for n.
Topp and Miller (1966) used two kinds of materials to measure $\mathsf{K}(\Theta)$, uniform glass spheres and glass beats, lightly sintered into aggregates. The samples were homogeneous and the hysteresis of $\mathsf{K}(\Theta)$ was found to be negligible. From fig. 4.10 it is obvious that there is a non-negligible difference in $\mathsf{K}(\Theta)$ for the two flow directions.

To check the objectivity of parameters estimated from multi-step outflow data it could be useful to perform the experiment for two sample orientations, if possible. This data can be used in numerical simulations to assess the uncertainty of the results.

4.4 Other applications of the X-ray system

The X-ray setup was also used for some other applications, e.g. the calibration of a light transmission method used to study changes of the water content inside a Hele-Shaw cell. Another possible application of the setup is the support of multi-step outflow experiments by checking the rough structure of the sample in reconstructed tomographic images.

4.4.1 Calibration of light transmission measurements with a Hele-Shaw cell

Studying the water distribution in a Hele-Shaw cell with light transmission methods needs the calibration of the transmission to the water content in the cell. Therefore X-ray attenuation was used to measure the water distribution within the cell. The saturation was calculated from these data and compared to the intensity data of the light transmission recorded with a digital camera. The cell used, consists of two glass plates of 6 mm thickness and 30 cm width and height mounted vis-à-vis with 3 mm spacing between. At the bottom of the cell an inlet was installed to bring the sand in contact with a water table and control the height of the water table. Sand was filled in the gap between the two glass plates and the cell was placed between tube and detector with the glass plates perpendicular to the center ray. Then a vertical scan of the dry material was made as reference. After this a water table in the cell was established at several heights and X-ray attenuation profiles were recorded again. At the end the water table was adjusted to the top end of the cell and kept there for some hours until maximal saturation was reached. The stepwise saturation was done to minimize air entrapments. At complete saturation a second reference image was taken. After saturating the cell, water table was decreased again in several steps and data recorded. Additionally at all states the transmission of light was recorded with the digital camera that should be calibrated. This light intensities were normalized with the two reference measurements by

$$I_{LTM} = \frac{I - I_{dry}}{I_{sat} - I_{dry}} \quad ,$$

where I_{dry}, I_{sat} and I are the transmitted intensities for the dry, saturated and partial saturated sand, respectively.
Together with the two reference measurements the spatial distribution of water saturation $S(x, z)$ was calculated from measured X-ray data, in analogy to

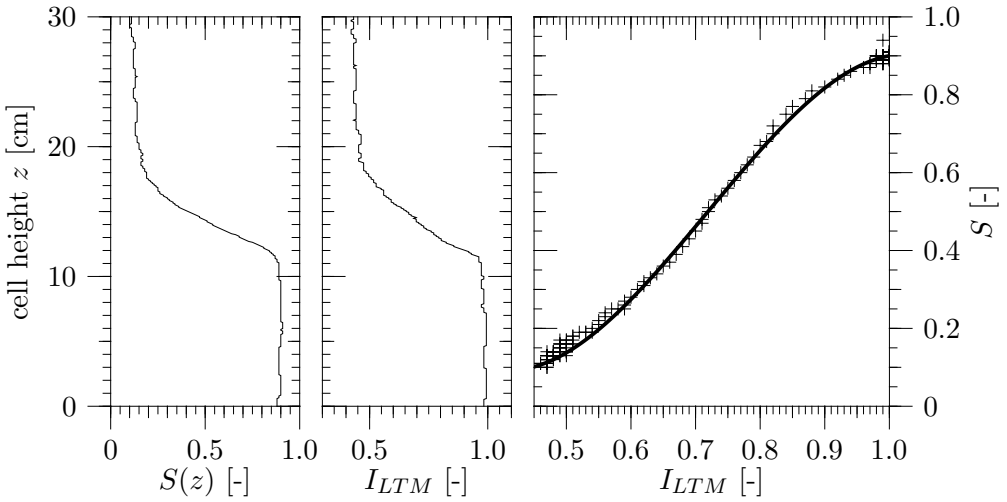

Figure 4.11: Water saturation S in a Hele-Shaw cell obtained from X-ray profiles and light transmission (I_{LTM}) in the left two graphs. The right graph shows the correlation between the two methods (symbols) and the fitted third-degree polynomial (line). *Transmission data courtesy F. Rezanezhad.*

(2.65), by

$$S(x,z) = \frac{A(x,z) - A_{dry}(x,z)}{A_{sat}(x,z) - A_{dry}(x,z)} \tag{4.7}$$

with

$$A_\xi = ln\left(\frac{I_0(x)}{I_\xi(x,z)}\right)$$

where A_ξ is the measured attenuation calculated from the measured X-ray intensities. The subscript ξ denotes the different saturation states *dry*, *sat* and between. The coordinate system is oriented with the x-axis parallel to the detector and the z-axis vertically, starting at the bottom of the cell. I_0 was taken at a position where no sample was between tube and detector, all intensities were corrected for their dark current. To increase the signal to noise ratio the vertical homogeneity was improved and $S(z) = \sum_{x=0}^{n_x-1} S(x,z)$ was calculated by averaging the all n_x values in x direction.
The resulting $S(z)$ curve is shown in the left graph of fig. 4.11. The middle

graph shows the averaged light intensities recorded with the digital camera. The water table in the shown situation was near the bottom of the cell, while drainage of the previous fully saturated cell. In the right part of fig. 4.11 the resulting correlation between saturation measured by X-ray attenuation and the intensities of the light transmission experiment is shown. The calibration for light transmission was found by fitting a third-degree polynomial to the data and results in

$$S = 1.7 - 9.0\ I_{LTM} + 15.3\ I_{LTM}^2 - 7.1\ I_{LTM}^3$$

with a correlation coefficient of $R^2 = 0.999$ (Rezanezhad, 2004).
The combination of X-ray attenuation opens the possibility to calibrate light transmission images taken with a digital camera to absolute values of water saturation that can be used for further experiments. One disadvantage is that the calibration hold only for exactly the material used. Other materials with different transmission properties have to be measured again with the procedure described above, due to digital imaging.

4.4.2 Structure analysis of natural soil columns

Hydraulic modeling at a field scale normally needs information about the hydraulic properties of the underlying materials. Typically small undisturbed samples are taken from the main structures and standard experiments are performed in laboratory to determine the needed hydraulic parameters. In best case these parameters are obtained from representative samples. But from the resulting parameters and the samples surface it is not possible to judge if the sample is representative or not (sec. 4.3). Together with X-ray attenuation and tomography methods it is possible to explore the internal structure without destroying the sample.

The setup of X-ray tube and detector shown here allows tomographic studies by rotating the sample between both. Transmitted X-ray intensity data can be used to reconstruct the internal distribution of the attenuation coefficient as shown in chapter 2.4.

An undisturbed soil column taken at a test side near Heidelberg was used to determine effective hydraulic parameters that should be used in further simulations on the scale of the test side. The sample was 10 cm high and 16.3 cm in diameter. The material was loamy sand located in a depth of 45-55 cm below the surface. Effective hydraulic parameters for this sample were determined by

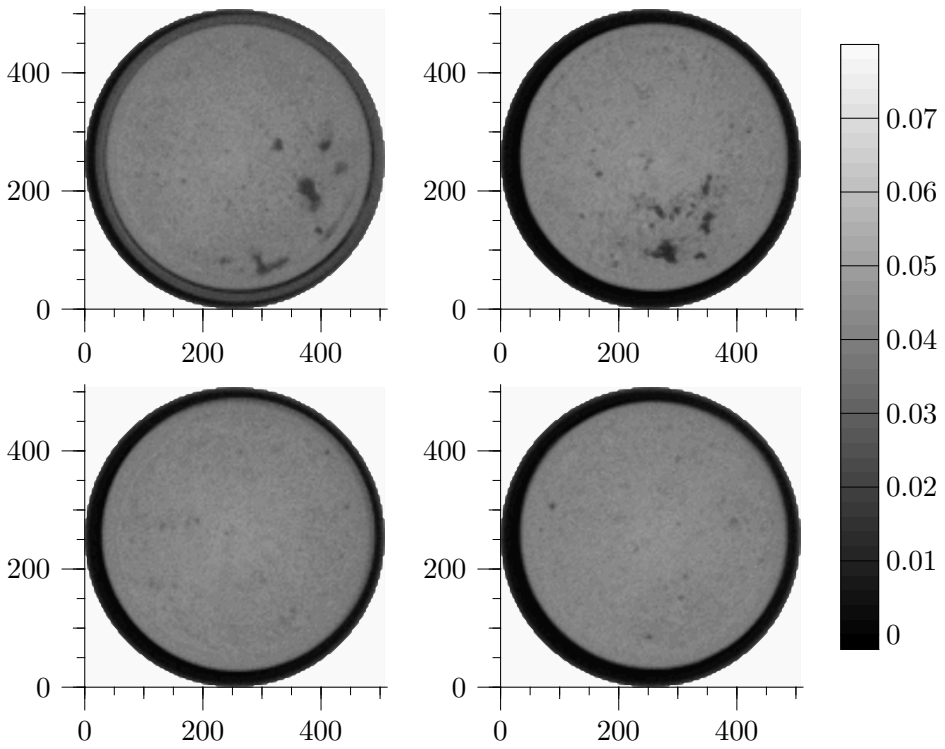

Figure 4.12: Slices through an undisturbed soil column at height 0.13, 1.93, 5.63 and 9.13 cm (from upper left to lower right) below the sample surface. The grey values in the slices are related to the X-ray attenuation coefficient at 70 keV in units of 1/mm. The x- and y-axis shown are pixel numbers of the 512×512 pixels large reconstruction grid. The spatial resolution is 0.4 mm/pixel.

a multi-step outflow experiment. Afterwards it was water saturated and sealed at bottom and top to prevent water runoff. In several heights of the sample data was recorded during sample rotation. From these data slices were reconstructed using the iterative reconstruction method described in section 2.4.5. Figure 4.12 shows some example images at different positions of the sample. All in all slices at 45 different heights were recorded. In these images large holes within a relative homogeneous matrix were observed. From reconstructed data the averaged attenuation coefficient was calculated by averaging the values that belong to the soil excluding the PVC tube that surrounds the soil. To obtain information about the surrounding of the holes the large ones were marked

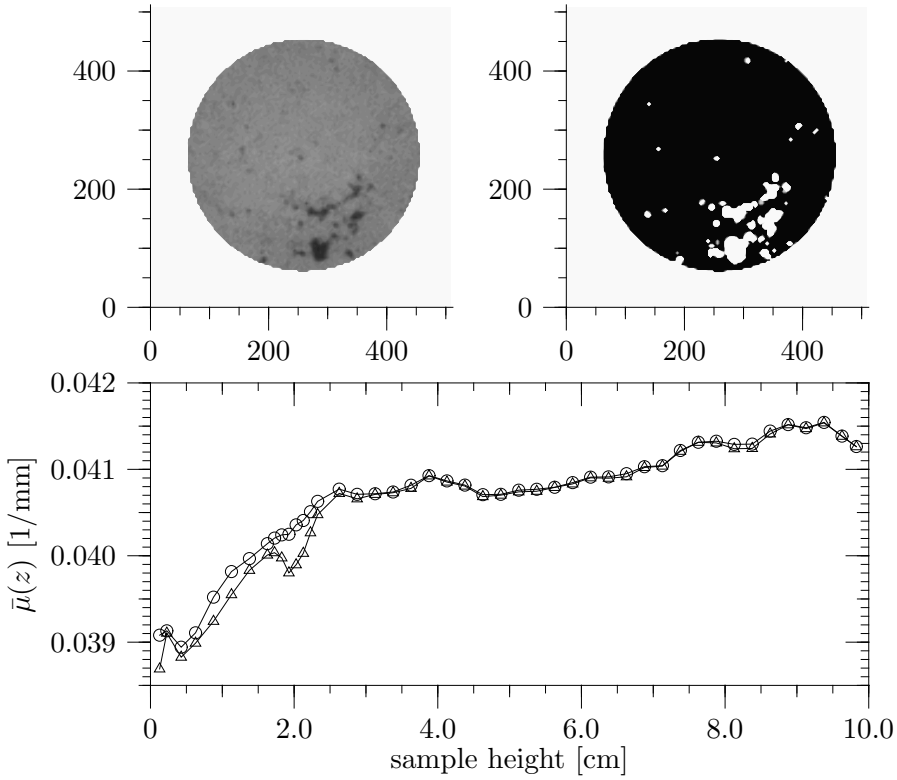

Figure 4.13: Averaged attenuation coefficient $\bar{\mu}(z)$ calculated from reconstructed slices. Triangles represent the $\bar{\mu}(z)$ for the whole sample and the circles are the averages excluding large holes. On the top left an example slice at 2.03 cm height is shown and on the right the excluded areas of the holes are highlighted in white.

by image analysis as depict in the upper part of fig. 4.13. Then a second profile of averaged attenuation coefficient was calculated excluding the hole area from averaging. The resulting profiles $\bar{\mu}(z)$ are shown in the lower part of fig. 4.13. Obviously, there are more holes at the bottom of the sample than at the top, because of larger difference between the two profiles at the bottom. The small difference near 8 cm sample height is caused by the hole produced by a tensiometer located here before. While the holes are excluded from averaging there is still a change in the attenuation coefficient observable (fig. 4.13). Assuming that the surrounding material is always the same, similar to SiO_2, it is possible to calculate the change in porosity $\Delta\phi$ from the maximum

and minimum $\bar{\mu}(z)$ values by

$$\begin{aligned}\Delta\phi &= -\frac{\Delta\bar{\mu}}{\mu_{SiO_2}(70\,\mathrm{keV})} \\ &= -\frac{\bar{\mu}(0.5\,\mathrm{cm}) - \bar{\mu}(9.4\,\mathrm{cm})}{\mu_{SiO_2}(70\,\mathrm{keV})} \\ &= -\frac{0.0390\,\mathrm{mm}^{-1} - 0.0415\,\mathrm{mm}^{-1}}{0.0557\,\mathrm{mm}^{-1}} \\ &= 0.045 \quad .\end{aligned}$$

This means that porosity is decreasing from bottom to top. In sec. 4.3 it was demonstrated that effective parameters determined from samples affected with weak internal heterogeneities must be interpreted carefully.
To increase the accuracy of the determined hydraulic parameters it may be helpful to redo the multi-step outflow measurement with samples from the same soil to average the results and decrease the errors by increasing the number of measurements.
Another solution could be a change of the structure model in the inverse modeling procedure from an assumed as homogeneous to a more realistic one using the information of the X-ray measurements. This needs inverse modeling techniques that can handle three dimensional structure models. The price to pay here is an increase in computing time, but multiple experiments are also time consuming.

4.4.3 Water distribution in an artificially structured medium during infiltration

As shown before the setup cannot be used to monitor hydraulic processes with high spatial and temporal resolution together, when the internal changes are much faster than the regeneration time of the X-ray tube. A slow process where this should be possible is the infiltration into a dry sample shown next.

The used sample was build from sand with different grain size distributions. Coarse sand with grain size between 0.63 mm and 1.25 mm and fine sand with grain size below 0.25 mm was used to build an artificially structured sample. A rotationally symmetric structure was build particularly with regard to save computing time in further simulations. The axis of symmetry was located in the center of the surrounding PVC tube. The radius was 8.15 mm and the height of the sand was 7.0 cm. In fig. 4.14 a sketch of the structure is shown.

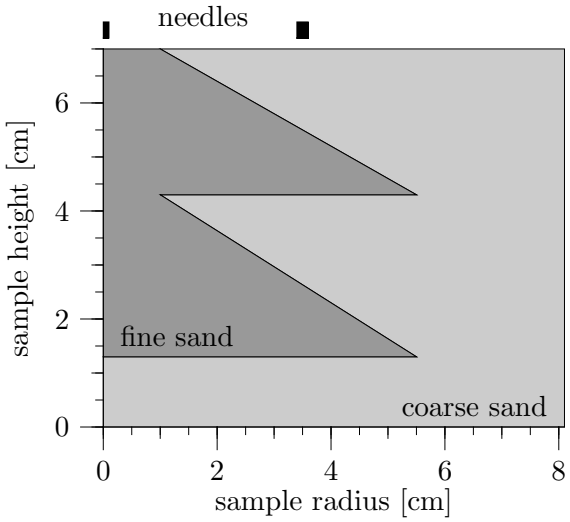

Figure 4.14: Sketch of the radial symmetric structure build from coarse and fine sand. The symmetry axis of rotation is on the same as y-axis on the right border. On top, the positions of the needles is indicated one in center and the others distrubuted equidistantly on a circle with radius 3.5 cm.

The structure was produced in several steps. Fist, the lower homogeneous part of coarse sand was filled into the column. Afterwards, a cone was poured into the center until the circle at the bottom reached a given radius of 5.5 cm. This radius was fixed with a tube of thin paper. Then the remaining volume inside the paper tube around the cone was filled with coarse material, up to a fixed height of 3.0 cm above the homogeneous part at the bottom of the sample. Next, the space between paper and PVC was also filled with coarse sand and the paper tube was carefully removed. Then, a second cone of the same size as the first was poured, with the same steps as before, on top of the first cone. The tip of the second cone was removed to increase the area of fine sand at the top. On top of the sample a sprinkler was mounted with one needle in the center, directly above the fine sand, and six additional needles distributed equidistantly on a circle with radius 3.5 cm around the center. The drops falling from the outer needles did not hit the fine sand.

When sample preparation was finished X-ray measurements of the dry sample were made as references, one vertical scan and tomographic images at different positions. The infiltration was controlled with a peristaltic pump operated

at a constant flux rate of 1.1 cm/h. At this flux the hydraulic conductivity of the fine sand is larger than that of the coarse and the flow is forced through the initially dry structure of fine sand. After infiltration started at time $t = 0\,\mathrm{s}$ the distribution of water within the sample was monitored during infiltration by vertical X-ray attenuation profiles and tomographic images at special heights of the column.
Vertical distributions of water were estimated from attenuation data where the X-ray beam passes the center of the sample. Subtracting the attenuation profile

$$A_d(z) = (1 - \phi)\mu_{sand}d + O$$

of the dry profile from the others

$$A_i(z) = (1 - \phi)\mu_{sand}d + \theta^*(z)\mu_{water}d + O$$

leads to

$$A_i(z) - A_d(z) = \theta^*(z)\mu_{water}d \tag{4.8}$$

where μ_{sand} is the attenuation coefficient of sand, ϕ is the porosity and d the thickness of the sample. O represents the other contributions as the attenuation of air and the surrounding PVC tube. With the known attenuation coefficient of water and the thickness of the sample $d = 163\,\mathrm{mm}$ vertical water distributions $\theta^*(z)$ can be calculated from (4.8) shown in fig. 4.15.
Note, the profiles $\theta^*(z)$ do not represent the volumetric water content. Only if the sample is homogeneous in each depth the measured data is related to the volumetric water content. Here, the measured attenuation results also from integration along a line equal to the diameter of the sample. Thus, obtained data is not sensitive for the radial heterogeneity due to the internal structure. The measured attenuation $A_i(z)$ is the integrated value along the path of the beam through the center of the sample

$$A_i(z) = \int_{-r}^{r} \mu(r', z)dr' \tag{4.9}$$

where r is the radial coordinate with its origin in the center of the sample. With increasing $|r|$ the values $\mu(r, z)$ represent an increasing fraction of the total sample. The integrated measurements of attenuation contain no information about these changing contributions. Thus, the attenuation $A_i(z)$ reflects

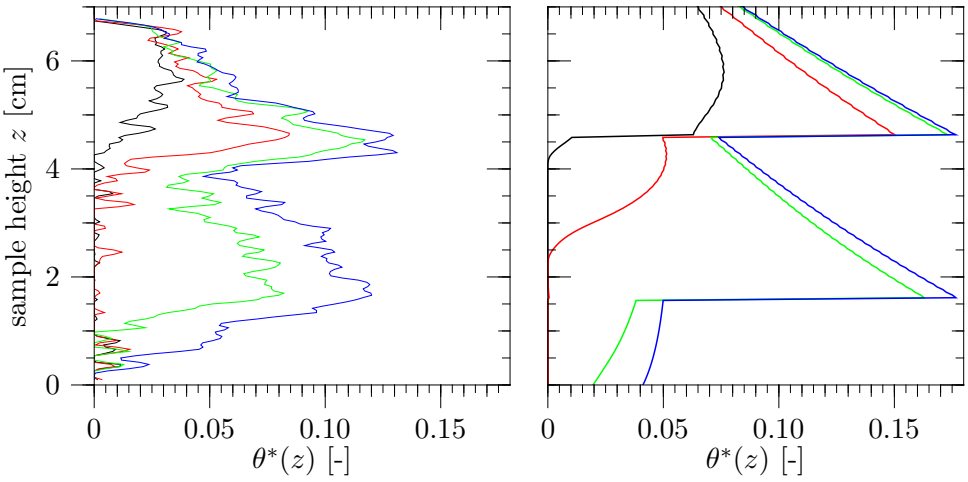

Figure 4.15: Measured (left) and simulated (right) vertical distribution of water during infiltration into the primary dry material shown at times $t = 340\,\mathrm{s}$ (black), $t = 645\,\mathrm{s}$ (red), $t = 1511\,\mathrm{s}$ (green) and $t = 2310\,\mathrm{s}$ (blue).

the vertical distribution of water and not the volumetric water content. This behavior is denoted by the usage of $\theta^*(z)$ instead of $\theta(z)$.

From reconstructed slices the water content along one line through the center was determined and compared to the corresponding point in the measured vertical profile. This was done later in the experiment where a stable and constant flow regime was established. Then the time between the vertical scan and recording tomographic data is negligible. There was no appreciable discrepancy found between the values determined from reconstructed slices, where beam hardening is corrected, and data on the profile. From this comparison effects like beam hardening could be ruled out and the calculated profiles represent $\theta^*(z)$.
Simulations with $\mu\varphi$ (sec. 2.6) of this infiltration process based on the structure model shown in fig. 4.14 were made. The hydraulic parameters of the two involved materials were found in separate multi-step outflow experiments. Simulated distribution of water at $t = 943\,\mathrm{s}$ and $t = 2535\,\mathrm{s}$ are depict in fig. 4.16. The shown water distributions represent exactly the values explored by the X-ray beam and the corresponding vertical profiles can be calculated by simple averaging the modeled water content along horizontal lines. Resulting vertical

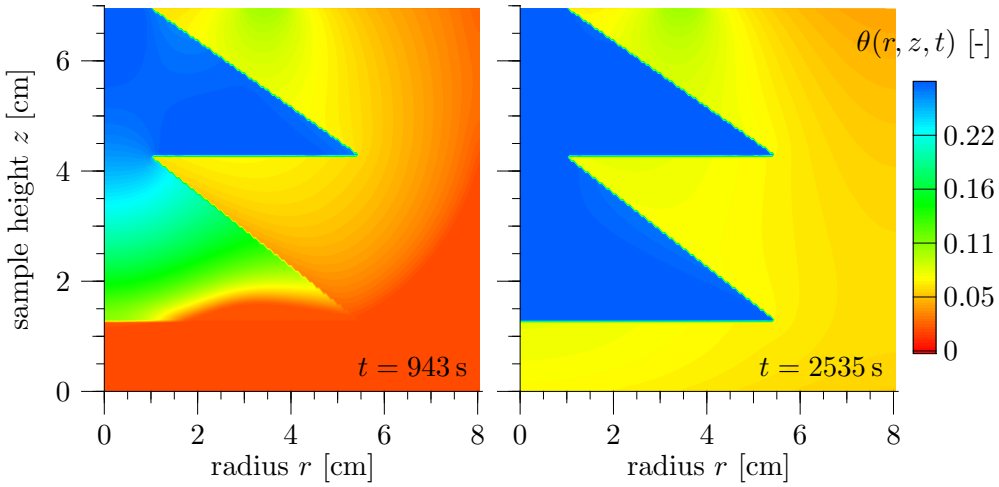

Figure 4.16: Water content distribution $\theta(r, z, t)$ during infiltration into a primary dry sample at time $t = 943$ and $t = 2535$.

distributions of water calculated at the same times as the measured profiles were shown in fig. 4.15.
To extract the distribution of water from tomographic images, they were filtered by a Gaussian filter with a circular filter window with a radius of 6 pixel ($\sigma = 1$ pixel, sensitivity 3σ) to reduce noise. Then differences between the wet and the corresponding dry image were calculated and filtered again using a larger filter window with a radius of 9 pixel ($\sigma = 3$ pixel, sensitivity 3σ). All pixel values were divided by the attenuation coefficient of water ($\mu_{water} = 0.019\,\mathrm{mm}^{-1}$) to achieve the volumetric water content values for each pixel. In fig 4.17 water content distributions at different times are depict. Shown are images at two positions, pos. 1 at the lower end of the upper cone and pos. 2 is 1 mm below.

The shape of the vertical distribution of water is well reproduced by the simulation (fig. 4.15). At the bottom of the sample was a dry porous plate and water drains free from the lower end of this plate. When water reaches the lower end of the sample it retains and further recorded profiles must differ from simulation because free drainage was not implemented as boundary condition for the simulation. Therefore only the profiles where the sample was still dry at the bottom are shown. The sharp edges at the two lower ends of the two cones in the simulation compared to the measurements show that in

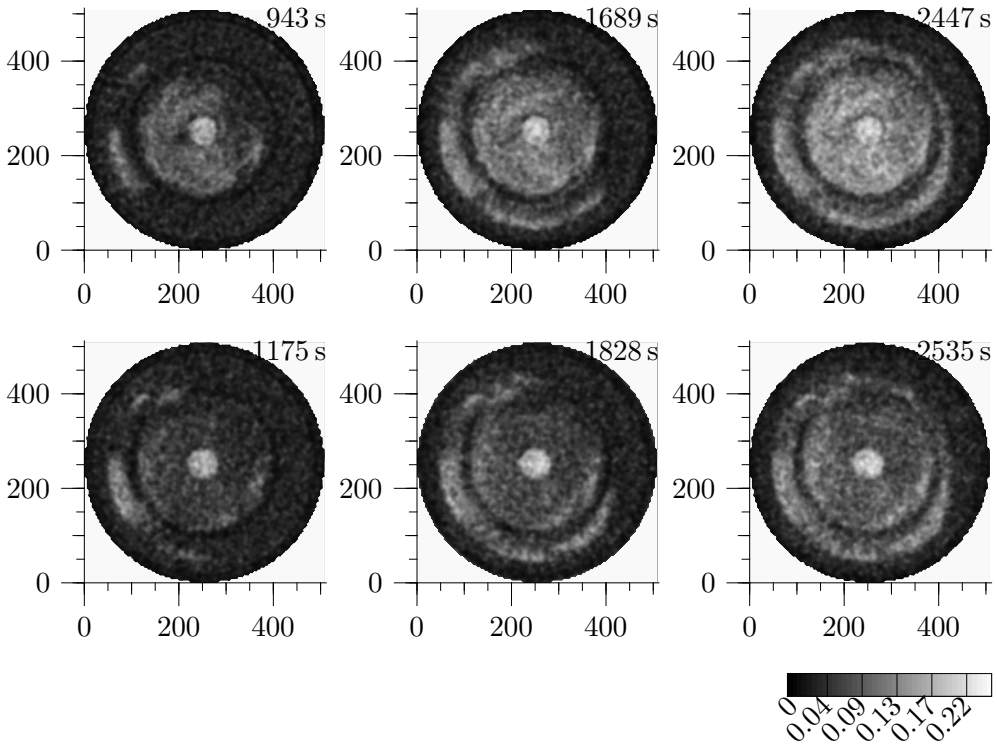

Figure 4.17: Reconstructed slices at different times during water infiltration into the primary dry sample. The upper row shows images at the lower end of the upper cone (pos. 1). Images in the lower row were taken 1 mm below (pos. 2). All images show the differences between wet and the respective dry image, with volumetric water content coded in different grey levels. x- and y-axis represent pixel numbers of the 512×512 pixel large reconstruction matrix. The spatial resolution is 0.4 mm/pixel.

the structured sample the boundary layer between the two sands is less sharp due to poor sample preparation and mixing or de-mixing of the material. The shown simulation in fig. 4.16 is the result at time $t = 943\,\mathrm{s}$ the same time like the upper left slice in fig 4.17. In the slice a small amount of water is located at the outside of the fine sand. This behavior is also observed in the other images. In the simulation the main part of water is funneled through the fine sand and the water content of the coarse sand is always below 0.07, much lower than in

the slice data.
This could be an explanation for the discrepancy between the values of the measured and simulated profiles where measured values are lower than simulated. The total amount of infiltrated water is the same in experiment and simulation, but the simulation did not reproduce the water flowing around the fine sand in that amount as it was found in tomographic data. This means that the total amount of water found in the measured profiles must be lower than in the simulation. The water in the coarse sand has its origin in small structures produced during sample preparation. The dark ring of low water contents, that surrounds the fine sand in the reconstructed images, is at the same position as the paper tube was during sample preparation. The low water content at this position can be explained by incomplete mixing when the paper tube is removed resulting in a coarser structure than around. The lowered hydraulic conductivity produces a barrier for the water flux breaking the forced flux through the fine material. The main flux funneled through the fine sand predicted by the simulation, is found in the experiment, indicated by the high water content in the center of the reconstructed images.

This shows that also in artifical structures the building process should be checked after preparation. Small anomalies, even in carefully prepared samples, have a large impact on the hydraulic behavior. The infiltration process can be monitored during the experiment with the usage of X-ray attenuation techniques and reveal the internal hydraulic behavior. Also the effect of small heterogeneities in the artificial structure, not included in the simulation, can be shown.

5 Summary and conclusions

An alternative method to measure the water-retention curve was presented. A low pressure was applied to the lower boundary of a homogeneous sand sample. In hydrostatic equilibrium a vertical X-ray attenuation profile was recorded. Together with two reference profiles of the dry and completely water saturated sample the vertical water content profile $\theta(z)$ was calculated. In hydrostatic equilibrium the z-axis can be transformed into a matric head h-axis. This results in a section of the water-retention curve $\theta(h)$ that can be fitted by a van Genuchten parameterization to determine the parameters α and n. The parameters were also estimated by inverse modeling of multi-step outflow data. The comparison of the two sets of parameters shows that the method can be used to estimate the van Genuchten parameters with reasonable accuracy.
In the presented example the material offers a water-retention curve within the 10 cm sample height that shows a large enough range of saturation to estimate parameters. If saturation changes less in the accessible range, an extension is possible, by changing the lower boundary condition. The water-retention curve can be shifted through the sample and the single pieces must be merged until the entire curve is observed. It is also possible to use samples that are longer than 10 cm and measure the curve at once. With the system used, it is possible to measure vertical attenuation profiles with a height up to 120 cm.
One problem noted during the experiment was the accuracy of the parameter α which is directly related to the accuracy of the pressure at the lower boundary. At the time, the experiment was done, there was no possibility to control the pressure near the X-ray setup. The sample was desaturated separately. Then the pressure at lower boundary was fixed and the sample was transfered to the X-ray attenuation setup. To increase the accuracy of the parameters it would be much better to control the boundary condition while the sample is located at the X-ray system, to prevent changes in the sample caused by the sample transport.

During the development of other experiments a complete multi-step outflow setup was included into the X-ray setup, which allows to control the pressure at the lower boundary of the sample and to monitor the cumulative outflow of

water. It was used to perform multi-step outflow experiments and visualize the internal behavior of the sample in vertical attenuation profiles and tomographic images.
An unintentionally created heterogeneity during sample preparation was found when the prediction of vertical water content profiles were compared to measured profiles. The prediction was done considering van Genuchten parameters obtained by inverse modeling measured outflow data assuming a homogeneous sample. The difference between simulation and measurement can be explained by a weakly layering of the sample. A layered material model was created from the attenuation data and the formerly constant van Genuchten parameters α and n depend on the vertical position of the sample.
A forward simulation of the outflow experiments using the package $\mu\varphi$ (sec. 2.6) represents the vertical water content profiles much better than the constant parameters. The outflow data is represented satisfactory, too. Thus, the important effective parameters α and n are no longer objective. Obviously, a layered sample is sensitive to the flow directions except it is symmetric for these directions. The example presented in this work was not symmetric and turning the sample upside down in the simulation leads to a different outflow curve as the measured. The experimental setup does not allow this turning. Inverse modeling of the forward simulated outflow data results in different hydraulic functions.
This demonstrates that weakly layering prevents effective parameters from being objective. The heterogeneity here was produced unintentionally, but in natural soil heterogeneity is omnipresent. Even the layering as found in the used artifical sample must be found in natural soil considering the formation processes of soil. Sedimentation and increasing pressure with increasing depth force the development of such structures. Effective parameters estimated from special samples taken at the field have to be carefully used in simulations. Especially the soil layers near the ground surface are affected by this behavior. Here the direction of flow changes from downward to upward depending on precipitation, root uptake and evaporation. One possibility to decrease the uncertainty of the parameters and to check if layering is present could be a re-design of the multi-step outflow experiment to allow measurements in both flow directions. Alternatively two samples taken very close to each other, can be used, mounting one upside down with the present setup. The differences between the two flow directions are typically ascribed to the hysteresis of the water-retention curve. The results here show that this might not be the only reason for these differences.

Rapid changes of the water content were studied during imbibition of water into an initially dry sample. To increase the temporal resolution of the setup the detector was mounted vertically. This opens the possibility to record attenuation profiles along a vertical transection through the sample with a temporal resolution down to the minimal exposure time of the detector in the range of 25 ms. With this setup the water content profiles within a homogeneous sample were monitored from the point where the dry sample was connected to a water table at the bottom. Differences were found comparing the measurements to results of forward simulations of the problem. The imbibition shows two processes. At the beginning the water content at the bottom is increasing rapidly and after half an hour this increase slows down. The bottom of the sample becomes not completely saturated after 16 hours. The forward simulation that solves Richards' equation assumes the air to be continuous at all points in time and space. Therefore the simulation shows full saturation at the bottom from the beginning. From the experimental results it can be concluded that the water at the beginning rapidly enters the sample and destroys the continuity of the air phase at some points. Entrapped air can leave the sample by producing bubbles when the pressure in the air phase becomes large. Some air even stays in the sample as residual air phase and can only disappear as dissolved air through the water phase.

In several experiments the usage of tomographic images as support for hydraulic experiments was demonstrated. During infiltration of water in dry structured sand the evolution of the water content at selected positions was monitored with tomographic images. They can be used to check the quality of artifical structures after sample preparation. They also can be used to verify the calibration from X-ray attenuation data to water content. The image reconstruction accounts for beam-hardening effects due to non-linear attenuation and results with the distribution $\mu(x, y)$ of the attenuation coefficient for an arbitrary photon energy. From these data absolute water contents can be calculated if the porosity $\phi(x, y)$ is known or a reference image exits where the sample is in a well defined state (dry or fully water saturated).
The structured sample here was build from fine and coarse sand whereas the fine sand was arranged as two cones on top of each other embedded in the coarse sand. On top of the sample a sprinkler was used to apply a constant water flux. The infiltration process was monitored as X-ray attenuation profiles, and tomographic images were recorded. Measured data was again compared to simulated. The temporal evolution of the shape of the vertical profiles was well reproduced by the simulation. The absolute values were overestimated by

the simulation at all points. The difference can be addressed to water which was found in the tomographic data at places where it was not predicted. The simulation predicts that the water flux is forced to the fine material that has a higher hydraulic conductivity at the beginning. In the experiment more water was found in the surrounding coarse material than predicted by the simulation. This water was not observable in the vertical profiles and therefore the measured values must be smaller than the simulated. Again the sample preparation is liable for the water in the coarse sand. The support used to prevent mixing between fine and coarse sand produced new structures itself. This position can be found in the tomographic images indicated by low water content. This can be explained by some de-mixing or incomplete mixing of the coarse sand at these locations. In dry state the hydraulic conductivity of sand is lower the coarser the material is. This means that in the sample a hydraulic barrier was produced which understates the forcing of flow through the fine sand.

Tomographic data can also be used to test undisturbed natural samples if they are homogeneous and estimated effective parameters are objective in that way that they represent the hydraulic behavior of the sample. In a series of tomographic images from an undisturbed sample a change in density was found together with large holes. Excluding the holes from the evaluation still results in a lower density at the bottom than at the top. Estimated data must be handled carefully in further simulations based on these data.

In a short paragraph a method was demonstrated where light-transmission data was calibrated to absolute water content values calculated from X-ray attenuation data. A Hele-Shaw cell was filled with sand and a constant water table near the center of the cell was established. Then, the water saturation was calculated from vertical attenuation profiles. Light transmission data, recorded by a digital camera, was calibrated by comparison to X-ray data. This was done to make quantitative measurements of fingered flow through sand inside the Hele-Shaw cell.

5.1 Restrictions and limits of the setup used for X-ray tomography

As shown it is useful to determine the structure of soil samples additionally to multi-step outflow experiments. Also the description of heterogeneous samples

needs information about inner structures. In artificial samples these structures can be build by hand, but building them with accuracy e.g. by filling sand with different grain size distributions in distinct volumes in a column also is a difficult procedure. There it is useful to localize the exact position of the involved materials. This can also be done by computed tomography.
The setup used here allows acquisition times of maximal 16 s. Then the X-ray tube shuts down and image recording must be stopped or finished. If thick samples are used the photon flux needs to be large enough to detect adequate intensities on the detector to resolve spatial structures and changes within the sample. Therefore the power of the tube used has to be large, which leads to a fast warming of the device. The tube temperature also plays a major role when series of images are recorded to get three dimensional information by stacking sliced images.
These two problem can not be solved satisfactory. Always a tradeoff has to be found meaning that for many measurements in short time the power of the tube must be reduced to keep it cool. But there is a lower limit because the intensity behind the sample must still be detectable. Another possibility is to reduce the sample thickness (as done with the Hele-Shaw cell in sec. 4.4.1) where images can be recorded at lower tube power and remove the handicap of tube heating.
Still, there is the problem with the limited acquisition time. If the sample is at equilibrium data recording can be interrupted and continued in the next beam interval. This was done during most attenuation experiments presented in this work, where vertical profiles were recorded in more than on beam interval. This excludes the possibility to observe directly dynamics in the attenuation that change seriously during measurement time.
Tomographic images are taken during the 16 s beam time typically near half maximum tube power. If shorter scan times are needed the tube power has to be increased to keep the intensity on the detector in an adequate range reducing the number of measurements that can be done before the tube becomes too hot. In principle it is possible to get a complete three dimensional image of the sample if enough slices are recorded. The sample must be in hydrostatic equilibrium or steady state because the setup needs for such a scan more than five hours if 100 images are taken with a typical sample of 10 cm height and a vertical spatial resolution of 1 mm. This long scan time results from the time that has to be wait when the tube cools down. An alternative here is to sample the column at special depths that are determined from vertical attenuation profiles. This can be used to focus on parts of the column where heterogeneities are supposed e.g. large stones in natural soils or intersections

between materials in artifical samples.
If dynamic processes are studied, as in sec. 4.2, a loss of spatial resolution must be accepted. If the line sensor is mounted vertically rapid changes of attenuation in a vertical layer through the sample can be observed with scan intervals up to 40 Hz limited by the readout frequency of the detector. This is achieved with the loss of spatial information along the photon path through the sample and there is of course no information about locations that are not in the plane given by the X-ray source focus point and the vertical detector. The same principle works, if the detector is kept horizontal and attenuation through a layer in a single depth of the sample is monitored.

Bibliography

Arya, L. M. and Paris, J. F., 1981. A physicoempirical model to predict the soil moisture characteristic from particle-size distribution and bulk density data, *Soil Sci. Soc. Am. J.* **45**:1023–1030.

Bayer, A., Vogel, H.-J. and Roth, K., 2004. Direct measurement of the soil water retention curve using x-ray absorption, *Hydrology and Earth System Sciences* **8**:2–7.

Bear, J. 1988. *Dynamics of fluids in porous media*, General Publishing Company, Ltd.

Brooks, R. H. 1980. Water retention measurement for soils, *Journal of Irrigation and Drainage Div.* **106**:105–112.

Brooks, R. H. and Corey, A. T., 1966. Properties of porous media affecting fluid flow, *J. Irrigation and Drainage Div., Proc. Am. Soc. Civil Eng. (IR2)* **92**:61–88.

Buckingham, E. 1907. Studies on the movement of soil moisture, *Bulletin 38*, U.S. Department of Agriculture, Bureau of Soils, Washington, DC.

Burdine, N. T. 1953. Relative permeability calculations from pore-size distribution data, *Petr. Trans., Am. Inst. Mining Metall. Eng.* **198**:71–77.

Callaghan, P. T. 1990. Susceptibility-limited resolution in nuclear magnetic resonance microscopy, *J. Magn. Reson.* **87**:304–318.

Celia, M. A., Bouloutas, E. T. and Zarba, R. L., 1990. A general mass-conservative numerical solution for the unsaturated flow equation, *Water Resour. Res.* **26**:1483–1496.

Chan, T. P. and Govindaraju, R. S., 2004. Estimating soil water retention curve from particle-size distribution data based on polydisperse sphere systems, *Vadose Zone J.* **3**:1443–1454.

Císlerová, M. and Votrubová, J., 2002. Ct derived porosity distribution and flow domains, *J. Hydrol.* **267**:186–200.

Císlerová, M., Votrubová, J., Vogel, T., Amin, M. H. G. and Hall, L. D., 1997. Magnetic resonance imaging and preferential flow in soils, *In* F. J. L. M. Th. van Genuchten and Wu, L., (ed.) *Proc. Int. Workshop on Characterisation and Measurement of the Hydraulic Properties of Unsaturated Porous Media*, University of California, Riverside, CA 1999, S. 817–829.

Culligan, K. A., Wildenschild, D., Christensen, B. S. B., Gray, W. G., Rivers, M. L. and Tompson, A. F. B., 2004. Interfacial area measurements for unsaturated flow through a porous medium, *Water Resour. Res.* **40**:W12413.

Darcy, H. 1856. *Les Fontaines de la Ville de Dijon*, Dalmont, Paris.

Darnault, C. J. G., DiCarlo, D. A., Bauters, T. W. J., Jacobson, A. R., Throop, J. A., Montemagno, C. D., Parlange, J.-Y. and Steenhuis, T. S., 2001. Measurement of fluid contents by light transmission in transient three-phase oil-water-air systems in sand, *Water Resour. Res.* **37**:1859–1868.

Deinert, M. R., Parlange, J. Y., Steenhuis, T., Throop, J., Ünlü, K. and Cady, K. B., 2004. Measurement of fluid contents and wetting front profiles by real-time neutron radiograhy, *J. Hydrol.* **290**:192–201.

DeMan, B., Nuyts, J., Dupont, P., Marchal, G. and Suetens, P., 2001. An interative maximum-likelihood polychromatic algorithm for ct, *IEEE Transactions on Medical Imaging* **20**:999–1008.

Deurer, M., Vogeler, I., Khrapitchev, A. and Scotter, D., 2002. Imaging of water flow in porous media by magnetic resonance imaging microscopy, *Journal of Environmental Quality* **31**:487–493.

DiCarlo, D. A., Bauters, T. W. J., Steenhuis, T. S., Parlange, J.-Y. and Bierck, B. R., 1997. High-speed measurements of three-phase flow using synchrotron X rays, *Water Resour. Res.* **33**:569–576.

Dijk, P., Berkowitz, B. and Bendel, P., 1999. Investigation of flow in water-saturated rock fractures using nuclear magnetic resonance imaging (NMRI), *Water Resour. Res.* **35**:347–360.

Faybishenko, B. A. 1995. Hydraulic behavior of quasi-saturated soils in the presence of entrapped air: Laboratory experiments, *Water Resour. Res.* **31**:2421–2435.

Flury, M., Flühler, H., Jury, W. A. and Leuenberger, J., 1994. Susceptibility of soils to preferential flow of water: A field study, *Water Resour. Res.* **30**:1945–1954.

Freeze, R. A. and Cherry, J. A., 1979. *Groundwater*, Prentice-Hall, Inc.

Fuchs, T. 1998. *Strahlaufhärtungskorrekturen in der Computer-Tomographie*, PhD thesis, Institut für Medizinische Physik Friedrich-Alexander Universität Erlangen-Nürnberg.

Garnier, P., Angulo-Jaramillo, R., DiCarlo, D. A., Bauters, T. W. J., Darnault, C. J. G., Steenhuis, T. S., Parlange, J.-Y. and Baveye, P., 1998. Dual-energy synchrotron X ray measurements of rapid soil density and water content changes in swelling soils during infiltration, *Water Resour. Res.* **34**:2837–2842.

Gillham, R. W., Klute, A. and Heerman, D. F., 1976. Hydraulic properties of a porous medium: Measurement and empirical representation, *Soil Sci. Soc. Am. J.* **40**:203–207.

Graf, H. 2004. *Experimental investigations on multiphase flow in porous media*, PhD thesis, University of Heidelberg.

Haines, W. B. 1930. Studies in the physical properties of soils: V. The hysteresis effect in capillary properties and the modes of moisture distribution associated therewith, *J. Agric. Sci.* **20**:97–116.

Hainsworth, J. M. and Aylmore, L. A. G., 1983. The use of computer-assisted tomography to determine spatial distribution of soil water content, *Australian Journal of Soil Research* **21**:435–443.

Hassanizadeh, S. M. and Gray, W. G., 1993. Thermodynamic basis of capillary pressure in porous media, *Water Resour. Res.* **29**:3389–3405.

Hassanizadeh, S. M., Celia, M. A. and Dahle, H. K., 2002. Dynamic effect in the capillary pressure-saturation relationship and its impacts on unsaturated flow, *Vadose Zone J.* **1**:38–57.

Hemminga, M. A. and Buurman, P., 1997. NMR in soil science, *Geoderma* **80**:221–224.

Hopmans, J. W., Císlerová, M. and Vogel, T., 1994. X-ray tomography of soil properties, *Soil Sci. Soc. Am. Special Publication.*

Hopmans, J. W., Vogel, T. and Koblik, P. D., 1992. X-ray tomography of soil water distibution in one-step outflow experiments, *Soil Sci. Soc. Am. J.* **56**:355–362.

Hounsfield, G. N. 1973. Computerized transverse axial scanning (tomography). Part I. Description of the system, *British Journal of Radiology* **46**:1016–1022.

Hubbel, J. H. 1982. Photon mass attenuation and energy-absorption coefficients from 1 kev to 20 mev, *Int. J. Appl. Radiat. Isot.* **33**:1269–1290.

Ippisch, O. 2004. personal communication, Interdisciplinary Center for Scientific Computing, University of Heidelberg, Im Neuenheimer Feld 368, D-69120 Heidelberg.

Jain, A. K. 1989. *Fundamentals of digital image processing*, Prentice Hall.

Jaynes, D. B. 1992. Estimation hysteresis in the soil water retention function, *In* F. J. L. M. Th. van Genuchten and Lund, L. J., (ed.) *Indirect Methods for Estimating the Hydraulic Properties of Unsaturated Soils*, University of California, Riverside, CA 92521, S. 115–124.

Joseph, P. 1982. An improved algorithm for reprojecting rays through pixel images, *IEEE Transactions on Medical Imaging* **3**:192–196.

Kak, A. C. and Slaney, M., 1999. *Principles of Computerized Tomographic Imaging*, IEEE Press, The Institute of Electrical and Electronics Engenieers, Inc., New York.

Kastanek, F. J. and Nielsen, D. R., 2001. Description of soil water characteristics using cubic spline interpolation, *Soil Sci. Soc. Am. J.* **65**:279–283.

Kasteel, R., Vogel, H. and Roth, K., 2000. From local hydraulic properties to effective transport, *Europ. J. Soil Sci.* **51**:81–91.

Klein, O. and Nishina, Y., 1929. Über die Streuung von Strahlung durch freie Elektronen nach der neuen relativistischen Quantendynamik von Dirac, *Z. Phys.* **52**:853–868.

Klute, A. (ed.) 1986. *Methods of Soil Analysis. 1: Physical and Mineralogical Methods*, Agronomy Series 9, 2. edition, American Society of Agronomy, Madison, WI.

Kool, J. B. and Parker, J. C., 1987. Development and evaluation of closed-form expressions for hysteretic soil hydraulic properties, *Water Resour. Res.* **23**:105–114.

Kool, J. B., Parker, J. C. and van Genuchten, M. T., 1985. Determinig soil hydraulic properties from one-step outflow experiments by parameter estimation: 1. Theory and numerical studies, *Soil Sci. Soc. Am. J.* **49**:1348–1354.

Kosugi, K. 1996. Lognormal distribution model for unsaturated soil hydraulic properties, *Water Resour. Res.* **32**:2687–2703.

Kutílek, M. and Nielsen, D. R., 1994. *Soil hydrology*, Catena Verlag.

Matscheko, G. and Carlsson, G., 1989. Measurement of absolute energy spectra from a clinical ct machine under working conditions using a compton spectrometer, *Phys. Med. Biol.* **34**:209–222.

Mees, F., Swennen, R., van Geet, M. and Jacobs, P., (ed.) 2003. *Application of X-ray computed tomography in the geosciences*, The Geological Society London.

Microcal 1997. *Microcal Origin, Users's Manual*, Microcal Software, Inc., One Roundhouse Plaza, Northampton, MA 01060, USA.

Miller, E. E. and Miller, R. D., 1956. Physical theory for capillary flow phenomena, *J. Appl. Phys.* **27**:324–332.

Mualem, Y. 1976. A new model for predicting the hydraulic conductivity of unsaturated porous media, *Water Resour. Res.* **12**:513–522.

Mualem, Y. 1984. Prediction of the soil boundary wetting curve, *Soil Sci.* **137**:379–389.

National Institute of Standards and Technology 2004. http://physics.nist.gov/physrefdata/xraymasscoef/.

Neutron 92. *Neutron News* **3**:29–37.

Parker, J. C., Kool, J. B. and van Genuchten, M. T., 1985. Determinig soil hydraulic properties from one-step outflow experiments by parameter estimation: II. Experimental studies, *Soil Sci. Soc. Am. J.* **49**:1354–1359.

Parlange, J.-Y. 1976. Capillary hysteresis and the relationship between drying and wetting curves, *Water Resour. Res.* **12**:224–228.

Petrovic, A. M., Siebert, J. E. and Rieke, P. E., 1982. Soil bulk density analysis in three dimensions by computed tomography scanning, *Soil Sci. Soc. Am. J.* **46**:445–450.

Pires, L. F., Arthur, R. C. J., nad O. O. S. Bacchi, V. C. and Reichardt, K., 2004a. The use of gamma ray computed tomography to investigate soil compaction due to core sampling devices, *Brazilian Journal of Physics* **34**:728–731.

Pires, L. F., Bacchi, O. O. S. and Reichardt, K., 2004b. Damage to soil physical properties caused by soil sampler devices as assessed by gamma ray computed tomography, *Australian Journal of Soil Research* **42**:857–863.

Pons, M.-N., Weisser, E. M., Vivier, H. and Boger, D. V., 1999. Characterization of viscous fingering in a radial Hele-Saw cell by image analysis, *Experiments in Fluids* **26**:153–160.

Press, W. H., Teukolsky, S. A., Vetterling, W. T. and Flannery, B. P., 1992. *Numerical recipes in C*, Cambridge University Press.

Randall, E. W. and Ivanova, N. M. G. I., 1997. NMR studies of soil, soil organic matter and nutrients: spectroscopy and imaging, *Geoderma* **80**:307–325.

Rezanezhad, F. 2004. personal communication.

Richards, L. A. 1931. Capillary conduction of liquids through porous mediums, *Physics* **1**:318–333.

Roth, K. 2005. *Soil Physics. Lecture Notes*, Institute of Environmental physics, University of Heidelberg, `www.iup.uni-heidelberg.de/institut/forschung/groups/ts/students`.

Russo, D. 1988. Determining soil hydraulic properties by parameter estimation: On the selection of a model for the hydraulic properties, *Water Resour. Res.* **24**:453–459.

Ruth, C. and Joseph, P. M., 1997. Estimation of a photon energy spectrum for a computed tomography scanner, *Med. Phys.* **24**:695–702.

Samouëlian, A., Cousin, I., Richard, G., Tabbagh, A. and Bruand, A., 2003. Electrical resistivity imaging for detecting soil cracking at the centimetric scale, *Soil Sci. Soc. Am. J.* **67**:1319–1326.

Samouëlian, A., Richard, G., Cousin, I., Bruand, A. and Tabbagh, A., 2004. Three-dimensional crack monitoring by electrical resistivity measurement, *Europ. J. Soil Sci.* **55**:751–762.

Shepp, L. and Logan, B., 1974. The fourier reconstruction of a head section, *IEEE Tranactions on Nuclear Science* **NS-21**:21–43.

Si, B. C. and Kachanoski, R. G., 2000. Unified solution for infiltration and drainage with hysteresis: theory and field test, *Soil Sci. Soc. Am. J.* **64**:30–36.

Solymar, M., Lehmann, E., Vontobel, P. and Nordlund, A., 2003. Relating variations in water saturation od a sandstone sample to pore geometry by neutron tomography and image anslysis of thin sections, *Bull. Eng. Geol. Env.* **62**:85–88.

Stöhr, M. 2003. *Analysis of flow and transport in refractive index matched porous media*, PhD thesis, University of Heidelberg.

Tidwell, V. C. and Glass, R. J., 1994. X ray and visible light transmission for laboratory measurement of two-dimensional saturation fields in thin-slab systems, *Water Resour. Res.* **30**:2873–2882.

Toft, P. 1996. *The Radon transform - theory and implementation*, PhD thesis, Department of Mathematical Modelling, Technical University of Denmark.

Topp, G. C. 1971. Soil-water hysteresis: The domain model theory extended to pore interaction conditions, *Soil Sci. Soc. Am. J.* **35**:219–225.

Topp, G. C. and Miller, E. E., 1966. Hysteretic moisture characteristics and hydraulic conductivities for glass-bead media, *Soil Sci. Soc. Am. Proc.* **30**:156–162.

Tucker, D. M., Barnes, G. T. and Chakraborty, D. P., 1991. Semiempirical model for generating tungsten target x-ray spectra, *Med. Phys.* **18**:211–218.

Van As, H. and van Dusschoten, D., 1997. NMR methods for imaging of transport preocesses in micro-porous systems, *Geoderma* **80**:389–403.

van Dam, J. C., Stricker, J. N. M. and Droogers, P., 1992. Inverse method for determining soil hydraulic functions from one-step outflow experiments, *Soil Sci. Soc. Am. J.* **56**:1042–1050.

van Dam, J. C., Stricker, J. N. M. and Droogers, P., 1994. Inverse method to determine soil hydraulic functions from multistep outflow experiments, *Soil Sci. Soc. Am. J.* **58**:647–652.

van Genuchten, M. T. 1980. A closed-form equation for predicting the hydraulic conductivity of unsaturated soils, *Soil Sci. Soc. Am. J.* **44**:892–898.

Veeman, W. S. 1997. Nuclear magnetic resonance, a simple indroduction to the principles and applications, *Geoderma* **80**:225–242.

Vogel, H. J. 2000. A numerical experiment on pore size, pore connectivity, water retention, permeability, and solute transport using network models, *Europ. J. Soil Sci.* **51**:99–105.

Vogel, H.-J., Roth, K. and Bastian, P., 2002. Using bulk density measured by x-ray tomography to estimate the hydraulic structure of soil, *Transactions 17th World Congress os Soil Science, Bangkok, 2002* S. 1218/1–1218/2.

Wildenschild, D., Hopmans, J. W., Vaz, C. M. P., Rivers, M. L., Rikard, D. and Christensen, B. S. B., 2002. Using X-ray computed tomography in hydrology: systems, resolutions, and limitations, *J. Hydrol.* **267**:285–297.

Zurmühl, T. 1994. *Validierung konvektiv-dispersiver Modelle zur Berechnung des instationären Stofftransports in ungestörten Bodensäulen*, Bayreuther Bodenkundliche Berichte, Band 36.

Zurmühl, T. 1998. Capability of convection-dispersion transport models to predict transient water and solute movement in undisturbed soil columns, *Journal of Contaminant Hydrology* **30**:101–128.

Zurmühl, T. and Durner, W., 1998. Determination of parameters for bimodal hydraulic functions by inverse modeling, *Soil Sci. Soc. Am. J.* **62**:874–880.

A Equations of the implemented reconstruction algorithm

$$
\begin{aligned}
M_i &= \left(\sum_{h=1}^{J} l_{ih}\phi'_h\right)\left(Y_i^{\Phi\Phi}e_i + \frac{y_i(Y_i^{\Phi})^2}{\hat{y}_j^2}\right) + \\
&\quad \left(\sum_{h=1}^{J} l_{ih}\theta'_h\right)\left(Y_i^{\Phi\Theta}e_i + \frac{y_i Y_i^{\Phi} Y_i^{\Theta}}{\hat{y}_j^2}\right) && \text{(A.1)} \\
N_i &= \left(\sum_{h=1}^{J} l_{ih}\phi'_h\right)\left(Y_i^{\Phi\Theta}e_i + \frac{y_i Y_i^{\Phi} Y_i^{\Theta}}{\hat{y}_j^2}\right) + \\
&\quad \left(\sum_{h=1}^{J} l_{ih}\theta'_h\right)\left(Y_i^{\Theta\Theta}e_i + \frac{y_i(Y_i^{\Theta})^2}{\hat{y}_j^2}\right) && \text{(A.2)} \\
e_i &= 1 - \frac{y_i}{\hat{y}_i} && \text{(A.3)} \\
\phi'_j &= \left(\frac{\partial\phi}{\partial\mu}\right)|_{\mu_j^n} && \text{(A.4)} \\
\theta'_j &= \left(\frac{\partial\theta}{\partial\mu}\right)|_{\mu_j^n} && \text{(A.5)} \\
Y_i^{\Phi} &= \sum_{k=1}^{K} \Phi_k \hat{y}_{ik} && \text{(A.6)} \\
Y_i^{\Theta} &= \sum_{k=1}^{K} \Theta_k \hat{y}_{ik} && \text{(A.7)} \\
Y_i^{\Phi\Phi} &= \sum_{k=1}^{K} \Phi_k \Phi_k \hat{y}_{ik} && \text{(A.8)} \\
Y_i^{\Phi\Theta} &= \sum_{k=1}^{K} \Phi_k \Theta_k \hat{y}_{ik} && \text{(A.9)} \\
Y_i^{\Theta\Theta} &= \sum_{k=1}^{K} \Theta_k \Theta_k \hat{y}_{ik} && \text{(A.10)} \\
\hat{y}_{ik} &= b_{ik} e^{-\Phi_k \sum_{j=1}^{J} l_{ij}\phi(\mu_j^n) - \Theta_k \sum_{j=1}^{J} l_{ij}\theta(\mu_j^n)} \quad . && \text{(A.11)}
\end{aligned}
$$

The derivatives ϕ'_j and θ'_j at the points of inflection are defined as

$$\phi'_j = \frac{1}{2} \lim_{\epsilon \to 0} \left[\left(\frac{\partial \phi}{\partial \mu} \right) \Big|_{\mu_j^n - \epsilon} + \left(\frac{\partial \phi}{\partial \mu} \right) \Big|_{\mu_j^n + \epsilon} \right] \tag{A.12}$$

$$\theta'_j = \frac{1}{2} \lim_{\epsilon \to 0} \left[\left(\frac{\partial \theta}{\partial \mu} \right) \Big|_{\mu_j^n - \epsilon} + \left(\frac{\partial \theta}{\partial \mu} \right) \Big|_{\mu_j^n + \epsilon} \right] \quad . \tag{A.13}$$

Acknowledgments

Now its the time to thank a lot of people for being there and supporting me. To keep at least this chapter free from mistakes in writing, i will switch to my first language.

Nun ist es an der Zeit die Menschen zu nennen, die am Gelingen dieser Arbeit beteiligt waren.

Ohne Kurt Roth würde es diese Arbeit gar nicht geben, weshalb er auch an erster Stelle genannt werden soll. Er hat mich, vor nunmehr fast vier Jahren, in seine Gruppe aufgenommen und mich während der ganzen Zeit unterstützt. Viele motivierende, aufschlussreiche und unterhaltsame Gespräche haben dazu beigetragen, die Zeit interessant zu gestalten. Vielen Dank dafür.

Auch möchte ich mich bei Hans-Jörg Vogel bedanken, der mir ebenso durch unzählige Diskussionen Einblicke in die Bodenphysik gewährt hat. Außerdem hat er mich damals, als ich auf der Suche nach einer Promotionstelle war, dazu gebracht, in Heidelberg zu bleiben; dabei war nicht nur die Wissenschaft ausschlaggebend.

Die Zeit in Heidelberg hat auch dazu geführt, neue Leute kennenzulernen. Hans, den zweiten den ich Heidelberg kennengelernt habe, Ute, die in einem Lesemarathon dankenswerter Weise einen Teil der Schreibfehler dieser Arbeit verbessert hat. Auch die anderen sollen nicht vergessen werden: Leo, Holger, Anatja, Olaf, Volker, Carolin, Fereidoun, Benedikt und Klaus, wobei die Reihenfolge willkürlich gewählt wurde, haben mitgeholfen ein menschliches Umfeld zu gestalten. Zum angenehmen Arbeitsklima haben auch meine Büromitbewohner beigetragen; Thomas vor dem Umzug und Margarita, Bärbel und Tina danach. Wobei ich mich bei Tina nochmals für die Verdrängung des Sofas entschuldigen möchte; ich weiß, dass so eine Sache nicht ersetzt werden kann.

Die Entscheidung in Heidelberg zu bleiben, hatte jedoch auch zur Folge, dass ich mit meiner Freundin eine Wochenendbeziehung wagen musste. Jetzt, so kurz vor Schluss, kann ich wohl sagen, dass es funktioniert hat. Trotzdem freue ich mich auf die Zeit, die nun folgt, und wir uns dann auch mal unter der Woche sehen können. Für die Geduld und das immer noch Dasein möchte ich Danke sagen. Liebe Kiki, ich bin froh, dass es dich gibt und ich dich immer noch vermissen kann, aber bald nicht mehr muss.

Meinen Eltern möchte ich sagen, dass der Sohn bald aus dem Gröbsten raus ist. Es hat sich gelohnt, hinter ihm zu stehen. Ich glaube, ihr wisst gar nicht wie sehr das geholfen hat und ich kann es auch nicht in Worte fassen. Um die Familie zu komplettieren, will ich auch meine kleine Schwester Stephie erwähnen, die gar nicht mehr so klein ist, aber trotzdem immer meine kleine Schwester bleiben wird. Und das ist auch gut so, weil ich mir keine bessere kleine Schwester vorstellen kann.

Es gab auch ein Leben neben der Uni, in dem ein zwei Menschen ein Rolle gespielt haben, die ich nicht verschweigen möchte. Jens und Wolle, die sich immer wieder dazu hinreißen ließen, den einen oder anderen gemütlichen Abend mit mir zu verbringen. Auch wenn der Kontakt eher unregelmäßig war, war er doch immer da. Goldi und Alex, mit denen endlich mal wieder ein Treffen ansteht. Ebs, der es nicht geschafft hat mir den Spaß am „wissenschaftlichen“Arbeiten zu nehmen, sondern, im Gegenteil auch irgendwie selbst daran Schuld ist hier erwähnt zu werden. Ich bin auch froh darüber, Christoph und Frank getroffen zu haben, die als außeruniversitäre Mitbewohner nicht zu ersetzen waren. Angela und Jochen, die ich nicht aus den Augen verlieren möchte.

So, abschließend sei allen gesagt, die sich nun vergessen fühlen, dass ich sie nicht absichtlich weggelassen, sondern nur vergessen habe.